THE UNIVERSITY OF CHICAGO

QUANTUM METROLOGY WITH SPIN DEFECTS IN NANODIAMONDS

A DISSERTATION SUBMITTED TO
THE FACULTY OF THE INSTITUTE FOR MOLECULAR ENGINEERING
IN CANDIDACY FOR THE DEGREE OF
DOCTOR OF PHILOSOPHY

BY
PAOLO ANDRICH

CHICAGO, ILLINOIS
DECEMBER 2017

for Giuliana Togno

If you want the truth to stand clear before you, never be for or against,

the struggle between for and against is the mind's worst disease.

Sengcan

CONTENTS

LIST OF FIGURES

ACKNOWLEDGMENTS

There is an enormous amount of people without whom this work would not have been possible and who deserve a lot more credit than I can express in just few lines. Nevertheless, I still want to voice my gratitude and I hope they will all forgive me for the brevity.

Firstly, I want to thank my advisor David Awschalom, for believing in me from the day that I walked into his office in Santa Barbara as a confused engineering student, until the last day of an adventure that brought him also to the (dark) engineering side in Chicago. His constant support and attention in creating an environment filled with great scientists was what made this experience truly formative and invaluable. I am therefore grateful also to all the members of the group that have cross paths with me and taught me so much about science and life. Some colleagues in particular deserve a mention. Viva and Benji were the first to take me under their wings and were not only great teachers but also helped me adjust to the new life that I was embarking into. Ken and Brian (Maertz) were the rest of the crew that kept me company during the long periods of isolation in the CNSI building. The pretty regular cleanroom encounters with Greg and Alberto were a source of tips on how to solve fabrication blunders and what lightened up the long hours in a bunny suit. Charlie and Paul were not only the students with whom I overlapped the most, I am also happy to have called them roommates for almost two years and, in particular, I want to thank Charlie for always being there to listen to my rants and concerns and to help me pull through the hardest moments. Brian (Zhou) was also an amazing teammate and his support was invaluable, especially in the last lonely days of the Searle era. Joost instead kept me sane during my days in the ERC office. Joe has essentially always been there during all these years to help me with whatever I needed, from the most boring activities like proofreading drafts for the hundredth time, to talking through the latest science developments.

I also want to thank some other people who I encountered during my PhD and who gifted me both with their scientific insights and with their friendship. Thank you Claire, Bryan, Laetitia, Joerg, Nitin, Sukumar, Shanying, David, Alex, Xiaoying, Jiajing, Sunanda, Etienne, and Audrey, I would not have made it without you. A thanks goes also to all the people who run the CNSI, UCSB

Nanofab, MRSEC, and PNF facilites, without whom nothing could have happened. In particular thanks go to Aidan, Shiva, Qiti, Justin, Peter, Sally, and Maria. Equally important were all the people that helped me navigate through the bureaucratic complications of a PhD life. Thank you Holly, Sonya, Lynne, Daniel, Mary Pat, Rovana, and Novia.

Maybe they did not participate in the scientific aspect of my quest but all the people who supported me with their friendship and love during all these years were as critical as anybody else. Liam and Ciara, Lydia, Brendan, AJ, Marc, George, Cem, Siavash and all the Chicago soccer crew, thank you for the amazing moment spent together. I am obviously immensley grateful to my family, to Hope, and to her family for always believing in me, even when I am not sure I was really believing in myself. I think that nothing else helped more than you being with me during this adventure.

Finally, there is unfortunately a person who I cannot directly thank but to whom I owe one of the largest debt of gratitude. Nobody more than Professoressa Togno fueled my passion for science and influenced the career choices I have made so far. I immensely regret not telling her this before it was too late, but I will always bring her memory with me.

ABSTRACT

The negatively charged nitrogen-vacancy center in diamond has become a prominent room temperature spin qubit platform for quantum information and sensing applications owing to its inherent optical addressability and long spin coherence times. In particular, a major research effort has focused on exploiting the metrology capabilities of the nitrogen-vacancy center to investigate the details of biological and magnetic systems at the nanoscale using diamond micro- and nanoparticles (we will mostly refer to these as nanoparticles in what follows). These particles behave like highly localized, low-thermal-mass spin systems and can therefore be used for high spatial resolution, high sensitivity mapping of their environment.

Nonetheless, some outstanding challenges limit the sensing capabilities of these nanosensors. On the one hand, the nitrogen-vacancy centers contained in nanoparticles present strongly degraded coherence properties compared to what is common in bulk diamond due to a higher density of structural defects and impurities. On the other hand, in order to investigate systems that produce a signal that decay fast with distance (e.g. single or small ensembles of spins), the qubit needs to be placed within a few nanometer of the diamond surface. Because of the presence of magnetic and electric noise resulting from electronic spin and charges at the interface, the coherence of the qubits is further diminished. As the nitrogen-vacancy center's coherence properties ultimately limit the achievable sensitivity, improving thse properties has been a central research focus in the scientific community.

In this thesis two main approaches to extend the capabilities of diamond nanoparticles as nanoscale sensors are investigated. Firstly, we discuss a fabrication process developed to produce nanodiamonds with controlled crystal properties, shape, size, and nitrogen-vacancy center placement and density. We show that these accomplishments are conducive to enhanced photoluminescence properties and bulk-like spin coherence times. We additionally demonstrate that, thanks to their precisely controlled geometry, the nanoparticles can be optically trapped within a microfluidic system and behave as highly stable, contactless nanoprobes in solution.

In a separate effort, we study hybrid quantum architectures that promise to improve the sensi-

tivity of the nitrogen-vacancy centers by enabling the amplification of the signal to be measured. In this way, the requirements on the position of the qubits with respect to the diamond's interface can be relaxed. In particular, we first develop a technique to create portable arrays of nanoparticles embedded within a flexible and transparent matrix that can be placed in contact with a sample and provide two-dimensional mapping capabilities. We then use this sensing platform to create a ferromagnet-nanodiamond hybrid system to study the interactions between collective spin excitations (spin waves) in the ferromagnet and ensembles of nitrogen-vacancy centers in the nanodiamonds. We show that surface confined spin waves interact strongly with the qubits' spins and can mediate and enhance their coherent magnetic interactions with a microwave source. These results pave the way to the use of spin wave mediated coupling as a way to improve the sensitivity of the nitrogen-vacancy centers both in nanoparticles and bulk material.

CHAPTER 1

INTRODUCTION

It has become a cliché to begin a discussion about nanotechnologies citing Richard Feynman's famous 1959 lecture 'There's plenty of room at the bottom'[43]. Here, the physicist details his view on the future of miniaturization and strongly encourages researchers of all disciplines to enter a "new field of physics", which would venture into "the problem of manipulating and controlling things on a small scale". However, as with other "corny opening remarks" (e.g. Moore's law), its appeal resides in the accuracy with which it described the world to come. Indeed, in the last few decades, scientists from all backgrounds embraced Feynman's invitation and delved into a relentless effort towards miniaturization and the understanding of nature at a smaller and smaller scale. Examples of this trend are the advancements in protein crystallography[124], the development of nanorobots for biological applications[66], the engineering of materials at the nanoscale level that fueled the emergence of novel properties[156], and many more. The rapid fluorishing of nanometer scale devices has, in particular, stimulated the parallel quest for new technologies that could enable the investigation of various physical parameters with unprecedented spatial resolution, in order to shed a light on the details of their inner workings. From these efforts emerged the field of nanoscale metrology, which is the main focus of the work presented in this thesis. To contextualize our results, in the rest of this chapter we are going to take a closer look at the state of the art of this field, particularly for what concerns magnetic field and temperature sensing.

1.1 Requirements for a nanosensor

Nanoscale metrology, or nanometrology, is the science that deals with the quantitative investigation of the state of a physical systems at the micro- and nanometer scale. This process requires, for instance, the measurement of dimensions, forces, optical and electronic properties, magnetic and electric fields, and temperature. Various figures of merit and operational parameters can be used to determine the quality of a sensor, and these can vary in importance depending on the specific appli-

cation. In this work, we are interested in the detection of magnetic fields of samples ranging in size from few microns down to only few atoms, with nanoscale spatial resolution. Likewise, we focus on temperature sensing applications where either the sample to be measured or the desired spatial resolution are in the nanometer scale range. This imposes stringent requirements on the sensor, in particular on its size and on its position control, as it is crucial that it can be placed in close proximity of the system to be measured. We further note that, in the case of temperature measurements of nanoscale systems, the thermal mass of the sensor also needs to be minimized to avoid perturbing the temperature distribution of the sample. For this reason, ideal temperature sensors for nanoscale applications are contactless so as not to introduce spurious heat transfer channels. This is also an important feature for magnetic field sensors for biological in vivo measurements, as the need for any contact could disrupt the sample. Finally, another significant parameter for a sensor is its bandwidth, which describes the range of signal frequencies that it can detect. The bandwidth is usually either limited by intrinsical physical properties of the system or by the electronics that is responsible for the collection of the signal.

In recent years, considerable efforts have been focused on advancing magnetic[45] and thermal [170] microscopy, and in the following we are going to use the requirements that we discussed to briefly review the products of these advancements and the open issues that researchers are trying to address.

1.2 Magnetic microscopy

For decades, scientists have been studying tools that could enable the sensing of ultra-low magnetic fields with high spatial resolution. As many chemical elements possess nuclear or electronic magnetic moments, a sensor with enough sensitivity to detect the faint magnetic fields they generate could reveal the chemical identity of atoms and establish the three-dimensional arrangement of molecules. This process has been mostly driven by x-ray crystallography and nuclear magnetic resonance measurements, which allowed, for instance, to determine in the 1990s the structure of the human tumor suppressor protein p53[18, 24]. This information played a crucial role in gaining

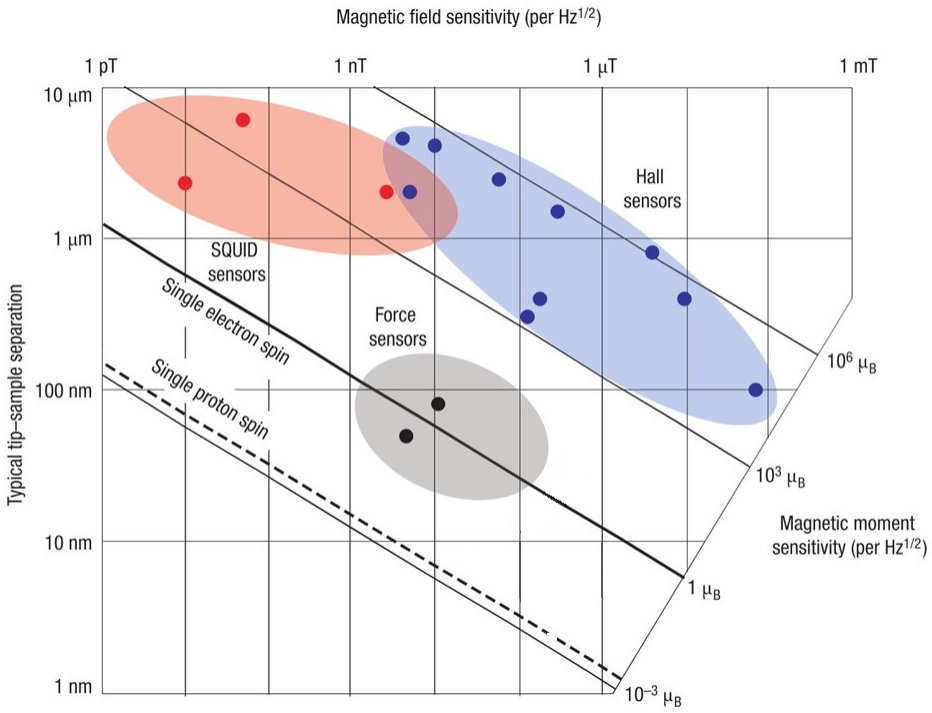

Figure 1.1: Magnetic sensing cababilities for a variety of techniques developed to detect small magnetic fields at the micro- and nanoscale. The dots correspond to experimental results for Hall sensors[11], SQUID sensors[73, 48, 63], and nanomechanical force sensors[127, 30]. Nanoscale spin detection is affected both by magnetic field sensitivity (horizontal axis) and tip-sample separation (vertical axis), with the best magnetic moment sensitivity being in the bottom left corner of the graph. Adapted from [28].

insights into the mechanism by which p53 regulates cell metabolism. Unfortunately, both x-ray crystallography and nuclear magnetic resonance have very stringent requirements for the morphology of the samples to be analyzed. Specifically, both techniques necessitate homogeneous samples composed of either highly purified solutions, which require prohibitive purification processes, or well-ordered crystals, which are not available for a large number of molecules. For this reason, the development of experimental techniques that could directly measure the magnetic signal originating from a few spins has been at the center of extensive research efforts.

But the analysis of molecular structures is not the only driving force in this field. The study of stray magnetic fields in magnetic materials has also attracted substantial interest due to its application in the investigation and design of magnetic recording devices. Additionally, a large number of physical effects rely on the nanoscale magnetic response of a system to external fields (e.g.

superconductivity), or on the details of its internal magnetization (e.g. spin Seebeck effect).

One aspect that all the applications we mentioned have in common is the need to detect fields that quickly decay with the distance from their source. For instance, the magnetic field of a magnetic dipole drops off as the inverse third power of the distance. For this reason, one very important parameter for a sensor, in addition to its overall magnetic field sensitivity, is the minimum achievable separation between the sensor itself and the sample. It is important to stress that this also translates into a requirement on the size of the sensor itself, as it is crucial that the whole sensing volume is exposed to the same magnetic field to be measured.

Figure 1.1 shows the magnetic field sensitivities and the minimum sensor-to-sample separation for several experimental techniques developed in recent years. Here, an additional figure of merit, the magnetic moment sensitivity, is introduced, which identifies the minimum number of Bohr magnetons detectable with one second of data collection. This parameter combines the contributions of magnetic field sensitivity and sensor size and it is of particular importance to determine the ability of a system to detect small number of spins. We are now going to briefly review these existing experimental techniques to better understand their features and current limitations.

1.2.1 Hall sensors

Magnetic field sensing with Hall sensors is based on the classical Hall effect. This effect appears in materials with mobile carriers and consists in the generation of a voltage transversal both to an electric current flowing through the material and to an externally applied magnetic field. The sensing process is based on the dependence of the amplitude of the Hall voltage on the magnitude of the magnetic field.

Hall sensors have numerous desirable features. For one, the ultra-fast response of the Hall effect to external field variations translates in a measurement bandwidth extending from DC to the GHz range[11]. Additionally, Hall sensors can be employed in the presence of fields up to tens of tesla. Finally, they can be operated from cryogenic temperatures to at and above room temperature. The room temperature operation is especially desirable as it allows for the measurements of biological

systems and of devices at ambient conditions.

The main limitation to the usage of these devices for nanoscale sensing resides in the inversional relationship that exists between their sensitivity and the dimensions of the sensor, which qualitatively explains the position of the Hall sensor's experimental values in Figure 1.1. In essence, improvements in the spatial resolution can only happen to the detriment of the field sensitivity. Additionally, the miniaturization process results in a larger pink noise (with $1/f$ dependence, where f is the operational frequency) contribution due to the smaller amount of charge carriers, which strongly affects the performance of the sensor at low frequencies. Finally, the need for electrical connections to the sensor and the use of materials that are not generally biocompatible complicates the investigation of living biological systems.

1.2.2 Superconducting quantum interference device magnetometers

Superconducting quantum interference devices (SQUIDs) are among the most sensitive magnetic flux and field detector currently known, allowing for field resolution at the 10^{-17} T level[42]. A SQUID consists of a superconducting loop interrupted by one or two Josephson junctions, and measurements of magnetic fields usually reduce to measurements of voltage fluctuations across the junctions generated by variations in the magnetic flux present through the loop (see Figure 1.2(a)). In recent years, considerable efforts were devoted to use SQUIDs to detect the magnetic response of micro- and nano-objects developing the field of nano-SQUIDs. In this regime it has been proven that the sensor magnetic moment sensitivity improves linearly with decreasing SQUID linear size[51], which led to the progressive device miniaturization and to sensitivities reaching few Bohr magnetons per unit of bandwidth.

Despite their disruptive potential, SQUID sensors suffer of two major drawbacks when it comes to nanoscale sensing. First, the device fabrication complexity and the fragility of its quantum properties complicate the integration of these systems with a scanning probe technology, which limits the ability to perform sensing in close proximity of the sample. Additionally, the requirement for the superconducting loop (and for additional pick-up coils[42]) to be kept at cryogenic temper-

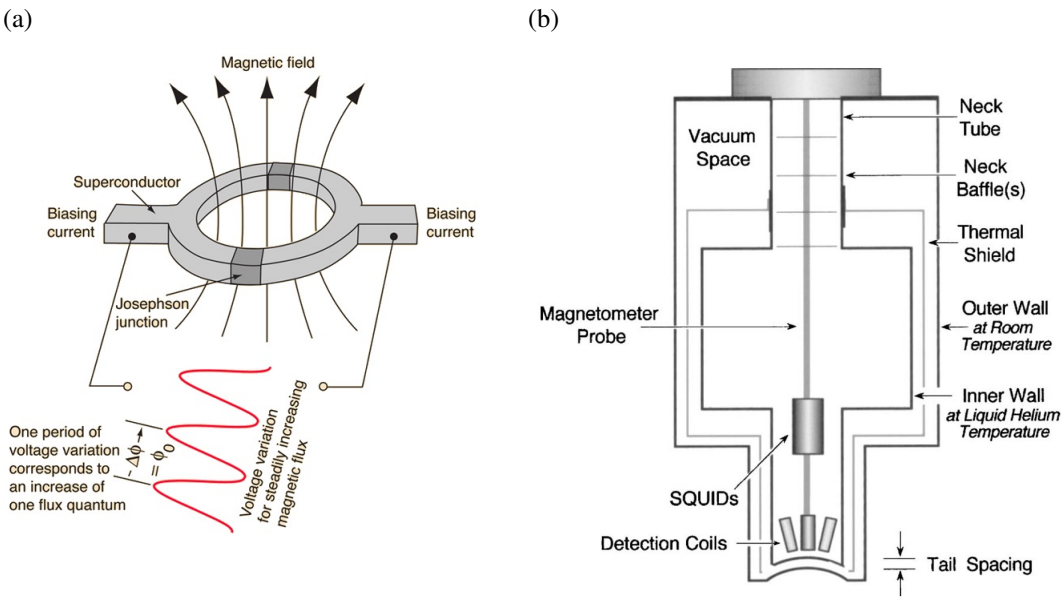

Figure 1.2: (a) A schematic of a typical squid element[23]. A biasing current is flown through a superconducting loop interrupted by two Josephson junction. The voltage across the loop, which depends on the encircled magnetic flux, is measured. (b) Typical design of a complete SQUID system for biomagnetic measurements[42]. The need to maintain the sensor at cryogenic temperatures imposes a limit on the distance from the sample.

atures imposes an additional limitation to the sensor-to-sample distance for ambient conditions measurements because the sensor needs to be packaged within a thermally insulated region (see Figure 1.2(b)). This prevents the use of SQUIDs sensors for measurements inside biological systems. Finally, although bandwidths up to tens of MHz have been demonstrated recently using dispersive measurements in custom made systems[86], the maximum bandwidth of commercially available systems only extends typically from DC to 50 kHz, mostly due to limitations on the control electronics (SQUIDs have an intrinsic bandwidth of several gigahertz).

1.2.3 Magnetic resonance force microscopy

The last magnetometry technique that we are going to analyze is magnetic resonance force microscopy (MRFM), which was first described in the seminal work by John Sidles in the early 1990s[137]. This technique resorts to a combination of atomic force microscopy (AFM) and nuclear magnetic resonance (NMR) or electron spin resonance (ESR) methods to enable the mea-

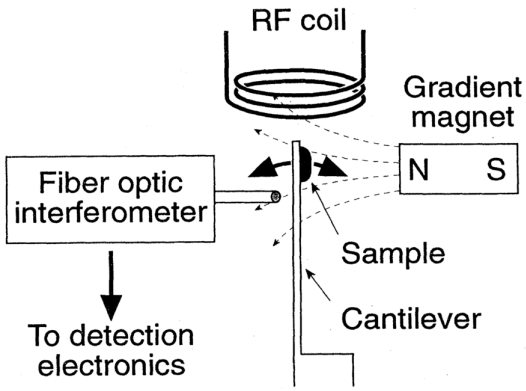

Figure 1.3: Schematic of a magnetic resonance force microscopy apparatus for the case where the sample is anchored to the cantilever and a ferromagnet provides a magnetic field gradient[138].

surements of very small numbers of spins. In particular, a microscale cantilever with a magnetic tip is used to detect the force generated by the magnetic moment of the target spins, while a forced precession is induced on these spins at the mechanical resonant frequency of the cantilever. The magnetic tip of the cantilever is also used to generate a highly non-uniform magnetic field, which is used to spatially resolve the driving frequency of spins of the same species, thereby improving the achievable spatial resolution[107]. We note that another possible approach to these measurements relies on positioning the sample on the cantilever and the use of an external magnet to generate the magnetic field gradient[138] (see Figure 1.3).

MRFM has some important advantages over the magnetic sensors that we previously described. First, this technique offers elemental and isotopical sensitivity, meaning that the detected signal is specific of a particular electronic or nuclear species. This is a consequence of the dependence of the spins' driving frequency on their intrinsic magnetic moment through the effect of the Zeeman splitting of the spin energy levels induced by the external magnetic field. Additionally, the magnetic field imaging is three dimensional as the presence of the field gradient also allows for the differentiation of the signal coming from different distances from the tip. The resonant nature of MRFM, while limiting the bandwidth of the measurement, also makes this technique insensitive to noise outside the narrow resonance width of the probe.

MRFM measurements recently enabled the detection of the spin of a single electron[127] and

of nanometer-size volumes of nuclei[30], but advancements beyond this limit have been challenging to obtain. Efforts to enhance the sensitivity of MRFM have focused on improvements in the cantilever design (smaller motional masses and longer damping times are desirable[138, 107]) and in devising stronger magnetic field gradients, but design tradeoffs emerge at very small scales. For instance, stiffer (and heavier) cantilevers guarantee longer damping times, which allow for better noise suppression, but their larger mass requires stronger signals to be perturbed. Additionally, to achieve noise levels suitable for the detection of few spins, all the measurements need to be performed at ultra-low temperatures (< 1 K), precluding the study of systems at ambient conditions. Finally, the bandwidth of MRFM is inversely proportional to the damping time of the cantilever and it is therefore related to its design. As we previously discussed, the damping time needs to be maximized to optimize the sensitivity, therefore it is not possible to directly control the bandwidth of the system. On the other hand, the frequency of the cantilever mechanical resonance is also controllable in part through its design, which could enable the optimization of the system at different operation frequencies depending on the application. However, the resonance frequency, the mass of the cantilever, and its dimensions are interconnected, which complicates this optimization process.

From the discussion in this section and the data included in Figure 1.1 we can therefore conclude that, despite the considerable advancements obtained in recent years in the field of magnetic microscopy, substantial improvements still need to be made to reach the limit of single nuclear spin detection, particularly when the measurements need to be performed at ambient conditions.

1.3 Thermal microscopy

As we previously mentioned, the rapid progress in the ability of engineering materials at the nanometer scale has resulted in the emergence of a large number of novel nanoscale devices[15]. At these dimensions, thermal transport can have profoundly different properties than in the case of macroscopic systems, interfaces become increasingly more important, and the accumulation

of heat can lead to short device lifetimes, or electrical and mechanical failures. To gain insight in these phenomena it is crucial to have access to accurate local temperature measurements with nanoscale resolution. Furthermore, a growing body of research on temperature controlled gene expression[71, 80], tumor metabolism[158], and cell-selective disease treatments[133] has called for the development of temperature sensors that can be integrated within living systems.

Conventional temperature measurements rely on the electrical or the optical properties of materials. For instance, standard thermocouples take advantage of the Seebeck effect, in which a temperature gradient across two dissimilar electrical conductors or semiconductors results in a finite electrical potential across the junction between the two materials[54]. Alternatively, infrared thermometry relies on variation in the electromagnetic emission spectrum to extract information regarding the sample's temperature. Both these methods are well established and can provide good accuracy and a spatial resolution of a few microns, but limitations in the minimum dimensions of the probe and in the diffraction limit of the excitation source make further improvements challenging.

Various novel tools have been developed in recent years to go beyond these limits. Figure 1.4 shows the state of the art achievements for the best temperature micro-sensors in terms of their size and accuracy. We note that, as it is described here, the accuracy of a sensor is different from its sensitivity as it refers to the ability of approximating the real temperature of the sample instead of indicating the smallest variation that can be measured.

As we previously mentioned, the size of the sensor influences both the achievable spatial resolution and the accuracy as larger sensors can introduce additional thermal dissipation path in the system. We note that in the graph in Figure 1.4, the size refers to the active sensing component of the device and how well its position can be determined. In the rest of this section we will further analyze the details of these parameters in some examples.

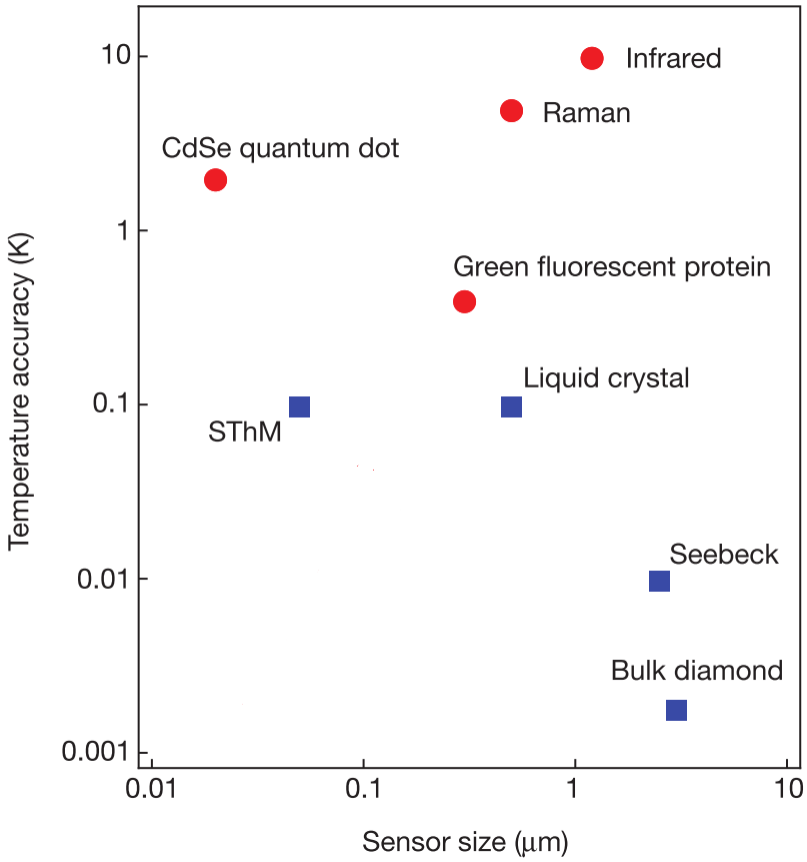

Figure 1.4: Sensor size and temperature accuracy for existing thermal microscopy techniques. Red circles indicate methods that are biologically compatible. Adapted from [79].

1.3.1 Scanning thermal microscopy

As in the case of MRFM, the development of scanning microscopy (AFM and scanning tunnel microscopy, STM) led to major improvements in the sensitivity and spatial resolution of temperature sensing techniques. In particular, thanks to the advancements in nanofabrication techniques, it became possible to create nanometer sized temperature sensors that could be integrated with AFM and STM tips to take advantage of the sub-100 nm spatial resolution of these tools[94]. Various types of sensors based on different physical principles can be used. One approach relies on the integration of miniaturized thermovoltage-based systems, which follow the working principle of standard thermocouples (see Figure 1.5(a)). Additionally, sensors based on the temperature dependence of the electrical resistance of micrometer-sized wires have been developed[121]. Both these techniques suffer from the need of rather complicated fabrication techniques to create the sensor

at the tip of a scanning probe. Thermal expansion schemes using bimaterial cantilevers have been used in order to reduce the fabrication requirements but the larger size of the sensing region complicates the control of the heat flow from the sample to the sensor[94], and the measurements need to be performed in vacuum.

Overall, scanning thermal microscopy (SThM) techniques allow for spatial resolutions smaller than 100 nm, temperature accuracy $\sim$100 mK, and temperature resolution of $\sim$1 mK in a 100 Hz bandwidth. Improvements in the temperature resolution are usually obtained through lock-in techniques where the temperature of the sample is modulated at a frequency f. In principle, this frequency should be as high as possible to suppress the $1/f$ components of the pink noise, but its upper boundary is limited by the temporal response of the sample and the sensor, which depends on their size.

The spatial resolution is ultimately limited by the tip sharpness, but only limited improvements are currently accessible as a sharper tip comes with the added cost of increasing the sample-tip heat transfer resistance. When this resistance becomes comparable with the resistance of other heat propagation channels (e.g. gas conduction) the accuracy of the measurement diminishes. One additional limitation of SThM is the large overall thermal mass of the sensing system, which can impact the real temperature especially of micro- and nanoscale samples, and sets a hard limit on the temperature accuracy of this technique. Finally, SThM techniques are not compatible with biological samples, both because of the materials used, which are not in general biocompatible, and due to the need for contacts between the probe and the measurement system. In the following we will see how some of the limitations of SThM can be addressed with other techniques.

1.3.2 Nanoscale fluorescence thermometry

Another approach to nanoscale temperature sensing relies on the temperature dependence of the fluorescence properties of nanoparticles and organic dyes. These optical techniques have several advantages, especially when it comes to measurements in biological settings. In particular, their non-contact nature translates in a minimal disruption of the system to be measured, which is of par-

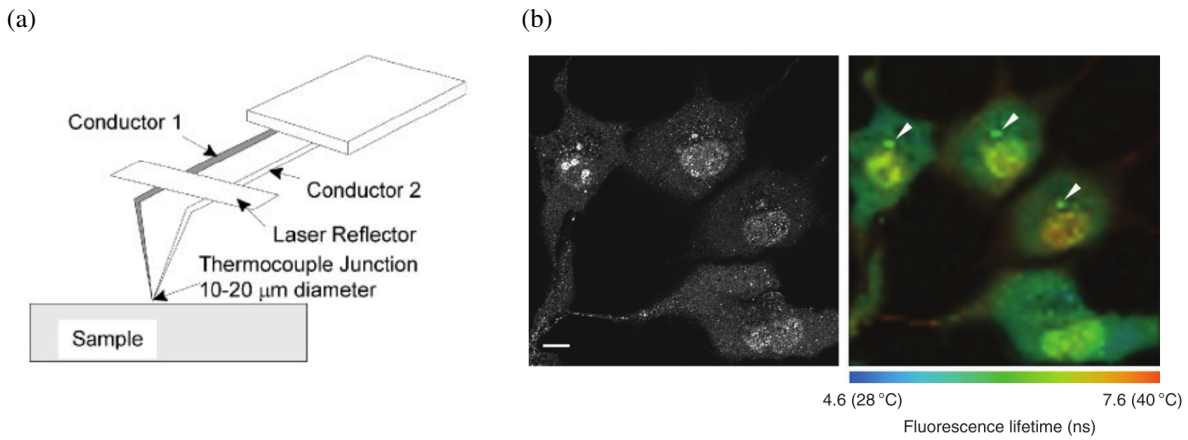

Figure 1.5: (a) Schematic of a scanning thermal microscopy tip with an integrated microscale thermocouple probe[94]. (b) Confocal fluorescence image (left) and fluorescence lifetime mapping (right) of a fluorescent polymeric thermometer inside COS7 cells[116]. The temperature map of the cells is extracted from the variations in the fluorescence lifetime of the polymer.

ticular importance, for instance, for intra-cellular measurements. Additionally, the nanometer size and the isolation of the probe from the measurement apparatus means that the sensing region has a small thermal mass and therefore does not interfere significantly with the heat transfer processes and can rapidly reach thermal equilibrium with its environment, which is particularly important for time-dependent studies. Furthermore, the spatial resolution of this technique is in principle only limited by the size of the fluorescent probe[129, 87].

It is important to note that, particularly when considering thermometry applications in biological systems, the sensors should satisfy requirements that go beyond excellent temperature and spatial resolution. Specifically, the sensor's output should be independent from environmental changes in pH, ionic strength, and the surrounding biomolecules. The output should also not be affected by the concentration of the sensing agent, the excitation intensity, and the history of the sensor, or else variations in the collected signal could be incorrectly interpreted as changes in temperature. Various systems that satisfy these requirements have been proposed and implemented. For instance, the temperature dependence of the emission spectrum of quantum dots[166] and fluorescent nanoparticles[155] have been used to perform measurements of intra-cellular temperatures with sub-degree accuracy. However, these approaches require long integration times, thereby not allowing for real-time measurements. Additionally, spatially resolved intra-cellular measurements

have not been possible because of the challenges in controlling the sensor's position. A recently described experiment based on fluorescent polymers[116] demonstrated the temperature mapping of living cells with 200 nm spatial resolution and temperature accuracy from 0.18 °C to 0.58 °C in the 29 °C to 39 °C range. Temperature variations are detected as changes in the polymers fluorescence lifetime (see Figure 1.5(b)), which again requires long integration times and limits the temporal resolution of the measurements. An attempt to address some of these limitations has been made through the use of green fluorescent proteins (GFPs) as thermal nanoprobes[37]. GFPs are already widely used as contrast agents in biology because they can be genetically expressed in many organisms, making it a noninvasive marker for in vivo applications, and their position is highly controllable. Temperature measurements with GFPs are based on fluorescence polarization anisotropy (FPA), which involves the measurement of the relative intensities of the fluorescence light polarized parallel and perpendicular to the incident polarization. Because only light intensities are measured, the read-out can be fast, and at the same time a $\sim$300 nm spatial resolution and 0.4 °C temperature accuracy are still achievable. The main drawback of this technique is the output's dependence on the viscosity of the medium, which translates into a requirement for medium specific calibrations. Additionally, GFP expression has been proven difficult to obtain in certain primary cell types[136], and their photoluminescence is not stable in time[32, 25].

As it is the case for magnetic field sensing, there are several challenges that need to be addressed in order to truly extend thermal microscopy to the nanoscale, particularly when we are interested in the study of biological systems. The crucial properties of biocompatibility, small thermal mass, contactless nature, photostability, and output's independence from the surrounding medium still have not been identified in a single system.

1.4 Thesis overview

In chapter 2, we are going to introduce a novel platform that has been recently investigated to address the limitations of the available sensing architectures, the nitrogen-vacancy (NV) center in

diamond. The NV center is a paramagnetic defect in the diamond lattice, which behaves as an atomic system trapped within a solid state lattice. As a result, it can offer the properties of discreteness and sensitivity to the environment that are common for atomic energy levels but without the need for the complex handling systems that are required for isolated ions.

First, we will introduce the basic optical and electronic properties of the NV centers and explain the physical principles that result in the NV center's sensitivity to magnetic fields and temperature variations. Depending on the specific application and properties of the signal to be measured, the implementation of the sensing measurements can assume different forms, which we will describe in details. We will also briefly discuss the effect of the proximity of the NV centers to the diamond surface and how this can limit the achievable sensitivity.

As discussed in this chapter, major nanoscale sensing efforts have been directed to the study of the properties of complex systems (e.g. live cells, magnetic devices) with high spatial resolution. For the NV centers community this desire has generated widespread interest towards the use of diamond nanoparticles as nanoscale probes, which could be brought in contact and scanned over, or within, a sample. Chapter 3 will begin with an overview of the existing fabrication processes for diamond nanoparticles and of the properties of the resulting material. The limitations that are encountered when using these nanodiamonds for sensing purposes are then described.

In Chapter 4 we will present a novel fabrication process that we developed to address these limitations and push the limits of nanodiamond sensing architectures towards the levels achievable with bulk diamond material. After describing the details of the fabrication steps, we will analyze the photoluminescence and spin properties of the NV centers to compare the quality of our engineered nanoparticles with the ones described in Chapter 3. We will also discuss the use of the nanodiamonds as stable, contactless sensors optically trapped inside a microfluidic channel and demonstrate the possibility to achieve bulk-like magnetic field sensitivity in solution.

As we have mentioned before, the intrinsic sensing properties of the probe are not the only important operational aspect. For a large number of sensing applications the ability to orderly place the nanodiamonds in good contact with the sample and in a repeatable manner is critical.

In Chapter 5 we address these requirements and introduce an easily scalable technique that we developed to obtain portable and flexible arrays of nanodiamonds. We characterize the fabrication process and identify parameters' regimes that guarantee the fabrication of high coverage or single particle arrays.

Finally, in Chapter 6 we will look at another approach to enhance the sensitivity that is achievable with diamond nanoparticles (and more in general with NV centers in diamond) that does not rely on the optimization of the defect's intrinsic quality. Instead, here we will investigate the possibility of integrating the nanoparticles within a hybrid quantum architecture, in which a system external to the diamond crystal and having different properties can help compensating for the NV center's shortcomings. In particular, we construct a hybrid nanodiamond-ferromagnet platform and investigate the properties of the interactions between propagating spin waves excited in the ferromagnet and the NV centers. Our goal is to establish the possibility of using the spin waves as a way to mediate and enhance the coupling between microwave sources and spin qubits, which could have important implications for the sensing of isolated spins.

CHAPTER 2

THE NITROGEN-VACANCY CENTER IN DIAMOND

2.1 The resurrection of defects in semiconductors

The history of the advancements in nanotechnology is deeply tied to the progress in the understanding and application of semiconducting materials. What sets semiconductors apart from other types of materials is the possibility of widely controlling their optical and electrical properties using external perturbations or the intentional inclusion of impurities in their crystal lattice. However, in order to achieve this control it is crucial to first reduce at its minimum the concentration of unwanted impurities so that they do not dominate the effect on the characteristics of the material. This is particularly important for impurities that generate energy levels deep inside the bandgap of the semiconductor (deep impurities) as they can act as recombination centers that are not ionized even at room temperature, and therefore greatly affect the carriers lifetime and diffusion length. This is famously the case, for instance, of gold impurities in silicon[3]. It is therefore not surprising that, historically, material purification is what drove the explosive emergence of semiconductor technologies, which resulted, for instance in the success of the computing industry. Interestingly, it was precisely the attempt to reach beyond the limits of classical computing using systems governed by purely quantum mechanical behaviors that gave new life to the once dreaded deep impurities.

The emergence of quantum mechanically based computing (quantum computing, QC) was fueled by the possibility of addressing some computational problems of great practical interest that are considered intractable on classical machines, like the factorization into primes of large composite numbers for cryptography applications, or the simulation of complex quantum mechanical systems[20]. The unique feature that gives QC its capabilities is that a quantum computer can follow a superposition of computational paths simultaneously and produce a final state dependent on the interference of these paths. One key parameter for the implementation of QC is the amount of time that each computational component (quantum bits or qubits) can retain its information, which is what is identified as the *coherence* of the qubit. The need to protect the qubits from

decoherence processes associated with its interactions with the environment has been one of the main obstacle to the practical realization of QC. In the 1990s it was proposed to use trapped ions as quantum bits[22], to take advantage of their very well defined energy levels that could be used as long lived qubit states and of the possibility to obtain a good isolation from the environment and a highly efficient readout[110, 6]. Outstanding advancements have been obtained using this approach[10, 103, 105, 106, 109], but the high degree of control needed for each ion makes scaling this platform beyond few qubits, very challenging.

One way to address this problem pointed towards a rediscovery of the properties of defects in semiconductors, particularly defects that would introduce energy levels deep within the bandgap. Their most important feature is that their electronic levels maintain the discrete nature associated with atomic systems exactly because they are well separated in energy from the crystal's own states. For the same reason, their electronic wavefunction is tightly confined in space, which reduces the possibility of interacting with unwanted perturbations. Therefore, these defects show atom-like properties analogous to the ones that favor trapped ions, but they occur in a solid state system, which greatly simplifies their handling. In particular, great interest has been directed towards paramagnetic defects (defects with finite magnetic moment) as dipolar interactions can be used to couple them, and standard electron paramagnetic resonance and nuclear magnetic resonance techniques can be employed for their manipulation[160]. At the same time, it was recognized that the atom-like behavior of these systems could provide an ideal platform for nanoscale sensing purposes. For instance, the shift of the discrete spin energy levels due to Zeeman interactions can be used as a sensitive way to detect the presence of magnetic fields. Similarly, temperature variations can modify the positions of the energy levels via the lattice thermal expansion and the consequent modification of the defect's wavefunction. Therefore, as long as an efficient way to probe the position of the energy levels exists, these defects can be used to sense their local environment. In this regard, a subset of paramagnetic defects gained particular attention due to the possibility of investigating their energy level structure in a contactless matter, through measurements of their photoluminescence (PL). One in particular stood out.

2.2 Properties of the nitrogen-vacancy center

The negatively charged form of the so called nitrogen-vacancy (NV^-) center in diamond was the first paramagnetic defect in wide bandgap semiconductors to attract widespread interest for quantum applications. The detection of PL associated with single occurences of this defect in 1997[55] paved the way to the study of its intrinsic properties and allowed access to its full capabilities as single qubit systems, most of which are still unrivaled today. We mention that, while there exists also a neutral form of the NV center (NV^0) that can be isolated within the diamond lattice, there have been no demonstrations of the possibility of using this as an easily addressable quantum bit or quantum sensor. For this reason, most of the NV center's studies have focused on its negatively charged form, which is also the subject of this work. In the following we refer to the NV^- as the NV center and we focus on the properties that are relevant for room temperature sensing applications.

The NV center is a point defect within the diamond lattice comprised of a nitrogen substitutional atom and an adjacent vacancy in the diamond lattice (Figure 2.1(a)). The defect has C_{3v} symmetry and its axis can be oriented along any of the 4 directions of the $<111>$ family. The nitrogen impurity forms covalent bonds with three neighboring carbon atoms resulting in two unpaired electrons, which, together with the unpaired electrons of the carbon atoms surrounding the vacancy, are confined at the location of the defect. An additional electron, which is assumed to originate from a nearby donor, is also trapped at the NV center's site and gives the NV center its negative charge. These six electrons arrange themselves within single electron energy levels characterized by the defect's group symmetry(Figure 2.1(b)) and the resulting collective ground state of the system is a spin 1 triplet state. We note that most of the properties and the phenomena described in what follows can be interpreted considering the NV center complex as a single atom-like particle with spin S=1. Following this approach, we portray the energy level structure of the NV center in terms of a ground and an excited electronic S=1 states separated by $\sim$1.95 eV within the $\sim$5.5 eV diamond bandgap (see Figure 2.1(c)). Contrarily to the case of atoms in vacuum, these levels are accompanied by phononic sidebands that are visible as broadening in the absorption and

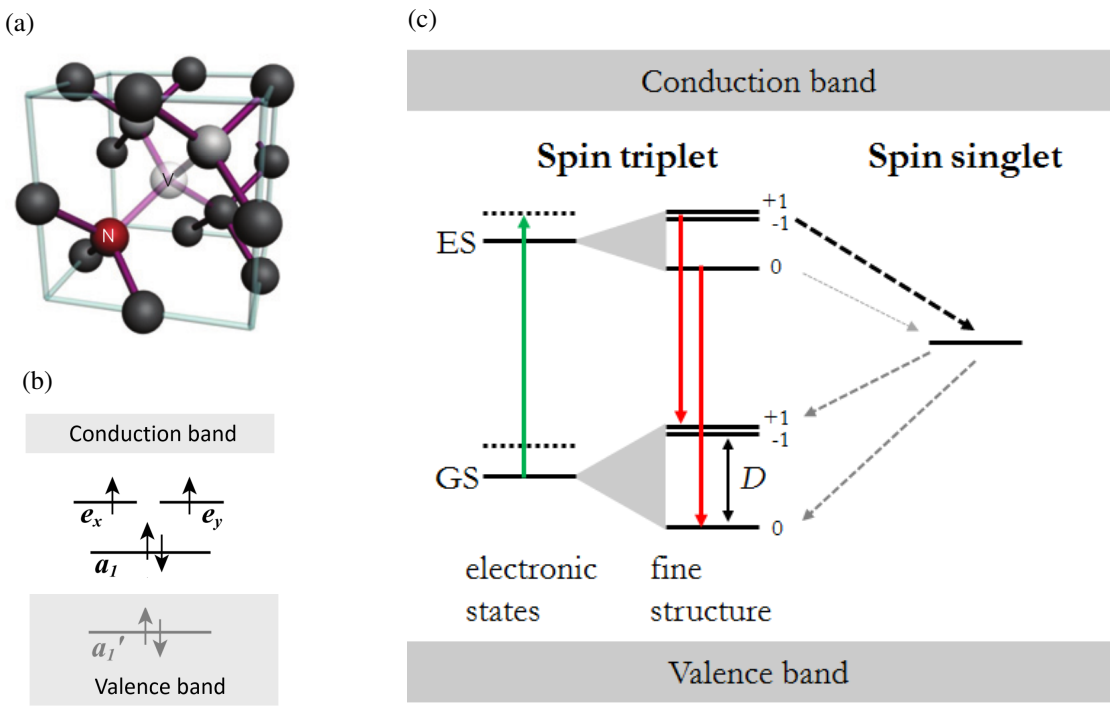

Figure 2.1: (a) Lattice structure of the nitrogen-vacancy (NV) center [4]. This defect is comprised of a nitrogen substitutional atom (red) and an adjacent lattice vacancy (translucent). (b) Occupation of the NV center's molecular-like orbitals by the siz electrons confined at the defect's site resulting in a spin triplet ground state. The symmetry of these orbitals reflects the C_{3v} symmetry of the defect. (c) Energy diagram of the electronic and spin states of the NV center. We are ignoring details of the level structure that are not relevant for our discussion. GS and ES are respectively the ground and excited electronic states. The dashed lines indicate the presence of phonon side bands. The fine structure of each electronic state is represented as a partial lifting of the spin degeneracy, where 0, +1 and -1 indicate the projection of the spin along the NV center's axis. D is the zero-field splitting in the electronic ground state. The straight green and red lines indicate radiative transitions, while the dashed lines represent the non-radiative decay through the singlet states. The thickness of these lines qualitatively represent the strenght of the relaxation channel.

emission spectrum. This property allows us to excite the NV using an optical excitation above the transition energy (this is commonly done with a green excitation at 2.33 eV, which guarantees good absorption from the NV center).

Interestingly, due to electron spin-spin interactions the spin degeneracy of the triplet states is partially lifted. This results in a zero-field splitting between the energy levels with zero (m_s = 0) and non-zero ($m_s = \pm 1$) projection of the spin along the NV center axis. In particular, in the electronic ground state the zero-field splitting D amounts to ~2.87 GHz at room temperature (we

will discuss later how the value of D depends on temperature). The presence of the zero-field splitting is of great importance as it enables the use of electron spin resonance techniques in the presence of zero or small external magnetic fields.

Another crucial feature of the NV center is the possibility of optically initializing and measuring its spin state at room temperature. To understand this we need to consider that, while optical excitations from the ground to the excited states are always spin conserving, the system relaxation can happen through two possible channels[34]. On the one side, the NV center can relax also radiatively through a spin conserving transition that has a fixed emission rate ($\sim$1/12 ns^{-1}) regardless of the initial spin state. Alternatively, the relaxation can happen through comparably long-lived ($\sim$250 ns) singlet states within the diamond bandgap (intersystem crossing), which do not originate any fluorescence within the commonly detected NV center spectrum. The coupling between these singlet states and the triplet excited state, which is currently thought to be of spin-orbit nature, is stronger when the NV center is in $m_s = \pm$ 1. On the other hand, the coupling between the singlet states and the ground triplet state is thought to be spin independent. This spin dependent relaxation has profound consequences as it provides a PL contrast between the zero and non-zero spin levels. Additionally, it allows for the polarization of the system into the m_s = 0 state through optical pumping, because the relaxation via the intersystem crossing preferentially depopulates the $m_s = \pm$ 1 states but equally repopulates all states, and the optical cycling is fast compared to the transitions between the m_s = 0 and the $m_s = \pm$ 1 levels (associated to the spin-lattice relaxation time T_1, which reaches few milliseconds at room temperature[67]).

To summarize and illustrate the practical implementation of the properties that we described, in Figure 2.2(a) we show the absorption and emission spectrum of the NV center. We highlight the possibility of pumping the defects using an off-resonant 532 nm optical excitation that initialize the system into the m_s = 0 ground state with spin polarization of $\sim$70 % to 90 %, which largely exceed the room temperature Boltzmann polarization. We can then collect the emitted broadband PL in the 630 - 800 nm range, which can easily be spectrally separated from the excitation. Figure 2.2(b) shows a typical two-dimensional PL scan of a bulk diamond sample[165] in which the NV center's

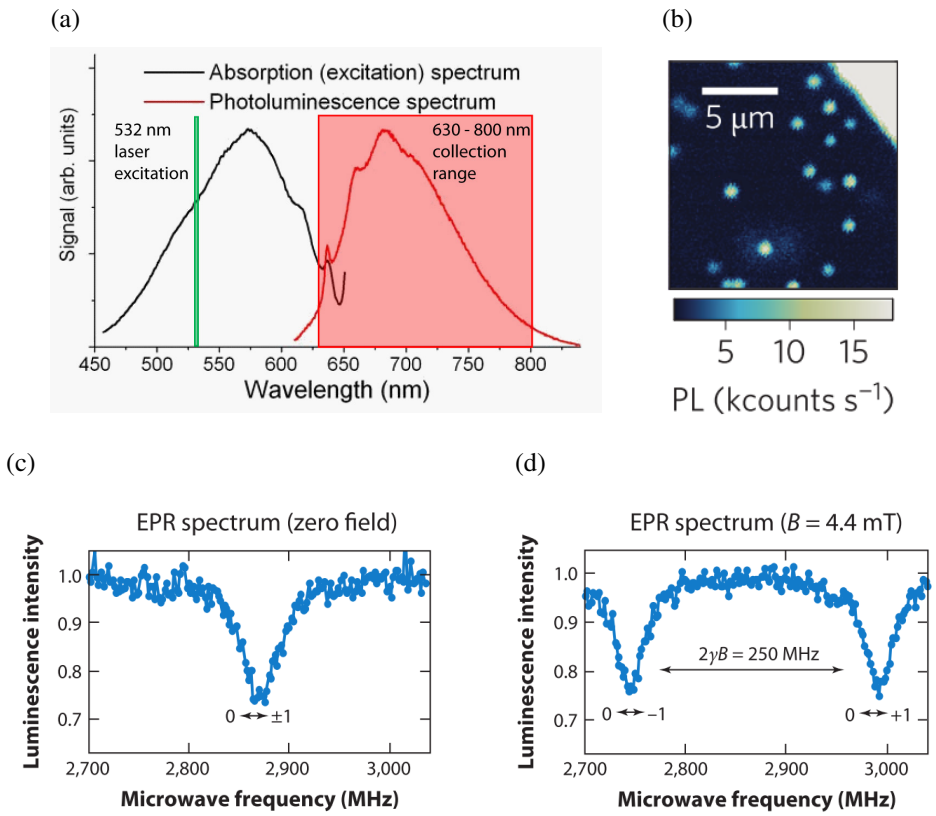

Figure 2.2: (a) Absorption and photoluminescence spectrum of the NV center (adapted from [98]). In green we indicate the position of the commonly used 532 nm off-resonant optical excitation. The red rectangle shows the detected photoluminescence spectral range. (b) Two-dimensional photoluminescence map of a diamond bulk sample[165]. The bright spots are associated with single NV centers. The bright area in the top-right corner is a part of a microwave antenna used to interact with the spin degree of freedom of the defects. (c) ODMR measurement collected on a single NV center. The drop in fluorecence indicates that the frequency of the applied microwave signal is resonant with the transition between the $m_s = 0$ and the $m_s = \pm 1$ spin states. (d) ODMR measurement collected on a single NV center in the presence of an external magnetic field, which lifts the degeneracy between the $m_s = +1$ and $m_s = -1$ states[130].

density is low enough to allow for their separate detection. The sample is continuously excited using a rastering 532 nm laser focused through an objective, while simultaneously collecting the resulting PL through the same objective.

As the PL intensity depends on the spin population in $m_s = 0$, we can then perform optically detected electron spin resonance (ESR) measurements on the NV center. The most basic of such experiments is the so-called optically detected magnetic resonance (ODMR) measurement that enables the measurement of the energy splitting between the spin states. The ODMR scheme consists

of detecting variations in the PL intensity while the frequency of an applied microwave signal is sweeped in the range of the spin transitions. When the frequency is resonant with a transition, it drives the system between the m_S = 0 and the $m_S = \pm 1$ states, which results in a drop in the PL intensity as shown in Figure 2.2(c)[130]. The ODMR measurements can be performed either under continuous optical and microwave excitations, or using pulsed pump-probe techniques, which enable the minimization of power broadening effects on the spin resonances[38]. Pulsed techniques are also the basis of more complicated ESR measurements used for high sensitivity quantum sensing applications as we will see in the following. Nonetheless, we note that the ODMR measurements that we described provides us with the basic tool to investigate the location of the energy levels of the NV center. As we mentioned above, this capability allows us to implement sensing applications.

2.3 Quantum sensing with the NV centers

To explain in more details the effect of external perturbations on the NV centers and how we can use these to perform sensing experiments, we can start from the inspection of the system's ground-state Hamiltonian H (sensing schemes at room temperature do not depend on the details of the excited state). In particular, here we focus on the effects of temperature and magnetic field perturbations. Neglecting hyperfine interaction terms that are not relevant for the purpose of this work, H can be written as:

$$\frac{H}{\hbar} = D(T)(S_z^2 - \frac{2}{3}) + g\mu_B \mathbf{B} \cdot \mathbf{S} \tag{2.1}$$

where the first term describes the zero-field splitting and the second the effect of the Zeeman interaction. $D(T)$ is the temperature dependent zero-field splitting, $g \sim$2 is the isotropic electronic g-factor, μ_B is the Bohr magneton, and $\mathbf{B}$ is the external magnetic field perturbation. As it is custom, we consider the NV center's axis oriented along the z direction. At common magnetic field ($\ll$ 100 mT), the zero-field splitting is the dominant interaction and the projection of the

NV center's spin along its axis (S_z) is a good quantum number. From eq. (2.1), we see that the energy levels are sensitive to the presence of magnetic fields and variations in temperature. In particular, in the presence of magnetic fields, the Zeeman interaction with coupling parameter $g\mu_B$ $\sim$28 GHz/T lifts the degeneracy of the m_s = +1 and m_s = -1 spin states introducing a shift of the ESR resonances that depends on the component of the external magnetic field along the NV center's axis (see Figure 2.2(d)). Both changes in magnitude and orientation can be measured and vector magnetometry can be performed by collecting measurements from NV centers with different orientations within the diamond lattice[92].

The temperature dependence of the zero-field splitting reflects instead a modulation of the interactions between the electrons confined at the defect's site when the lattice expands or contracts. Around room temperature, the response of D to temperature variations, and therefore the ESR shift, is $\sim$100 kHz/K[149].

It should now be clear that, as we have already mentioned, a measurement of the ESR frequency shifts provides a measurements of the external perturbations. The three most common approaches to detect these shifts are: the continuous-wave spectroscopy measurements that we have already introduced, the investigation of the time evolution of the spin system using pulsed ESR techniques, and measurements of the spin-lattice relaxation time (see Figure 2.3). We will briefly discuss all these in the rest of this section.

2.3.1 Continuous wave measurements

The most straightforward approach to measure the resonances' shift induced by an external perturbation is to directly collect the continuous-wave ODMR spectra and fit for the center position of the PL dips. Figure 2.3(a)) shows how this technique could be used to measure, for instance, the presence of slight variations in the external magnetic field. A more practical and precise way to perform these measurements can be used when the frequency shift is smaller than the width of the resonances and if it is possible to calibrate the sensor by measuring the position of the ODMR resonances in the absence of the perturbation. In this conditions, we can optimize the sensitivity

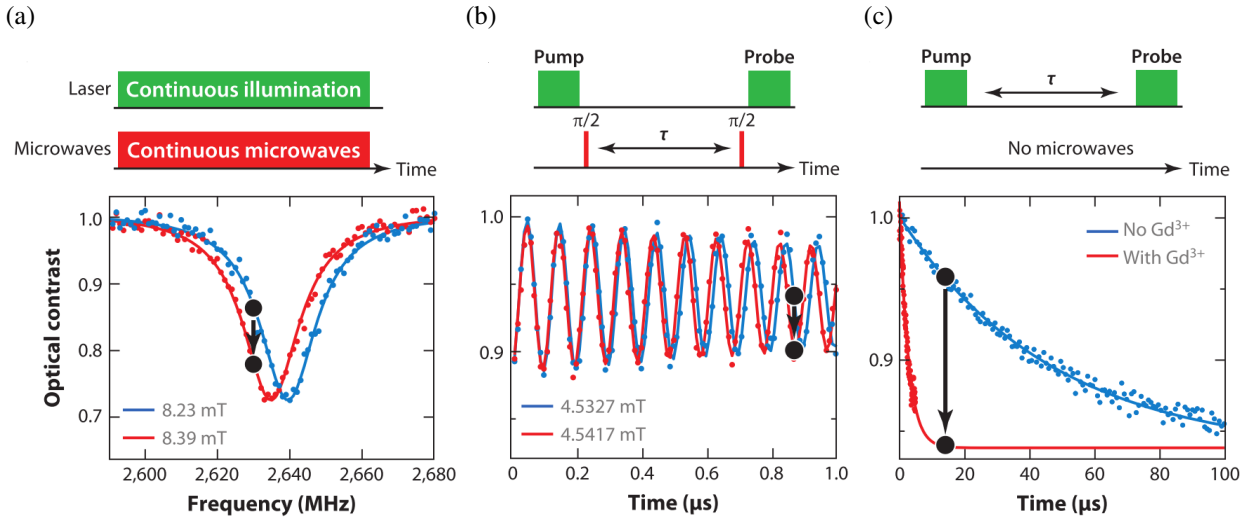

Figure 2.3: Pulse sequence diagrams (top) and example measurements (bottom) for various sensing protocols[130]. (a) Continuous wave detection of a change in DC magnetic field based on the measurement of the frequency shift of an ODMR resonance. Once the sensor is calibrated in the absence of the signal, the measurement reduces to the detection of variation in the emitted photoluminescence at a fixed applied microwave frequency. (b) Pulsed DC magnetometry using a Ramsey scheme. After initialization in the $|0\rangle$ state, the NV center spin is brought into a superposition of $|0\rangle$ and $|1\rangle$ using a resonant microwave pulse. This new state acquires a phase proportional, for instance, to the magnetic field to be measured, which can then be converted in variations in the population of $|0\rangle$ with another microwave pulse. After calibration of the sensor, the measurement translates into the detection of variations in the photoluminescence for a fixed delay time between the microwave pulses of the measurement's sequence. (c) Detection of magnetic noise through its effect on the spin-lattice relaxation time of the system. The relaxometry measurements are obtained by first initializing the NV center in $|0\rangle$ and then probing the population remaining in this state after a variable delay time τ. The data shows the relaxation dynamics of a NV center in the presence and absence of paramagnetic $GdCl_3$ salt. Again the measurement can reduce to the detection of photoluminescence changes at a fixed time between the initialization and the read-out of the NV center.

by recording variations in the PL amplitude at a fixed microwave frequency coinciding with the point of maximum slope of the resonance curve. We can define the minimum detectable frequency shift Δf_{min} as the one that provides a signal-to-noise ratio $\Delta PL/\sigma_{PL}$ of one, and in the case of shot-noise limited measurements we can write

$$1 = \frac{\Delta PL}{\sigma_{PL}} = \frac{\Delta I\, t}{\sqrt{I_0\, t}} = \frac{\left(\frac{dI}{df}\right)_{max} \Delta f_{min}\, t}{\sqrt{I_0\, t}} \tag{2.2}$$

where I is the photon count rate in number of detected photons per second, I_0 is the photon count rate in the absence of the perturbation and t is the measurement time. Considering a Lorentzian resonance line with contrast C and half width at half maximum Γ we obtain:

$$\Delta f_{min} = \frac{1}{\sqrt{3}} \frac{\Gamma}{C\sqrt{I_0 t}} \tag{2.3}$$

For a single NV center with typical $\sim$30 % contrast, linewidth of 10 MHz, and photon count rate of 5×10^4 s^{-1}, we obtain Δf_{min} $\sim$50 kHz for a 1 s integration time. This is equivalent to a magnetic field and temperature sensitivity of:

$$\eta_B = \delta B_{min} \sqrt{t} = 2\,\mu\text{T/Hz}^{1/2} \tag{2.4}$$

$$\eta_T = \delta T_{min} \sqrt{t} = 0.5\,\text{K/Hz}^{1/2} \tag{2.5}$$

These sensitivities are mainly limited by the resonance linewidth, which is ultimately bounded by the spin dephasing time of the spin system T_2^*. This dephasing is due to the presence of noise in the environment, which affects the instantaneous position of the ESR resonances resulting in an effective broadening. Nevertheless, it is usually challenging to reach this sensitivity limit experimentally because both the readout laser and the driving MW field induce an additional power broadening of the ESR line[38]. To circumvent this problem, we can separate in time the processes of spin initialization, manipulation, and readout as described later for the case of pulsed measurements.

From equation (2.2) we can also conclude that measurement's sensitivity could be greatly improved by simultaneously collecting PL from an ensemble of NV centers, which would increase the photon count rate at the expense of a worse spatial resolution. For this reason, for measurements where the perturbation to be measured does not change on a nanometer scale, ensemble measurements are usually convenient. However, it should be noted that measurements are usually performed in the presence of an applied external magnetic field to separate the resonances associated with the different NV centers' orientations. This is usually done to minimize the effective

resonance linewidth, which, at small field, is affected by strain in the crystal and by the different response of the various NV center's orientations to the magnetic field. When we then focus on one of the spectrally resolved resonances only one specific NV center orientation is relevant for the measurement but we still collect PL from all the defects in the probed volume. This therefore results in a decrease of the PL contrast, which partially reduces the sensitivity. Various studies have attempted to address this limitation in recent years, and reports of diamond samples with NV centers moslty aligned in one direction have appeared[40, 85, 47, 117].

2.3.2 Pulsed measurements

As mentioned above, pulsed experiments based on pump-probe schemes can provide a more sensitive approach than continuous wave measurements. The advantage of these techniques is that the NV centers are not optically pumped during the sensing period, and advanced magnetic resonance techniques can be used to greatly extend their coherence time, which, as we have seen, affects the achievable sensitivity. In the following, we assume that an external magnetic field is applied to lift the $m_S = \pm 1$ degeneracy and we consider a closed two-level subsystem comprised of the m_S = 0 and m_S = -1, identified respectively as $|0\rangle$ and $|1\rangle$. The description of the spin dynamics is relative to the frame of reference that rotates at the Larmor frequency of the equivalent Zeeman splitting between $|0\rangle$ and $|1\rangle$.

The simplest pulsed sequence used to perform nanoscale sensing is the so-called Ramsey (or free-induction-decay) sequence, which is represented in Figure 2.3(b) in its implementation as a pulsed magnetometry scheme[144]. The NV center is first initialized into the $|0\rangle$ state by applying a laser pump pulse. A first resonant microwave (MW) pulse ($\pi/2$ pulse) is then applied to rotate the spin to a coherent superposition $|\psi\rangle = \frac{1}{\sqrt{2}}(|0\rangle + |1\rangle)$, which then evolves over a time τ. During this time, the NV center's spin interacts with the target magnetic field. While the $|0\rangle$ state is not affected by the presence of the field, the $|1\rangle$ state acquires a phase $\phi = \tau g \mu_B B/\hbar$, corresponding to a precession in the plane perpendicular to the spin quantization axis, resulting in $|\psi\rangle = \frac{1}{\sqrt{2}}(|0\rangle + e^{i\phi}|1\rangle)$. A second $\pi/2$ pulse converts the relative phase between $|0\rangle$ and $|1\rangle$

into a population difference, which is then read out optically, yielding information on the Zeeman shift induced by the target field. For small ϕ, the signal S (change in PL with respect to the initial $|0\rangle$ state) depends linearly on the phase shift and therefore on the magnetic field through $S \approx \phi = \tau g \mu_B B/\hbar$. In Figure 2.3(b), the signal obtained as a function of τ for two different values of the total magnetic field is shown, which also illustrates the working principle of the Ramsey measurements. The implementation of the magnetic field detection would simply require measuring variations in the PL at a selected value of τ that allows for a detectable change in signal to appear. This principle would suggest that increasing the spin evolution time could indefinitely improve the sensitivity. However, there is a limit to the maximum possible value of τ because of the presence of noise in the system, which randomizes ϕ over time with characteritic time T_2^* and results in a reduction of the read-out contrast with increasing τ. It is possible to show[144] that the optimal compromise between read-out contrast and acquired phase happens for $\tau \approx T_2^*$. It should also be noted that, in these pulsed measurements, the photon count rate is decreased because of the finite pulse sequence duty cycle (photons are collected only during the first few hundreds of nanosecond of the readout pulse) and this is also a factor in determining the optimal value of τ. Considering a pulse sequence with $\tau = T_2^*$, laser readout time t_L, and total measurement time t (the number of averaged sequences will be $\sim t/T_2^*$), we can write the (shot-noise limited) minimum detectable field variation as:

$$\Delta B_{min} = \frac{\hbar}{g\mu_B} \frac{1}{C\sqrt{I_0\, t_L}} \frac{1}{\sqrt{T_2^*\, t}} \tag{2.6}$$

where $0 < C < 1$ is the signal contrast at $\tau = T_2^*$ ($C = 1$ at $\tau = 0$). For a NV center with a typical spin dephasing time $T_2^* \approx 1\,\mu s$, and considering currently achievable experimental conditions [126], the optimal sensitivity $\eta_B = \Delta B_{min}\sqrt{t}$ reaches $\approx 0.4\,\mu T\ Hz^{-1/2}$.

The Ramsey sequence is a measurement technique sensitive to static signals, but if we instead want to detect oscillating perturbations more advanced coherent control techniques, called dynamical decoupling techniques, can be used. These commonly address signals in the kilohertz to megahertz range (limited by the fastest achievable coherent control of the NV center's spin) and provide a further extension of the sensing capabilities of the NV centers by decoupling its

spin from the effects of slowly oscillating noise contributions. As the main source of noise in diamond tends to be the dipolar coupling of the NV center with other spins provided by impurities or by intrinsic ^{13}C nuclear spins, and because the correlation time of this kind of noise is long on the timescale of the NV center's spin manipulation, dynamical decoupling techniques can greatly extend the coherence time by suppressing these contributions. In practice, the simplest of these decoupling protocols is the ''Hahn echo" sequence, where, compared to the Ramsey sequence previously described, a resonant microwave π pulse is introduced a time $\tau/2$ after the first $\pi/2$ pulse. The result is to swap the phase aquired by the $|0\rangle$ and $|1\rangle$ states

$$\frac{1}{\sqrt{2}}(|0\rangle + e^{i\phi}|1\rangle) \rightarrow \frac{1}{\sqrt{2}}(e^{i\phi}|0\rangle + |1\rangle) \tag{2.7}$$

Magnetic field noise with correlation time that is long compared to τ will induce the same dephasing in the second half of the pulse sequence, therefore compensating the effect of the first half of the free evolution. The extended spin coherence time is commonly known as homogeneous coherence time T_2 (to contrast with the inhomogeneous coherence time T_2^*) in reference to the terminology used in the NMR community, where dynamical decoupling techniques were employed to reduce the effects of inhomogeneity in the field applied to ensembles of spins. In essence, dynamical decoupling techniques extend the optimal measurement interrogation time from T_2^* to T_2 at the expense of a reduced bandwidth and insensitivity to frequency smaller than $1/\tau$. We note that, while it is clear that these techniques are highly valuable in situations where the frequency of the signal is known, they also provide an equal performance for the detection of the variance of a signal of unknown frequency and varying phase, provided that the time correlation of the variance is long compared to the measurement interrogation time [144]. In both cases the sensitivity improves by a factor of $\sim \sqrt{T_2^*/T_2}$ with respect to the case of DC magnetometry. Relying on this improved sensitivity, it was possible in recent years to image the magnetic field of a single electron spin[53] and detect small ensembles of nuclear spins[95, 140].

While the optimal sensitivity of the Hahn echo measurement is achievable only for signals oscillating at frequency $1/T_2$, these results can be extended to faster oscillating fields by using se-

quences with a higher number of pulses. In particular, the Carr - Purcell - Meiboom - Gill (CPMG) sequence, which involves the addition of multiple π pulses between the initial and final $\pi/2$ pulses, allows to obtain optimal sensitivity also for signals having frequencies that are multiples of $1/T_2$. This also results in a further narrowing of the measurement bandwidth and, consequently, longer spin coherence times. Finally, as mentioned earlier for the case of the ODMR based measurements, the sensitivity can be further extended using ensembles of dense NV centers to improve the signal to noise ratio of the measurements. We note that, even though we mostly focused on the specific description of magnetometry applications, analogous protocols have been developed for the sensing of temperature variations[112, 148].

2.3.3 Spin-lattice relaxometry measurements

Signals at frequencies in the megahertz to gigahertz range can be detected using spin relaxometry techniques, which take advantage of the dependence of the spin-lattice (or longitudinal) coherence time T_1 on the amount of magnetic noise in the system at the spin transition frequency. In essence, the component of this noise orthogonal to the NV center's axis can drive precessions of the spin, therefore effectively reducing its T_1 time. In Figure 2.3(c) the principle of this measurement is illustrated for the case of NV centers in the presence of a solution containing Gd^{3+} ions[142]. A green excitation pulse is applied to prepare the NV center in $|0\rangle$ and then, after an evolution time τ, a read out pulse is applied to detect the remaining $|0\rangle$ population. The faster relaxation time is due to the gigahertz magnetic field fluctuations introduced by the movements, interactions, and relaxations in the gadolinium spin bath. As in the previous cases, once the system has been calibrated in the absence of the perturbation, the measurement can be performed by detecting changes in the PL at a fixed value of τ, and the maximum sensitivity increases the larger T_1 is[142]. For signals in the gigahertz range this technique has proven very sensitive (reaching ~ 1000 statistically polarized spins), and the possibility of using only optical pulses make these measurements particularly appealing.

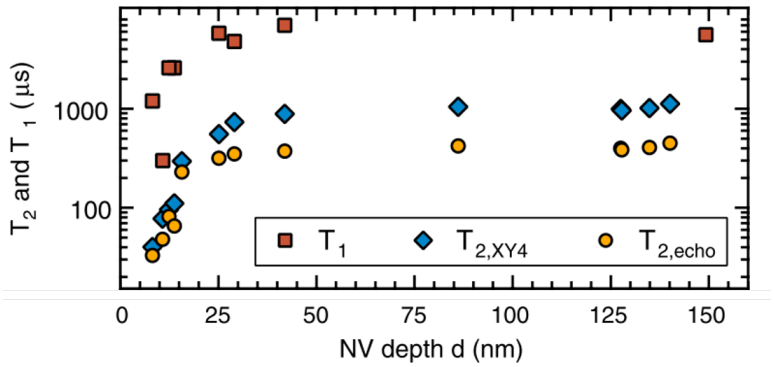

Figure 2.4: Coherence times T_2 and T_1 versus the NV center's depth (adapted from[108]). T_2 was collected both with a Hahn-echo and a $XY4$ protocol, which is equivalent to a CPMG protocol but with 2-axis rotations[159].

2.4 Effect of the interfaces

One common thread in the discussion presented in the previous section is the importance to have long NV center spin coherence times to achieve optimal sensitivities. Even in measurements that benefit from the higher signal-to-noise ratio of ensembles of NV centers with shorter coherence times, it is still crucial to ensure that the coherence is limited only by the higher density of NV center's spins and not by other sources. However, in our analysis we have so far neglected the effect of the spatial variation of the sample's signal, which can have important implications on the achievable sensitivity and spatial resolution. This is particularly clear in the case of measurements that aim at detecting few spins residing on the diamond's surface. The magnetic field generated by these spins is a dipolar field that decays sharply with the distance r from the source (the magnetic field generated by a single electron at a distance of 50 nanometers is only a few nT[53]), which means that the distance between the NV center sensor and the diamond surface d needs to be as small as possible in order to optimize both the sensitivity and the spatial resolution. Indeed, because the signal decays as $1/r^3$, the spins contained in a volume $\sim d^3$ create an indistinguishable signal at the location of the NV center[140]. On the other hand, the proximity to the surface strongly reduces the coherence properties of the NV center as it is illustrated in Figure 2.4[108, 114]. This effect has been associated with the presence of magnetic and electric field noise with a correlation time

faster than the one for bulk spin bath, and that is introduced by electronic spins present on the diamond surface[108, 72]. We can therefore conclude that, in nanoscale sensing applications where the detected signal is highly spatially dependent, it is of great importance to be able to precisely control the position of the NV centers to optimize sensitivity and spatial resolution.

We note that the considerations presented in this section are less relevant for temperature measurements as the high thermal conductance of diamond results in a fast thermalization of the lattice. In this case a fine spatial resolution can be recovered with the use of diamond nanoparticles, which can be beneficial more in general to perform sensing in complex systems as previously mentioned. In the next chapter we will discuss in details the advantages and limitations of using these nanoscale systems for sensing applications.

CHAPTER 3

FABRICATION AND LIMITS OF DIAMOND NANOPARTICLES

As we have seen in the previous chapter, the NV center constitutes a unique platform for the implementation of high sensitivity quantum sensing measurements at the nanoscale. However, a great number of sensing applications requires for the qubits to be embedded within micro- and nanoscale particles. We mentioned in Chapter 1, how this allows for the sensors to be introduced within a biological[79], or fluidic environment[62, 49] and perform contactless measurements. Additionally, the nanodiamonds (NDs) can be integrated with scanning probe techniques to obtain ultra-high spatial resolution sensing of magnetic systems [29, 125, 145]. Finally, nanoparticles have very small thermal masses ($\sim$ fJ/K), which is of great importance, particularly in temperature sensing measurements where adding additional heat dissipation channels in the system could be particularly detrimental.

These advantages, together with the good photostability[169] and biocompatibility[132], contributed to the growing interest in the study and fabrication of these nanoparticles for a wide range of applications[104]. In the following we are briefly reviewing the fabrication techniques of commonly available NDs and the relevant properties for quantum sensing applications.

3.1 Typical fabrication processes

We are going to focus on the two techniques that have been used to obtain the diamond nanoparticles used in most applications to date. We note that a complete analysis of the properties of the NDs resulting from these fabrication techniques is complicated to obtain and depends on their size, shape, surface chemistry and purification method[104]. All these parameters can influence, for instance, the particles' surface termination and their stability in solution but the analysis of these details is beyond the scope of this work.

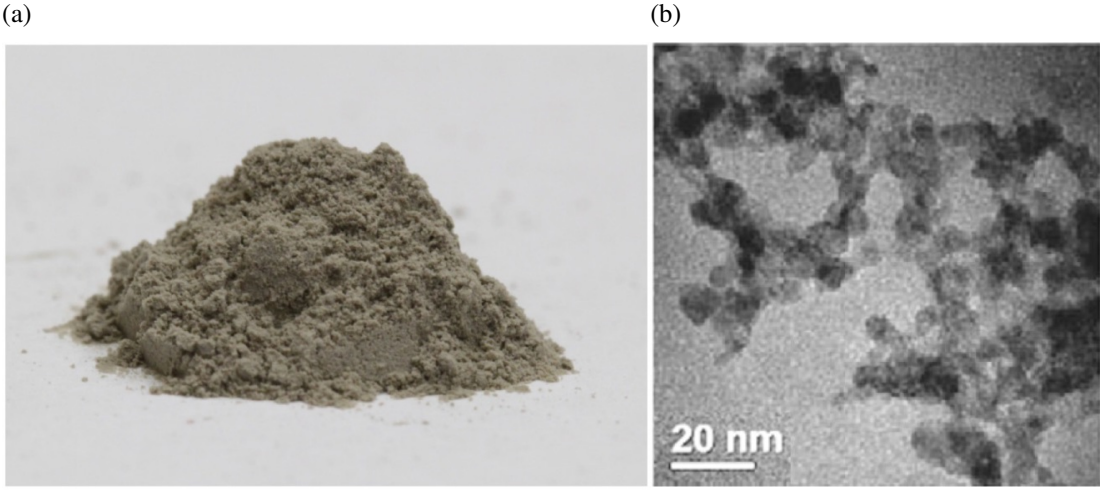

Figure 3.1: Detonation nanodiamonds. (a) Optical image of nanodiamond powder. (b) TEM image of an ensemble of nanoparticles[44].

3.1.1 Detonation technique

This technique was first developed in the 1960s[27] in the USSR but went unexplored until it was rediscovered at the end of the 1980s[52]. It involves the detonation of molecules of explosives in a closed chamber filled with inert gas or water coolant. The result is a mixture of diamond particles 4 nm to 5 nm in diameter and other carbon allotropes and impurities. The higher the cooling capacity, the larger the diamond yield, which can reach 75% in weight. An alternative technique makes use of the shock wave of an explosion to produce NDs from graphite and generates particle larger than 10 nm. The residual component of the detonation product contains graphitic carbon and incombustible impurities like metals coming from the explosives molecules or the walls of the detonation chamber. For most applications the powder needs to be purified, which usually involves the use of autoclave boiling acid or oxidation in air processes[104]. In Figure 3.1(a) a typical image of the final commercially available detonation ND powder is shown. Figure 3.1(b) is a high magnification transmission electron microscopy (TEM) image of an ensemble of these nanoparticles. The crystals tend to aggregate in micrometer-sized clusters that are hard to separate because of a very strong inter-particle adhesion force[104].

Numerous defects are present in detonation nanoparticles, both structural and compositional.

As a result of the explosive mixture being rich in nitrogen, a sizable (1 part per million) presence of nitrogen paramagnetic impurity is present in the nanocrystals. In addition, the presence of a graphitic shell surrounding the NDs is common. Finally, various structural defects are present, the most common being crystal twinning[65].

Until recently, diamond nanoparticles synthesized with this technique were not commonly investigated for applications in which the PL properties are important, but in recent years blinking NV center PL has been observed in 5 nm detonation NDs[13]. Additionally, stable NV center PL was detected in larger (> 20 nm) NDs[157]. Nevertheless, the PL intensity in these nanoparticles is commonly low due to size-related proximity of surface defects and the presence of internal structural defects, which can act as trap states and modify the band structure of the material in the proximity of the NV centers. For this reason, most applications requiring bright particles have relied on different synthesis techniques.

3.1.2 Ball milling technique

Nanoparticles obtained with this technique are currently the most commonly used in applications requiring coherent control and read-out of the NV centers due to their strong and stable PL properties. The fabrication process starts in this case from a synthetic micro diamond powder (> 20 µm to 50 µm) obtained from type Ib high pressure high temperature (HPHT) material grown from metal catalysts[12]. This material naturally contains nitrogen impurities that originate from the solvent metal, carbon source material, and residual gas in the reactor. The nitrogen atoms are incorporated as substitutional impurities and remain isolated for thermokinetic reasons. Irradiation with photons, electrons, ions, or neutron is then used to introduce vacancy in the lattice, and a subsequent annealing process in vacuum at $\sim$800 °C mobilizes the vacancies that migrate and combine with the immobile nitrogen atoms. Finally, a ball milling process is used to reduce the size of the particles to between few nanometers and few hundred nanometers (see Figure 3.2(a)). To remove the metal impurities introduced during the milling process, an acid treatment is commonly used, which is critical for the stability of the NV centers.

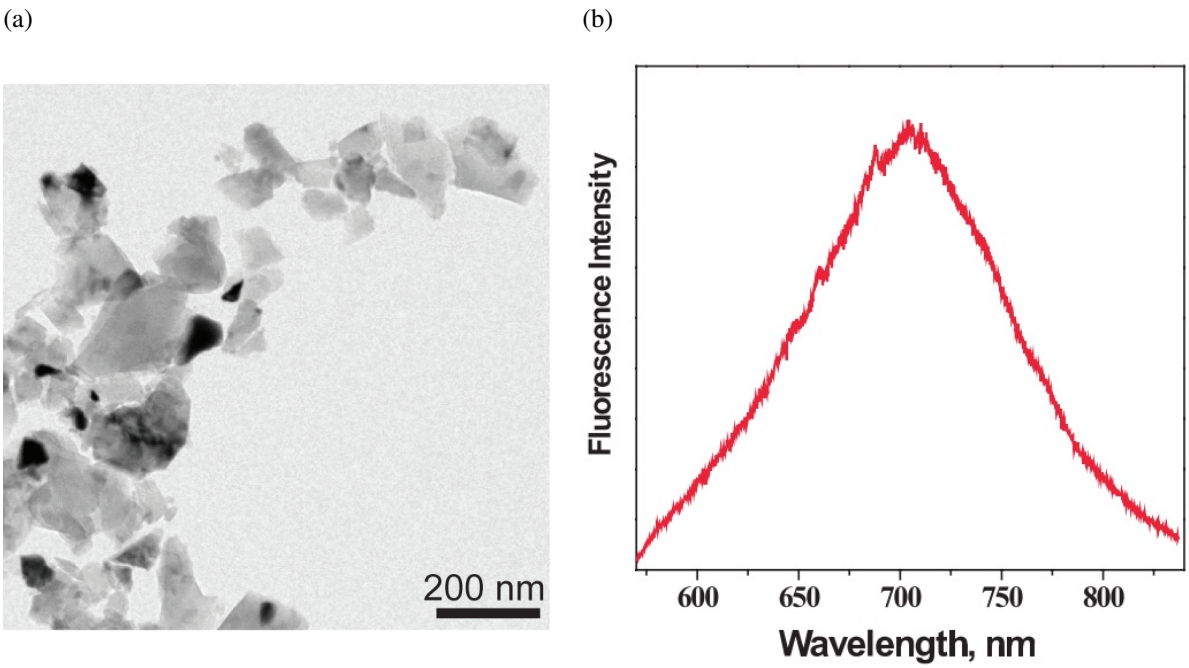

Figure 3.2: Ball milled nanodiamonds. (a) Scanning electron microscopy image of an ensemble of ball milled nanodiamonds (Adámas Nanotechnologies, Supplementary Information of [62]). (b) Typical photoluminescence spectrum of a ball milled nanodiamond containing an ensemble of NV centers not showing the characteristic zero-phonon line[12].

As we mentioned, nanoparticles obtained through ball milling techniques offer good and stable PL properties[12]. However, high energy milling processes introduce a high density of crystal dislocations[153]. Additionally, the resulting crystals are heavily strained. This is clearly reflected in the PL spectrum of a ND containing multiple NV centers shown in Figure 3.2(b). Here the zero-phonon emission line is not visible due to the inhomogeneous broadening of the optical transition induced by the varying strain across the nanoparticle[143]. We note that the strain also influences the value of the observed zero-field splitting[35, 147], resulting in a broadening of the NV center's ground state spin transitions. This is of particular importance for sensing measurements with ensembles of NV centers as it reduces the achievable spin read-out contrast and sensitivity. In the following we discuss in more details the properties of the NV centers in nanodiamond for quantum sensing applications.

3.2 Challenges to sensing with nanodiamonds

As discussed in the previous chapter, the NV centers' sensitivity is intrinsically tied to its spin dynamics properties. Unfortunately, NV centers in NDs persistently exhibit short spin coherence times, with values of T_2, measured with a standard Hahn-echo sequence, that do not usually exceed $\sim$10 µs (see Figure 3.3(a)). These short coherence times are likely associated with the presence of dense electron-spin baths at the surface of the NDs[147], or at the location of lattice dislocations in the crystal. Additionally, a clustering of the nitrogen impurities near the surface of the nanocrystal has been proposed as an additional dephasing mechanism[82]. The strong dipolar interactions within this strongly confined bath result in a rapid magnetic field fluctuations with short correlation time. This could explain the very limited enhancement of the spin coherence time that is usually achieved using advanced dynamical decoupling (DD) techniques[111, 82], which, as we have previously discussed, cannot eliminate the effect of rapidly oscillating noise. Alternatively, this effect can be explained as the result of very short spin-lattice relaxation times[111], which is again due to the presence of fast magnetic field oscillations and set an upper boundary for the spin coherences.

While addressing the effect of the surface spin-bath is challenging as it would require a detailed knowledge of the NDs' surface states, efforts to suppress the effect of nitrogen impurities can be more easily undertaken. In [75], Knowles *et al.* used NDs obtained from high-pressure high-temperature bulk diamond with nitrogen impurity concentration intermediate to type Ib ($\sim$200 ppm) and type IIa ($<$ 5 ppb) categories to guarantee low impurity concentrations while still providing a significant percentage (few percent) of nanoparticles that contain NV centers. For this kind of nanoparticles the dominant noise source is believed to be associated to a quasi-static bath of paramagnetic impurities in the crystal, which could be related to sparse ^{13}C or nitrogen impurities, rather than to the rapidly evolving surface states. This results in a clearer improvement of the spin coherence with the use of a CPMG-type pulse sequence (see Figure 3.3(b)). Nevertheless, the longest achieved value of T_2 is still limited to $\sim$67 µs, obtained with a 71-pulse sequence, which is highly impractical for sensing purposes as it strongly limits the bandwidth of the sensor.

The short coherence of the NV centers is not the only limitation to the use of currently available

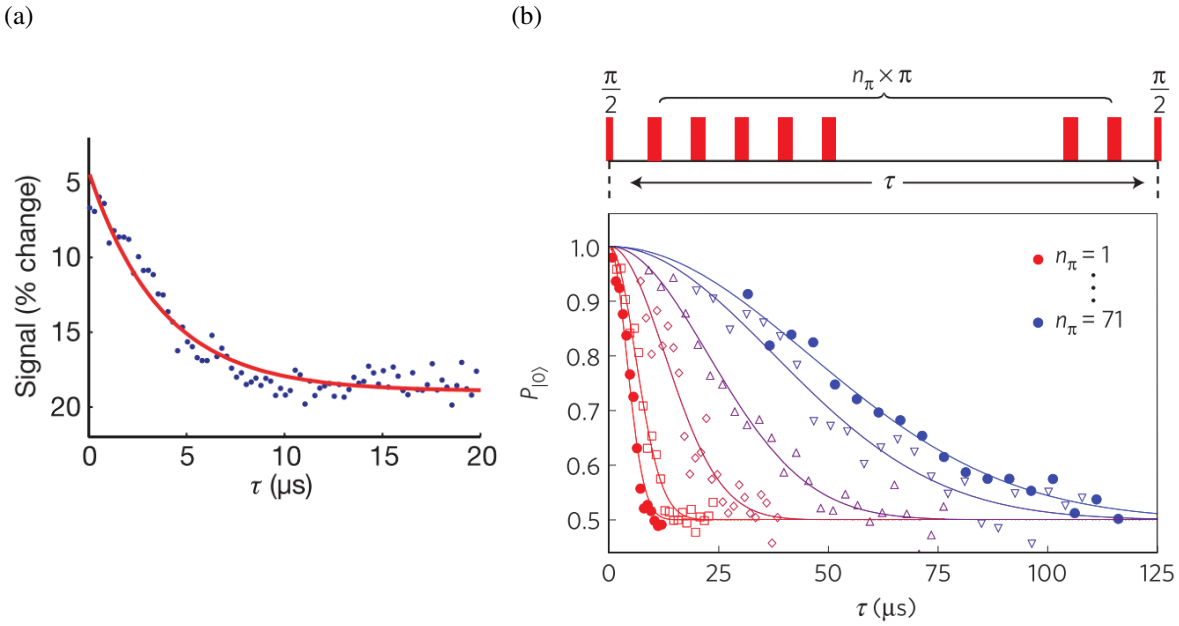

Figure 3.3: (a) Hahn-echo signal for a single NV center in a 30 nm-size nanocrystal showing a decay time of ∼4 μs[100] typical for milled nanoparticles. The signal is plotted as a fractional change of the NV center fluorescence. (b) Echo curves collected on a single NV center in a ∼20 nm-size nanoparticle plotted in terms of the $|0\rangle$ state population. A growing number of pulses in the CPMG-type dynamical decoupling pulse sequence (*top*) was used. The curves shown correspond to n_π = 1,3,9,21,51,71 and they are fit to exp(-$\tau/T_{2,DD}$)[75].

NDs for sensing applications. As mentioned earlier, it is of great importance to be able to precisely position the NV centers with respect to the diamond interface, especially when measuring signals with fast spatial decay, but this is obviously not achievable with the fabrication techniques described in this chapter. Additionally, through the detonation and milling techniques it is not possible to control shape, size, and crystal orientation of the nanoparticles. As a result, it is challenging to consistently obtain nanoparticles containing the same numbers of NV centers or achieve consistent alignment of the defects with respect, for instance, to an external magnetic field. Furthermore, the radiative lifetime of the electronic excited state of the defect increases from approximately 12 ns in bulk diamond[97], to approximately 25 ns in randomly shaped nanodiamonds[9], owing to changes in the effective refractive index. Finally, optically trapped nanodiamonds have been proposed as contactless sensors in fluidic environments, but the random geometry compromises their stability and orientation in the trapping volume, hindering their sensing potential. Indeed,

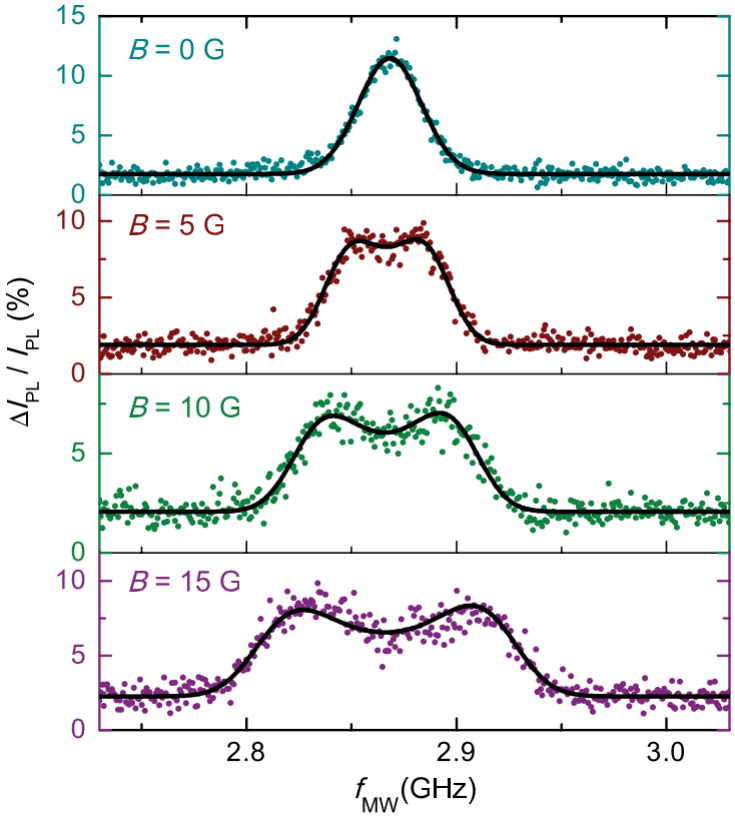

Figure 3.4: ODMR spectra of ensembles of optically trapped milled nanodiamonds (NV-ND-100nm, Adámas Nanotechnologies). Contrary to what has been shown so far, the resonances are here represented as positive variations in the photoluminescnece (ΔI_{PL}) with respect of the signal collected when the microwave field is not resonant with the NV centers' spin transitions (I_{PL}). The best-fit curve was obtained using a model that considers the NV centers' orientation averaged over the whole spherical angle[62]. It is clear that, because of the chaotic motion of the NDs in the optical trap, it is not possible to fully resolve distinct NV center resonances and the effective width of the peaks is considerably broadened.

when working with commercial nanodiamonds, a small size ($\leq$ 100 nm) is necessary to obtain well-localized NV centers that are close to the particle surface. However, nanoparticles of this size are considerably smaller than the common trapping volume ($\sim$1.5 μm^3) determined by the beam waist and Rayleigh length of the focused trapping laser. This means that many nanodiamonds can occupy the trap at one time, and that the dynamics of the system are complicated by additional particles leaving and joining the trap during a measurement[62]. In addition, this ensemble of particles continuously revolve within the trap, as no preferential trapping axis is established. This chaotic motion results in a continuous precession of the NV centers' axis with respect to, for instance,

an external target magnetic field. It was shown[62] that the overall effect of this movement is an extensive effective broadening of the ODMR resonances (see Figure 3.4), which strongly limits the achievable DC sensitivity (see section 2.3.1). Additionally, the random tumbling and rotating motion precludes the use of high sensitivity dynamical decoupling techniques as the NV centers' spin rapidly changes orientation with respect to the applied microwave control field.

To address the limitations that we presented in this chapter, it is necessary to create nanodiamonds with high crystal quality, precisely engineered geometry, and controlled NV center density and positioning. In the next chapter we will describe a fabrication technique that we developed to address these goals.

CHAPTER 4

ENGINEERED MICRO- AND NANOSCALE DIAMONDS AS MOBILE PROBES FOR HIGH-RESOLUTION SENSING IN FLUID

In this chapter we are going to introduce the fabrication process that we developed to create diamond micro- and nanoparticles (for simplicity we will simply call these nanoparticles and nanodiamonds in the following) with properties that allow us to go beyond the limitations detailed in the previous chapter. Our approach combines a high quality diamond epitaxial growth[114] with an established technique for diamond membrane fabrication[93], along with electron beam lithography to pattern the NDs with finely tuned shapes and sizes. The use of diamond membranes is crucial to obtain an efficient release of the particles in suspension at the end of the fabrication process. With this fabrication process we obtain NV centers with long spin coherence times embedded with controlled density and spatial distribution within single-crystal NDs, of engineered shape and size.

Specifically, we fabricate cylindrical nanoparticles (diameters ranging from 100 nm to 700 nm and lengths from 0.5 µm to 2 µm) incorporating single NV centers exhibiting consistently high Hahn echo coherence times ($T_{2,Hahn}$ $\sim$100 µs on average) up to $\sim$360 µs. The coherence can further extended to $\sim$710 µs using more advanced dynamical decoupling techniques. Additionally, we fabricate high-photoluminescence (PL), high-aspect-ratio NDs and use them for magnetometry experiments inside of a microfluidic circuit using an optical trapping apparatus. We show that the control over the particles geometry is crucial in achieving long-term (over 30 hours) trapping and orientation stability. These results pave the way for magnetic field and temperature mapping with bulk-like sensitivity in solution.

In the following we will first describe the details of the fabrication process, the analysis of the particles' crystal quality, and the procedure that allows us to release the NDs in solution. Subsequently, we will analyze the PL and spin properties of the NV centers contained in the nanoparticles. Finally, we will discuss the results of the magnetometry measurements in solution.

4.1 Nanodiamond fabrication

4.1.1 Growth of of high-quality delta doped diamond

The fabrication process begins with a 4 by 4 mm electronic grade (type IIa) diamond substrate (Element Six, [100] surface normal), on which we perform helium implantation using 1 MeV ions to create a disordered layer $\sim$1.7 μm below the surface (Figure 4.1(a)). This disordered layer allows us to release the membranes from the substrate later in the process[93].

A high quality diamond film is then grown on the ion-implanted substrate with an epitaxial plasma enhanced chemical vapor deposition (PECVD) process (Figure 4.1(b)). During the growth, nitrogen gas is intentionally introduced in a controlled fashion to introduce impurities in the crystal[114]. Purified ^{15}N ($> 98\,\%$) is used to be able to distinguish the NV centers formed in this grown film from those due to naturally occurring ^{14}N impurities (99.6 % isotopic abundance) in the substrate. We will explain in a later section how this analysis is performed.

By varying the growth conditions it is possible to span a considerable range of material thickness, structural quality, and NV center densities and depth positioning. In particular we fabricate material using two extreme sets of conditions. On one side (growth structure #1) we use a fast growth ($\sim$50 nm/min) using gas containing non-isotopically purified carbon (2000 W, 165 torr, CH_4/H_2 1%). ^{15}N is uniformly introduced during the whole growth process using a steady flow of $^{15}N_2$ (0.1 sccm), which translates in a highly uniform content of nitrogen impurities through the thick (1.0 μm to 1.5 μm) CVD material.

Alternatively (growth structure #2), we use ^{12}C isotopically purified gas (99.999 % ^{12}C content) and a slower growth (750 W, 25 torr, $^{12}CH_4/H_2$ 0.025%, $\sim$10 nm/h). This recipe allows us to obtain a material with a very low level of structural defects and paramagnetic impurities (^{12}C has a spin 0 nucleus), which is conducive to high spin coherence times. The nitrogen gas is introduced for a precisely controlled amount of time during the growth to obtain a delta-doped heterostructure consisting of [100 nm ^{12}C diamond] / [6 nm ^{15}N doped ^{12}C diamond] / [100 nm ^{12}C diamond].

The two types of growth provide us with materials with high and low NV center content re-

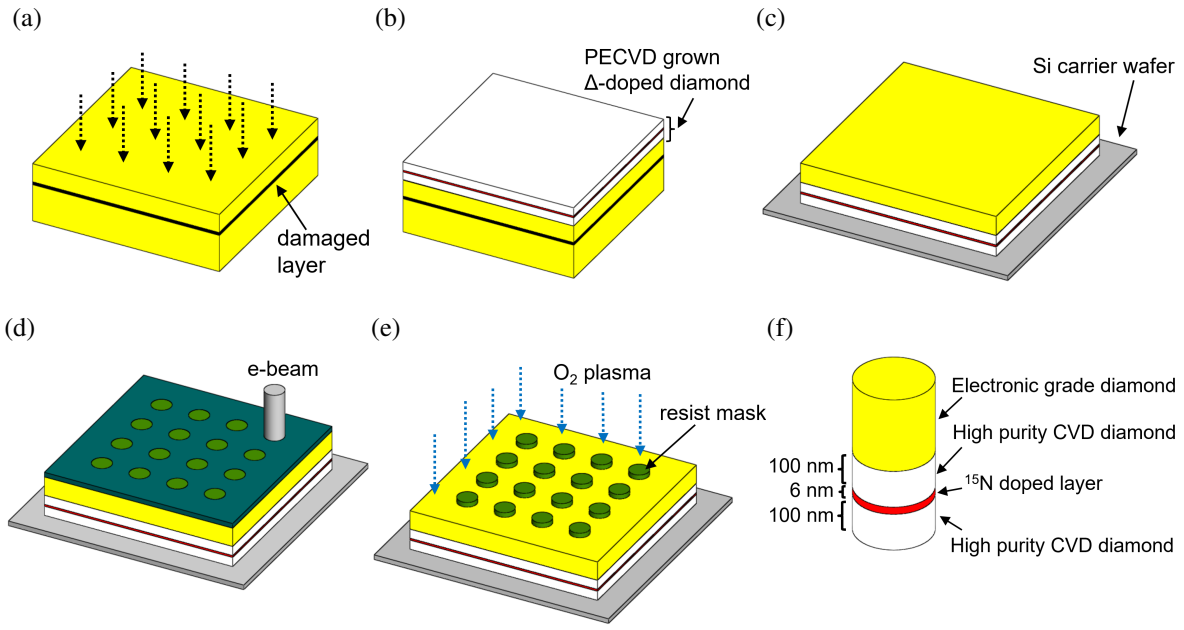

Figure 4.1: Engineered nanodiamond fabrication workflow represented for the case of a delta-doped membrane. (a) Electronic-grade bulk diamond is implanted with helium ions (He^{+}) creating a disordered layer below the diamond surface (black region in the figure). (b) Isotopically pure diamond (^{12}C) is grown on top of the substrate using plasma enhanced chemical vapor deposition (PECVD). ^{15}N doped regions (red) can be introduced in between ultra-low impurity diamond layers (white) in a controlled way. Electron irradiation and annealing are used to promote the formation of NV centers at the nitrogen locations. (c) The disordered layer is electrochemically etched to release a thin diamond membrane, which is then transferred regrown-side down on a silicon substrate and bonded using photoresist. The membrane is further thinned using an oxygen inductively coupled plasma reactive ion etch (O_2-ICP-RIE) to remove the damaged diamond layer and obtain the desired membrane thickness. (d) An etch mask is patterned on the membrane by electron beam lithography. (e) A O_2-ICP-RIE etch transfers the mask pattern to the underlying membrane to form cylindrically shaped NDs. (f) Schematic of a resulting cylindrical nanoparticle with a 6 nm NV center-rich layer sandwiched between two 100 nm low impurity layers.

spectively, which are useful for different kind of applications as mentioned in the previous chapters. While low-density, precisely positioned NV centers are ideal, for instance, for sensing small amount of spins outside the nanoparticle, high NV center's density material can be useful in applications where it is important to have a high luminescence rate, such as in some temperature sensing schemes[79].

Following the PECVD growth, the diamond is electron irradiated (2 MeV and 10^{14} cm^{-2} dose) to create vacancies in the lattice, and annealed at 850 °C for 2 h to promote the creation of NV

(a) (b)

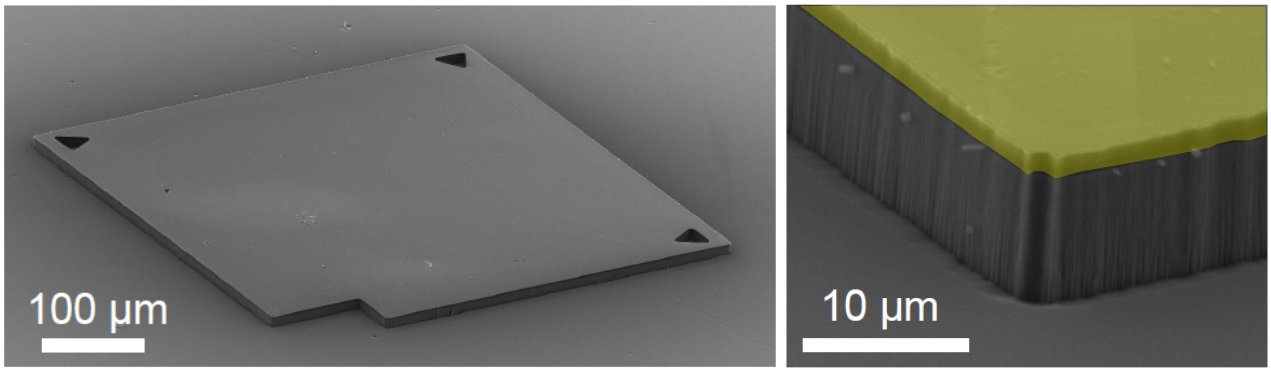

Figure 4.2: (a) SEM image of a diamond membrane bonded to silicon with PMMA resist. (b) Magnified SEM image showing the membrane (yellow, false color) on top of a silicon plateau that was formed during the membrane thinning process, which also etches the silicon substrate.

centers by mobilizing the vacancies. As the nitrogen impurities are immobile, the final NV center distribution will mirror the initial nitrogen doping profile. The sample is finally soaked in boiling acid (1:1:1 = H_2SO_4:HNO_3:$HClO_4$ at 200 °C) to oxygen terminate the surface, stabilizing the negatively charged state of the NV center[46, 60].

4.1.2 Diamond membrane fabrication

The next step of the fabrication process involves the separation of the high-quality regrown diamond material from the substrate in the form of thin membranes. In this work we use 500 by 500 µm membranes and in order to define their profile in the bulk material, we first use a photolithography step to pattern an array of 500 by 500 µm squares in a ∼200 nm thick SiO_2 mask deposited by PECVD. The mask pattern is etched into the diamond using oxygen inductively-coupled plasma reactive ion etching (O_2-ICP-RIE) until the disordered underlayer is exposed. Individual diamond membranes are then detached from the substrate using an electrochemical process aimed at selectively etching the disordered layer. To accomplish this, the sample is submerged in water and two tungsten electrode tips are use to apply a DC voltage (∼50 V) across one of the membranes[93]. The membranes released from the substrate are then collected in a water droplet and drop-casted onto a temporary substrate. Next, they are mechanically stamped to a silicon car-

rier substrate using a poly(methyl methacrylate) (PMMA) adhesion layer as described in details in appendix A (Figure 4.1(c)). The membranes are transferred with the newly grown diamond facing down and thinned using a O_2-ICP-RIE etch to remove impurities and defects that arise near the disordered layer and in the implanted material. After thinning, membranes are typically between 500 nm and 2 µm thick.

4.1.3 Diamond membrane patterning

Cylindrical particles are created from the diamond membrane by defining an etch mask using electron beam lithography and by transferring the pattern to the underlying material using a O_2-ICP-RIE etch. We start by thermally evaporating 3 nm of chromium on the diamond surface to promote the adhesion of the resist mask. We then spin-coat a negative electron lithography resist (1:1 Hydrogen silsesquioxane (HSQ):MIBK), which, when exposed, results in an amorphous silicon dioxide mask ∼200 nm thick. The sample is then exposed using a 30 keV electron beam at a dose of 650 µC/cm^2 (Figure 4.1(d)), developed with a 25 % solution of Tetramethylammonium hydroxide (TMAH) in H_2O for 70 s at room temperature, rinsed in deionized (DI) water, and dried. Next, we bake the sample at 300 °C in air for 10 min to promote uniformity in the hard mask. A chlorine/oxygen etch removes the Cr adhesion layer in the exposed areas, and finally we use a O_2-ICP-RIE etch to transfer the pattern of the mask into the diamond at ∼100 nm/min (Figure 4.1(e)). Details of the resist spinning and etching recipes are reported in appendix A.

Using this approach, we define cylindrical particles with diameters ranging from 100 nm to 600 nm (Figure 4.3(a)), and with a nearly 100 % yield (Figure 4.3(b)). The residual mask present on top of the NDs can be removed using buffered hydrofluoric (HF) acid.

4.1.4 Preparation of a nanodiamond solution

One major advantage of our fabrication process is that once the diamond membrane has been fully removed in the regions that are not covered by the mask, the cylindrical nanopillars remain loosely attached to the silicon substrate through a thin resist anchor. This allows us, for instance, to easily

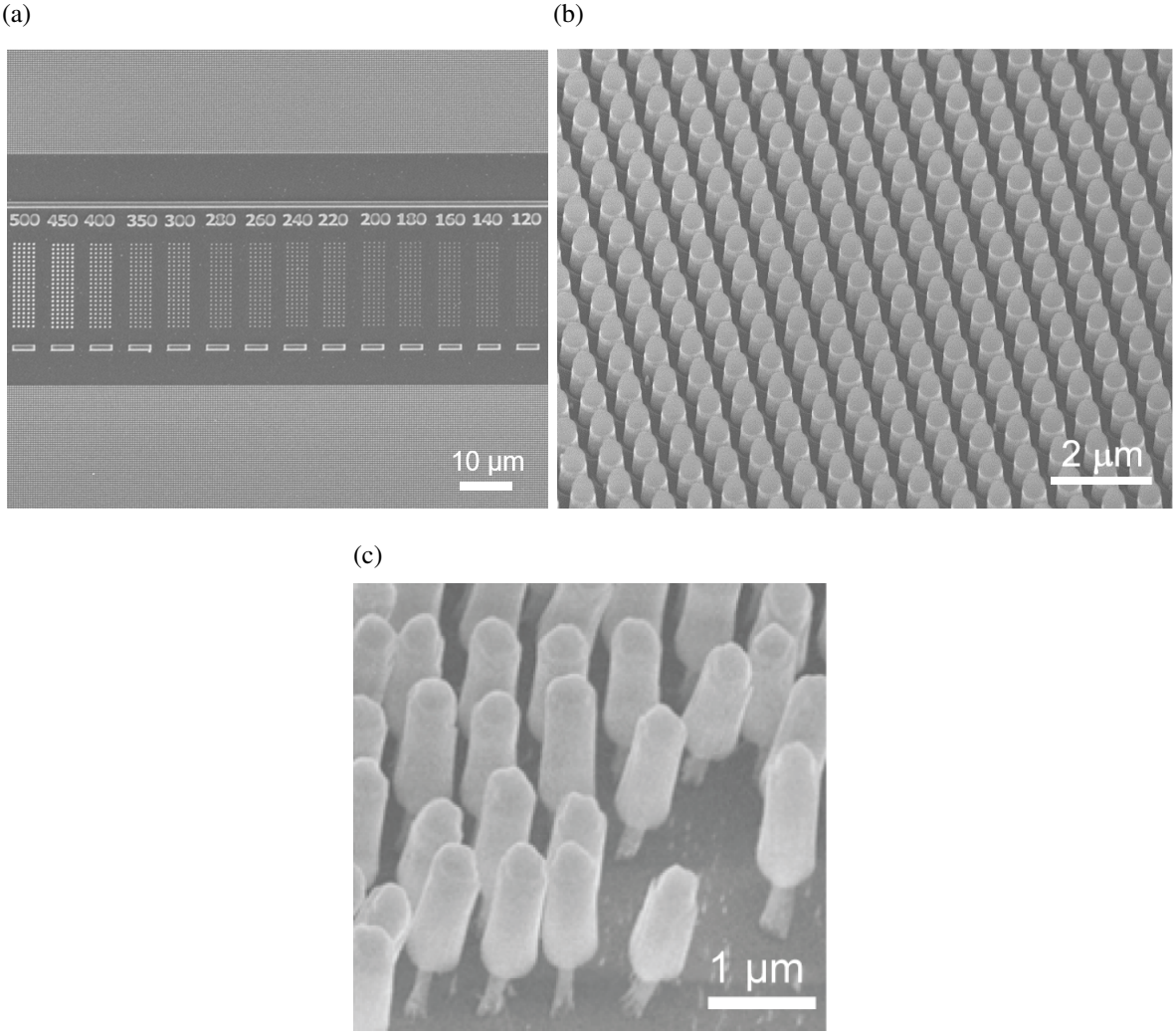

Figure 4.3: SEM images of the fabricated nanoparticles. (a) The center of the image shows arrays of NDs with diameters ranging from 120 nm to 500 nm. Particles with 100 nm and 600 nm diameters were also obtained. NDs in the upper and lower parts of the image are 300 nm in diameter and have a pitch of 500 nm. (b) The engineered nanoparticles are fabricated in near 100 % yield over hundreds of square microns. The etch mask is still visible on the top of the nanopillars. (c) NDs anchored to the underlying substrate by a photoresist pillar after the etch reaches the bottom of the membrane.

release the NDs in a solution. In the following chapter we will also discuss how this property can enable the creation of portable arrays of nanoparticles.

One approach to obtain a suspension of NDs involves soaking and sonication of the sample in acetone or deionized water to release the particles from the substrate. When acetone is used, a centrifugation process allows us to precipitate the particles and use them to create a water sus-

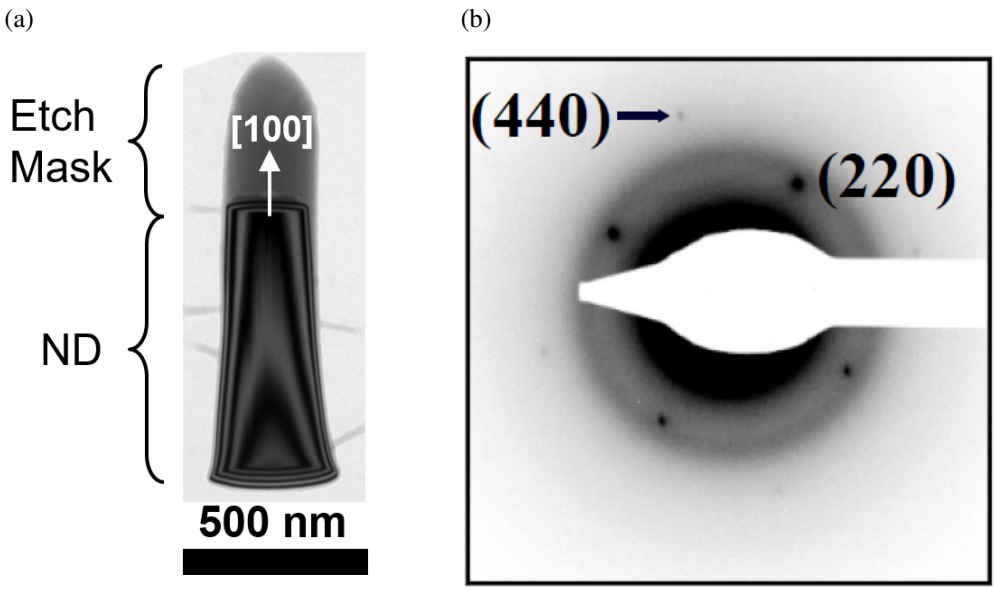

Figure 4.4: (a) Transmission electron microscope (TEM) image of an engineered diamond particle with the etch mask cap preserved. The taper of this particle is 96.7° and the [100] crystal direction (indicated with an arrow) is parallel to the main axis. The alternating dark and light regions are fringes due to the Bragg condition being modulated by the thickness of the crystalline ND. The amorphous mask does not show sign of crystallinity. (b) Selected-area electron beam diffraction pattern of the ND further confirms its single-crystal nature.

pension if necessary. Finally, we run the suspension through 2 - 5 µm pore filters to remove most of the contaminants coming from the silicon substrate. More details about the preparation of the NDs solution and an alternative approach used to obtain ultra-pure suspensions are presented in appendix A.

4.2 Analysis of the crystal properties of the nanodiamonds

We use a transmission electron microscopy (TEM) analysis to characterize the crystallinity and crystal orientation of the NDs obtained from both growth structures. The result of these measurements gives us information on the crystal quality of the PECVD grown diamond and on the effects of our fabrication process on the direction of the crystal axes relative to the particle ones. Furthermore, this information is useful for interpreting the spin measurements presented in what follows as it allows us to predict the NV centers axis orientation.

We prepare TEM samples by placing a 25 µL drop of engineered ND solution onto a commercial carbon film TEM support grid and allow the sample to dry in air. We perform imaging and collect diffraction patterns with an FEI Titan FEG TEM/STEM operated at 100 kV. Figure 4.4(a) shows a TEM image of a ND of diameter 300 nm and length 1 µm with the silicon dioxide cap retained. The alternating light and dark fringes are due to a thickness modulation of the Bragg condition. The presence of these fringes over the entire ND, in contrast with the absence of fringes in the region of the amorphous silicon dioxide cap, indicates that the particle is composed of a single crystal domain. Indeed, in a polycrystalline samples different domains would not simultaneously satisfy the Bragg condition, and therefore the fringes would appear only in a single domain at a time. We provide further evidence for the single crystal quality of the NDs by performing selected-area electron beam diffraction measurements (Figure 4.4(b)). The two set of spots positioned on two concentric circles in the diffraction pattern correspond to the (440) and (220) family of planes of the diamond lattice. If the NDs were polycrystalline, we would expect to see these sets of diffraction spots repeated at different position on the two circles. The homogeneous rings in the image are likely due to the amorphous carbon of the support film and to the amorphous mask cap. Finally, combining the information we obtained from real space and diffraction imaging, we establish that the diamond [100] crystal axis is consistently aligned with the main axis of the cylindrical particles (see Figure 4.4(a)).

4.3 Photoluminescence properties

To investigate the PL properties of the NDs we use a home-built confocal microscope apparatus[55] equipped with a 532 nm laser that we use to optically pump the NV centers. We compare the PL from an unprocessed membrane to the one from particles of different sizes to characterize the effect of the fabrication process. In Figure 4.5(a) we show an SEM image of the calibration array used in this experiment. The region on the left (*bulk*) is an area of the membrane left unprocessed to be used as a control reference signal. In Figure 4.5(b) we present a two-dimensional map of the PL signal collected rastering the pump laser over the calibration array. The image is slanted due to the

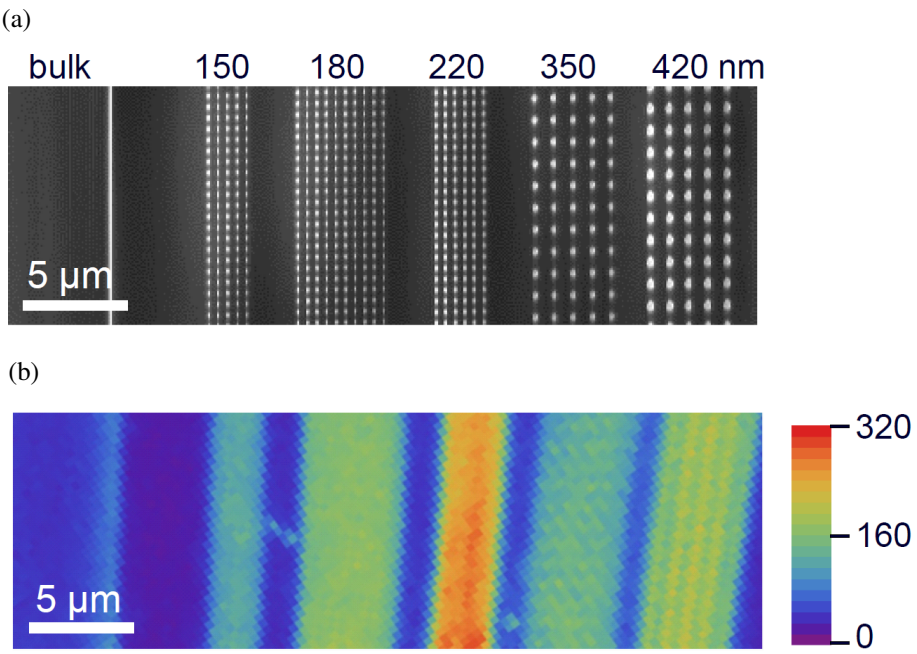

Figure 4.5: (a) SEM image and (b) scanning confocal photoluminescence image of diamond nanoparticles still attached to the silicon carrier wafer. The region labeled bulk was left unprocessed, while the diamond particles' diameter is labeled above the SEM image. The slant in the optical image is an artifact due to the high laser scan speed.

high scan speed of the laser. It is clear that, for all the diameters we studied, the particles exhibit an enhancement in the collected signal with respect to the bulk membrane, indicating an improvement in PL extraction efficiency due to a reduced total internal reflection at the diamond-air interface. At the same time, it is also evident that the enhancement is affected by the particle size, peaking at $\sim$10 times the bulk membrane signal (on average) for 220 nm diameter particles. This is due to the variations in the waveguiding efficiency for different pillar sizes[61].

In summary, by carefully engineering the geometry of the NDs we can strongly enhance the accessible PL signal, which is of great importance as NV centers in diamond nanoparticles usually have slower radiative rates than in the bulk (see Chapter 3).

In order to prove that our fabrication process is suitable to access the single defect regime, we collect photon correlation curves using a standard Hanbury-Brown and Twiss measurement scheme on NDs that were obtained from growth structure #2 material. In Figure 4.6, we show the second order correlation curve (with no background correction) for a 300 nm diameter ND incorporating

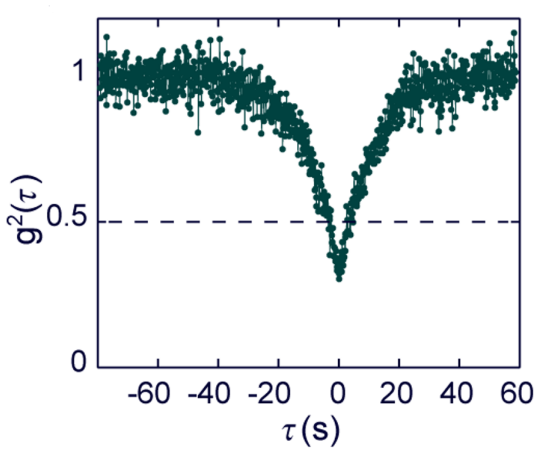

Figure 4.6: Second order photon correlation curve obtained from a nanoparticle containing a single NV center showing antibunching ($g^{(2)}(0) < 0.5$).

a single NV center, demonstrating strong photon antibunching ($g^{(2)}(0) < 0.5$). Using the PL intensity collected for a single NV as a reference and correcting for the variations in the collection efficiencies, we estimate that the NV center density varies between 0 and 10 NV centers per particle across the different particle sizes.

4.4 Spin properties

To characterize the spin properties of the NDs, we deposit a drop of suspension ($\sim$5 µL) in the proximity of a coplanar waveguide terminating in a circular antenna patterned on a silicon chip (Figure 4.7(a)). This allows us to deliver microwave signals to the NV centers. A piranha clean procedure (3:1 = [concentrated sulfuric acid: 30% hydrogen peroxide water solution]) is used to remove any organic residue left behind by the solution. This allows us to use the PL signal to quickly individuate the particles by removing any spurious source of PL.

We now discuss the procedure that we use to identify the engineered NV centers and investigate their coherence properties.

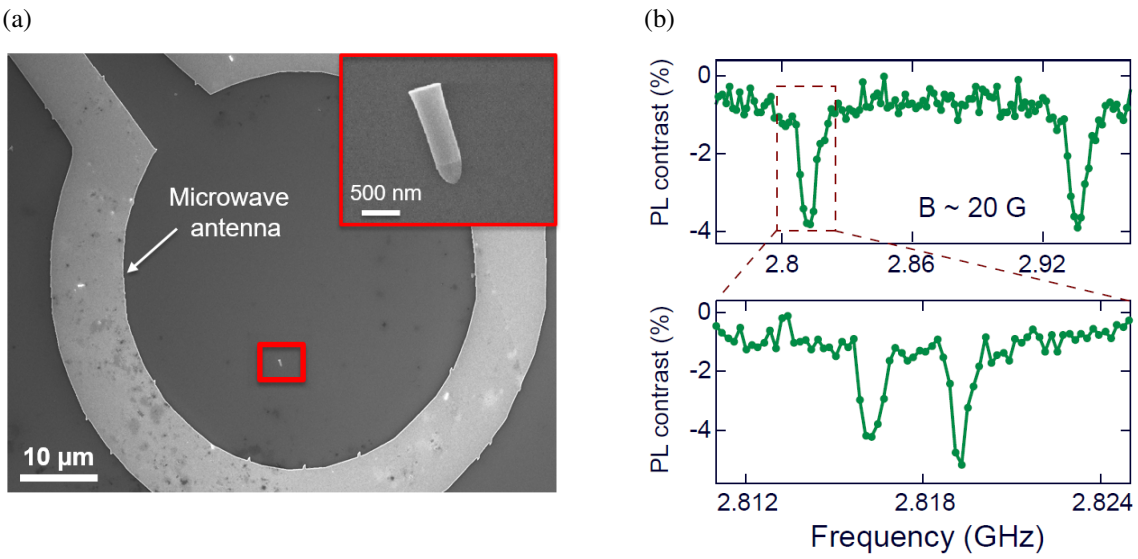

Figure 4.7: (a) SEM image of a circular microwave antenna terminating a coplanar waveguide patterned on a silicon substrate. Diamond nanoparticles (inset and red square) are drop-casted on the substrate from solution. (b) CW-ODMR (top) and high-resolution ODMR (bottom) collected on a nanoparticle containing a single NV center. The spectrum at the bottom shows the hyperfine structure associated with a ^{15}NV center.

4.4.1 Identification of the engineered NV centers

To begin our analysis of the spin properties of the NV centers contained in the engineered nanoparticles, we need to distinguish between the NV centers originating from the PECVD growth process and those native of the bulk diamond. This is necessary since we usually do not fully remove the substrate material. This distinction can be achieved by detecting the isotopic signature of the ^{15}N nuclei in the NV centers' ODMR spectra[122]. Indeed, the non-zero nuclear spin of both isotopes of the nitrogen nucleus results in the presence of a hyperfine interaction with the electron spin associated with the NV center, which introduces an additional term to the hamiltonian in eq. (2.1)

$$\frac{H_{hyp}}{\hbar} = \mathbf{S} \cdot \mathbf{A} \cdot \mathbf{I} \tag{4.1}$$

Here, $\mathbf{A}$ is the hyperfine tensor, and $\mathbf{I}$ is the spin operator for the nitrogen nucleus. Because the ^{15}N isotope ($\sim$0.362 % natural abundance) and the ^{14}N isotope have different nuclear spins (1/2 and 1 respectively), the hyperfine interaction results in a distinguishable 2 peak (^{15}N) or 3 peak

(^{14}N) structure for each ODMR peak.

To probe this hyperfine structure, we use a high frequency resolution ODMR technique[38]. In this technique instead of using continuous optical and microwave excitation, laser pulses are used to initialize and readout the NV centers, and microwave pulses that guarantee π rotation in resonant conditions are applied to control the spin. As an example, in Figure 4.7(b) we report the continuous wave ODMR (CW-ODMR) (top) and the high resolution ODMR scan of one of the CW-ODMR resonances (bottom) measured on a particle containing a single NV center (a magnetic field of $\sim$20 G is applied along the NV center axis).

All the NV centers studied in this work show a fine structure consistent with ^{15}N hyperfine interaction, confirming that they are associated with nitrogen impurities intentionally introduced during the growth process. We now proceed to the analysis of the spin coherence properties of these NV centers.

4.4.2 Spin coherence

The spin coherence is inferred from the decay time of coherence curves obtained with standard Hahn echo measurements ($T_{2,Hahn}$). The pulse sequence used in these measurements was described in details in 2.3.2, but we briefly summarize it again here to highlight the specifics of the implementation that we use (differential measurement). A sketch of the sequence is shown in Figure 4.8(a) (the Hahn echo corresponds to the case n = 1). First, a 1.5 µs pulse of a 532 nm wavelength laser is used to initialize the NV center into its m_s = 0 state. A π/2 microwave pulse resonant with one of the hyperfine resolved spin transitions is then used to create the superposition of the m_s = 0 and, for instance, the m_s = -1 (the degeneracy with the m_s = +1 state is lifted with the application of an external magnetic field). The system is then free to evolve for a time τ/2 before the π microwave pulse is applied. Lastly, the system evolves freely for τ/2 before a final microwave pulse converts the phase accumulated between the two states into a population difference. A second 1.5 µs green laser pulse is then applied and the resulting photoluminesce is collected using an avalanche photodetector (APD). Only the PL generated during the first 400 ns

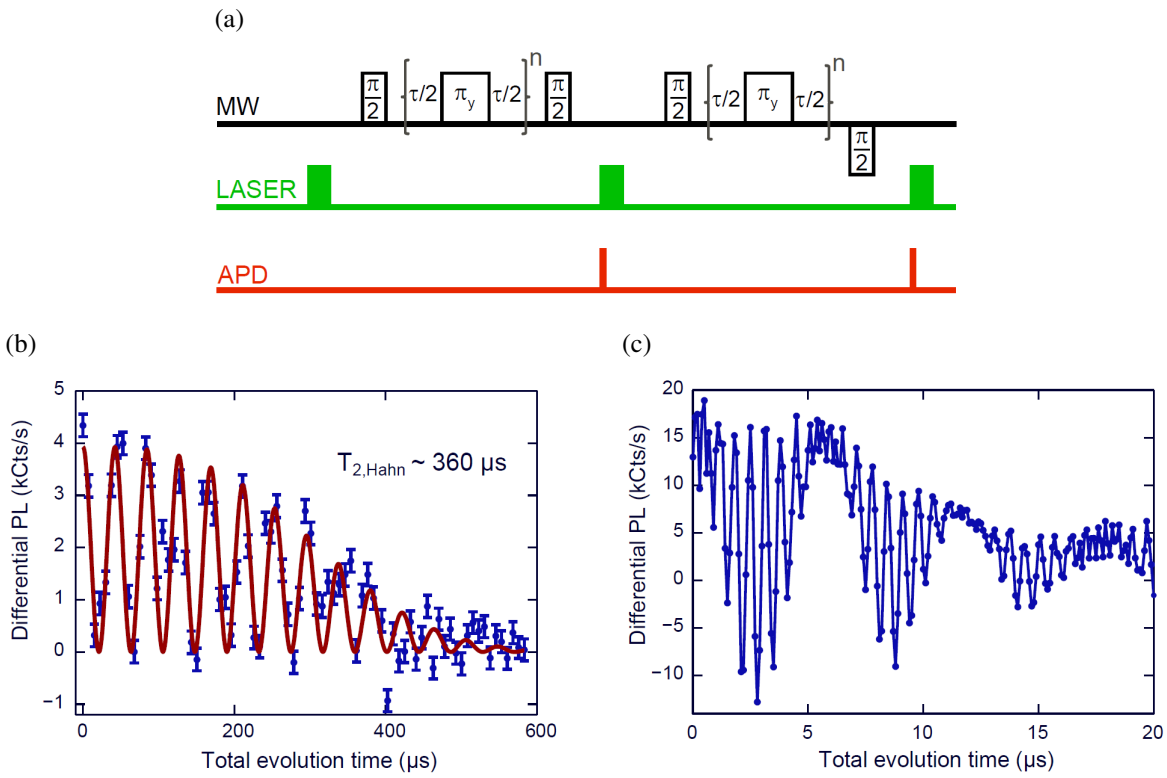

Figure 4.8: (a) Schematics of the pulse sequences used to characterize the spin coherence properties of the NV centers. For n = 1 the sequence reduces to a standard Hahn-echo measurement. For the CPMG measurements we use n = 5. (b) Hahn-echo measurement obtained on a particle incorporating a single NV center. The data is fit to equation 4.2 which provides an estimate for $T_{2,Hahn}$ = 357 ± 38 μs. (c) First 20 μs of the Hahn-echo trace revealing the fast dynamics associated with the interaction of the electronic spin of the NV center with the defect's ^{15}N nuclear spin.

is used to infer information on the spin state so as to maximize the signal to noise ratio[141]. The remaining time of the laser pulse is used to prepare the system in m_s = 0 again. The second half of the sequence differs by the sign of the last π/2 pulse. In this situation at τ = 0 the final state would be m_s = -1. The PL collected in the two halves of the sequence is then subtracted to obtain a differential signal that is not affected by oscillations in the PL or by PL that is not related to the NV centers that we are targeting (in the case of ensembles of NV centers with multiple orientations).

We first focus on the analysis of the NDs obtained with the delta-doped material (growth structure #2). To start, we inspect the coherence time of the NV centers in an unprocessed delta-doped membrane to ensure that the membrane fabrication step leaves the NV centers' properties intact. Two separate measurements give us $T_{2,Hahn}$ ~305 μs and ~750 μs respectively, in line with

what is expected for NV centers ∼100 nm below the surface of isotopically pure, delta-doped bulk diamond[114]. We then measured $T_{2,Hahn}$ for a series of particles. The selected NDs have diameters of 300 nm and 500 nm, and contain single NV centers. The average $T_{2,Hahn}$ decreases to ∼100 µs, but a significant portion of the measured values (3 out of 10) are in excess of 200 µs. The measurement collected on the NV center with longest coherence time is shown in Figure 4.8(b). The Hahn-echo trace shows periodic revivals caused by the interaction between the NV center electron spin and the defect's own ^{15}N nuclear spin[99], as well as additional oscillations that are likely associated to the presence of other substitutional ^{15}N atoms in the proximity of the defect.

To further analyze the effect of these interactions and understand their origin, we collect high temporal resolution measurements of the first 20 µs of the Hahn-echo trace (Figure 4.8(c)). This trace shows two revival dynamics. The fastest oscillation (∼3.05 MHz) corresponds to the well-known[114, 99] hyperfine interaction between the NV center's electronic spin and the defect's ^{15}N nuclear spin. The second fastest oscillation is associated with the effect of the Larmor precession of the defect's ^{15}N nuclear spin when the NV center is in the m_s = -1 state, enhanced by the electronic spin through the non-secular term of the hyperfine interaction[17]. From this Larmor frequency (∼335 kHz) we estimate that the component of the magnetic field perpendicular to the NV center axis is ∼59 G. From CW-ODMR measurements we estimate a parallel component of the magnetic field of ∼18 G, resulting in a total magnetic field of ∼62 G, compatible with what obtained from a separate measurement collected using a gaussmeter (note that the external magnetic field is different than for the measurement in Figure 4.8(b)).

As a result of the limitations in the achievable time resolution for long evolution times, when we collect the full Hahn-echo curve we sample the signal only at the antinodes of the second fastest oscillation in order to obtain clearer data. Here two slower oscillation dynamics are visible, which have their first revivals at ∼45 µs and ∼105 µs respectively. As mentioned earlier, these two oscillations are likely due to the interaction with a spin bath composed of the nuclear and electron spins of other substitutional ^{15}N situated in the region surrounding the NV center. We fit this data to the function

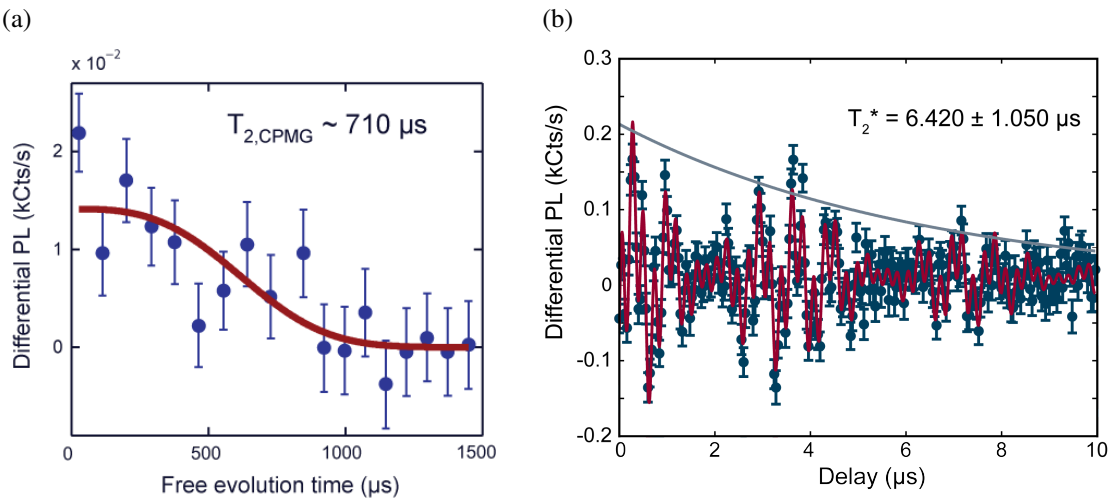

Figure 4.9: (a) CPMG measurement obtained on the same particle of Figure 4.8 using a sequence of five π-pulses. A fit of the data analogous to the one used for the Hahn-echo curves gives us $T_{2,CPMG}$ = 708 $\pm$ 215 µs. (b) A Ramsey trace revealing the dynamics associated with the ^{15}N nuclear spins. We fit the data to equation 4.3 (red line), resulting in T_2^* = 6.42 $\pm$ 1.05 µs. The grey line is the T_2^* decay envelope to guide the eye.

$$ae^{-[\tau/T_{2,Hahn}]^3}\cos(2\pi\nu\tau), \tag{4.2}$$

from which we obtain ν = 11.825 $\pm$ 0.08 kHz and $T_{2,Hahn}$ = 357 $\pm$ 38 µs. All uncertainties reported here and in the following are quoted at 95% confidence. We note that in the fit we disregard the slowest oscillation to simplify the estimate for $T_{2,Hahn}$. Imprecisions in the fit at long evolution times are due to imperfections in the measurement sampling period.

The broad distribution that we obtain for the values of $T_{2,Hahn}$ is likely associated with variations in the position of the NV centers with respect to the NDs' sidewalls, because the proximity to the diamond surface deteriorates the NV center coherence, as discussed in section 2.4. Nevertheless, we can conclude that with our fabrication process we can reliably obtain nanoparticles containing NV centers with $T_{2,Hahn}$ times, which are, on average, an order of magnitude longer than the highest values obtained in commercial nanoparticles.

In order to estimate the full potential of the engineered NDs, we also collect coherence measurements using a CPMG sequence composed of five π-pulses (Figure 4.8(a) with n = 5). We note that, as a result of adopting a single-axis decoupling scheme, the number of π-pulses that we can

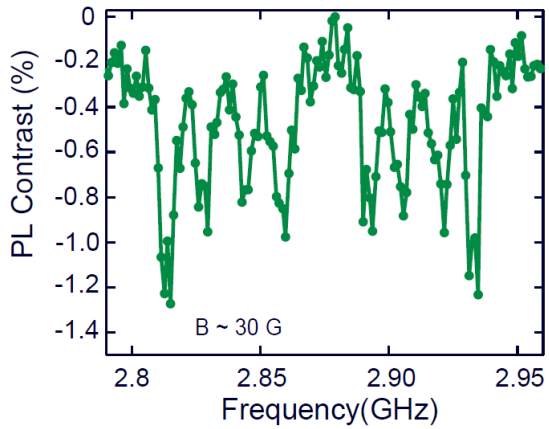

Figure 4.10: CW-ODMR spectra of uniformly doped diamond particles in the presence of an external applied magnetic field of 30 G randomly oriented with respect to the ND [100] crystal direction.

use in the sequence is limited by the effects of pulse errors[144]. Nonetheless, using this technique we are able to extend the coherence time up to $T_{2,CPMG}$ = 708 $\pm$ 215 µs (Figure 4.9(a)). The CPMG data shows only partial evidence of the ^{15}N related oscillations due to the sampling rate of the full trace, and these incomplete oscillations complicate the fit of the data, resulting in the large uncertainty we report. We note that replacing ^{15}N doping with ^{14}N doping would eliminate the oscillations in the signal and simplify the data analysis. This is due to ^{14}N's large quadrupolar splitting, which suppresses transitions between nuclear spin levels and prevents the spin precession, thereby introducing a simple static effect on the NV center's spin[17].

Finally, we also measured the inhomogeneous coherence time T_2^* for single NV centers as this parameter determines the achievable DC sensitivity. We used a standard Ramsey sequence (described in 2.3.2) and measured T_2^* times up to 6.42 $\pm$ 1.05 µs (see Figure 4.9(b)). The signal shows beating consistent with the oscillations associated with the ^{15}N spins and it was fit using the function

$$e^{-[\tau/T_2^*]}\big(A\cos(2\pi(\omega_1 \pm a)t + \phi_1) + B\cos(2\pi(\omega_2 \pm a)t + \phi_2)\big). \tag{4.3}$$

For comparison, we also analyze the properties of NDs obtained from a uniformly doped membrane (growth structure #1). CW-ODMR spectra show four pairs of peaks for a randomly oriented

external magnetic field (see Figure 4.10), consistent with the expected distribution of NV centers in all four crystal orientations for a single-crystal diamond sample. The $T_{2,Hahn}$ times are typically shorter ($< 5\,\mu s$) both for the bulk membranes and for the particles, likely due to the decoherence effects of ^{13}C atoms and of structural defects present in the rapidly grown material.

4.5 Magnetic field sensing in solution

To demonstrate the suitability of our engineered NDs as contactless scanning nanoprobes, we employ them to perform high sensitivity measurements in aqueous solutions, in combination with an infrared optical tweezers apparatus[62]. As a proof-of-concept, we work with high PL particles obtained from the uniformly doped material (growth structure #1) in order to obtain a larger signal-to-noise ratio. Thanks to the flexibility of our fabrication process, we can use $\sim$500 nm diameter, $\sim$2 µm long NDs, which occupy most of the trapping volume, strongly reducing the chances of multiple trapping and therefore improving the nanodiamond stability. Additionally, we use microfluidic circuits developed using standard polydimethylsiloxane (PDMS) fabrication processes[101] to control the nanodiamond solution. Once integrated with the optical setup, these systems allow us to efficiently transport a suspension of NDs into the trap region and, when a single particle is trapped, to flow deionized water to flush out excess particles and obtain a well-controlled surrounding environment. The design of one of the microfluidic circuits used in the measurements that follow is shown in Figure 4.11(a). The fabrication of the microfluidic circuits is discussed in appendix B. In Figure 4.11(b) a schematic of the setup at the sample location, and an optical image of a microfluidic channel with a trapped nanoparticle are shown.

To demonstrate the improvements in the trapping stability that can be obtained in our system, in Figure 4.12(a) we first compare the PL collected from commercial NDs (ND-NV-100nm, Adámas Nanotechnology) optically trapped in a drop of suspension deposited on a bare glass slide (top), with the one measured from NDs trapped inside a microfluidic circuit (bottom). Both traces are plotted using the same vertical scale to highlight the improvement in the signal stability. Specifically, the standard deviations of the PL signal in the droplet and in the microfluidic channel are

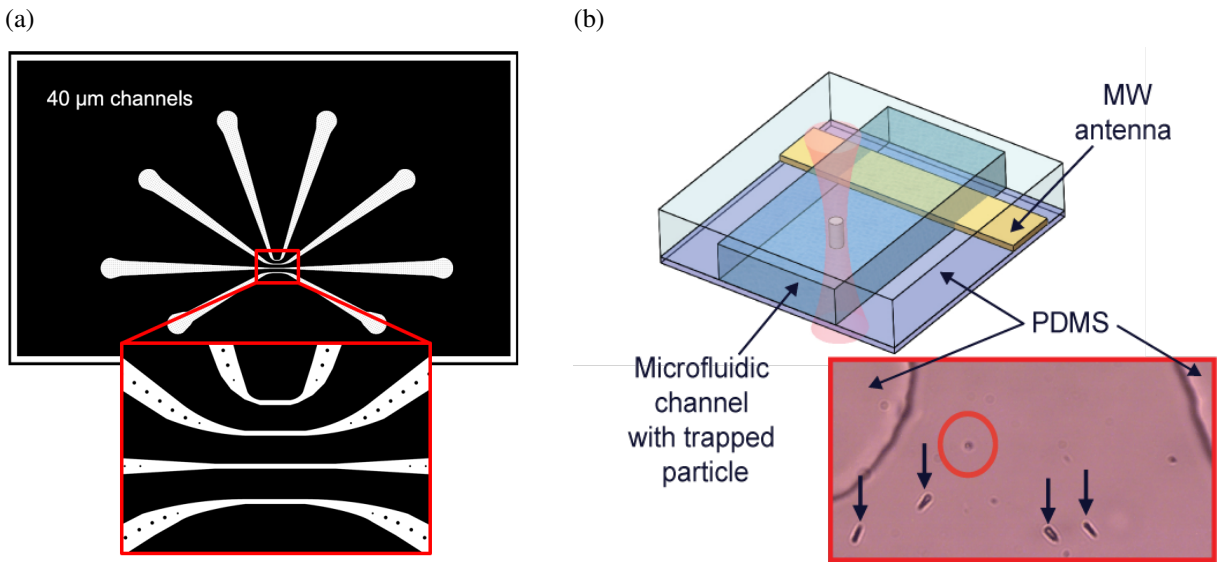

Figure 4.11: (a) Design of one of the microfluidics circuits used in this work. Multiple inputs and outputs are created as a redundancy measure. The black dots identify pillars that provide support for the microfluidic channels. See appendix B for more details. (b) Sketch of the optical tweezers/microfluidic apparatus at the optical trap location. The infrared trapping laser and the green probe laser are focused via a microscope objective (not shown) inside a microfluidic channel created in a PDMS layer bonded on top of a glass slide. A coplanar waveguide is patterned on the glass slide for microwave signal delivery. Inset: optical image of the interior of the microfluidic channel filled with a solution of engineered NDs. Some nanoparticles stuck to the bottom of the channel are indicated by arrows. One particle is trapped along its axis and levitated (red circle).

respectively $\sim$238 kCts/s and $\sim$9 kCts/s.

As we have seen in the previous chapter, another important limitation of commercial particles is associated with their random shape, which prevents a priori determination of the NV center orientations and results in uncontrolled rotational motion in aqueous environments. Random rotational dynamics complicate the interpretation of sensing measurements[62] and ultimately limit the use of dynamical decoupling techniques. In the top panel of Figure 4.12(b), we show a CW-ODMR spectrum for an ensemble of commercial NDs trapped inside a microfluidic channel in the presence of an external constant and uniform magnetic field (B $\sim$10 G) aligned along the trap axis (traveling axis of the trapping laser). We find that, even in a well-controlled environment, the effect of the rotation dynamics is evident and results in a spectrum with two broad peaks having a full-width-half-max (FWHM) of $\sim$30 MHz. In contrast, by carefully designing the geometry of our engineered particles, we introduce a preferential direction along which the NDs' main axis

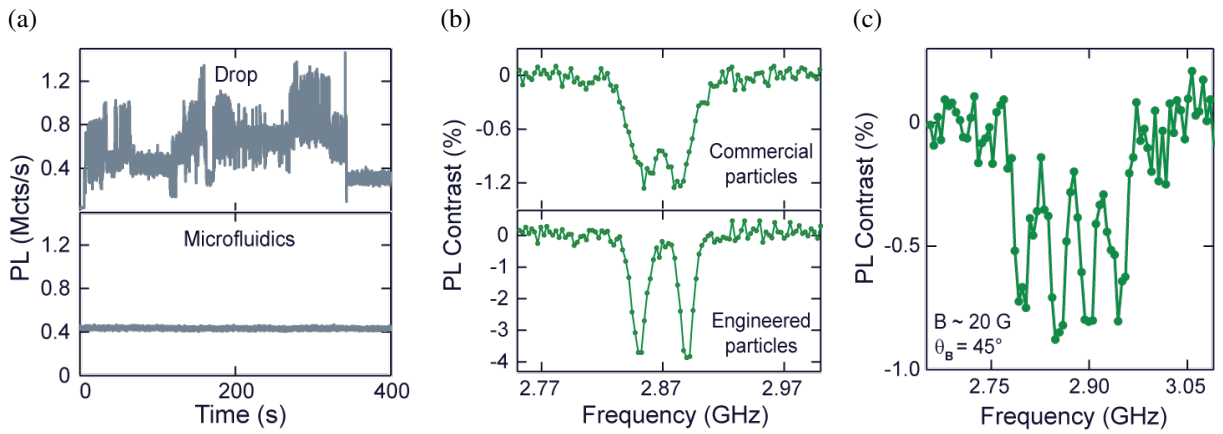

Figure 4.12: (a,top) Time trace of the photoluminescence signal collected from commercial NDs trapped in a drop of solution deposited on a bare glass slide and (a,bottom) flowed inside a microfluidic channel. (b,top) CW-ODMR spectra of commercial NDs and (b,bottom) of an engineered ND optically trapped in a microfluidic circuit. An external magnetic field ($\sim$10 G) is applied along the axis of the trap (54.7° with respect to the NV centers orientations). The signal is averaged for 0.6 s at each frequency point. (c) CW-ODMR spectra of an optically trapped engineered ND in the presence of a magnetic field ($\sim$20 G) applied at $\sim$45° with respect to the trap axis. The signal was averaged for 2 s at each frequency point.

(parallel to the [100] crystal lattice) tend to align within the trap[16, 5]. In our experiment, this preferential axis is the same as the trap axis. In the inset of Figure 4.11(b) we show a picture of the interior of a microfluidic circuit around the optical trap region. The particles indicated with arrows are stuck to the bottom of the microfluidic channel. In the center, we highlight a particle that is levitated with the optical tweezers' infrared laser and appears upright, with its main axis along the optical trap axis. In the lower panel of Figure 4.12(b), we show the CW-ODMR spectrum collected in the presence of a magnetic field (B $\sim$10 G) applied along the axis of the trap. Two well-separated peaks are visible, as expected for a cylindrical particle with [100] axis aligned along the magnetic field, as the four possible NV center orientations are degenerate with respect to the magnetic field direction. The FWHM of the peaks is $\sim$10 MHz, similar to what has been previously obtained with CW-ODMR measurements both of ensembles of NV centers in bulk diamond[1] and of single NV centers in NDs integrated with an AFM tip[125]. This result further suggests that the particle is indeed trapped along the crystal axis and that this axis is not appreciably precessing during the 400 s measurement.

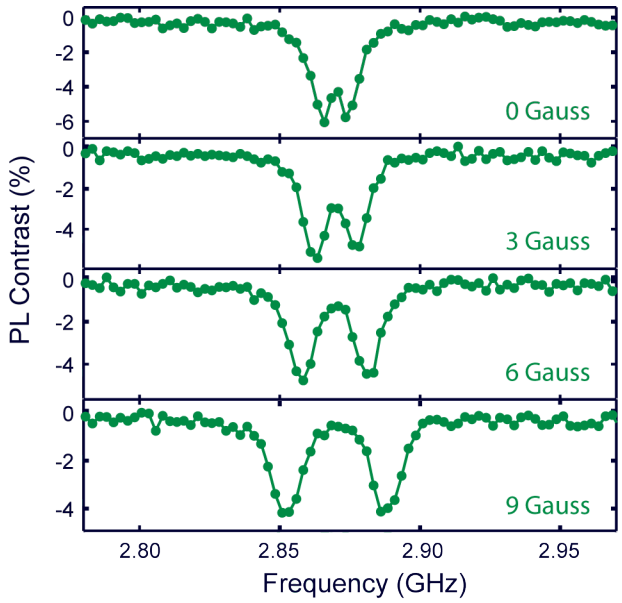

Figure 4.13: Series of CW-ODMR spectra collected on an engineered diamond nanoparticle trapped in a microfluidic channel in the presence of different magnetic field applied along the trap axis.

To gain further insights in the trapped particle dynamics, we collect CW-ODMR spectra with a magnetic field tilted with respect to the trap axis. In these conditions, we expect to see anywhere between two and four distinct peak pairs in the spectrum if the particle is not revolving around its main axis. In Figure 4.12(c), we show the result obtained with a magnetic field of $\sim$20 G applied at 45° from the trap axis, where four distinct peaks are visible. Their FWHM ($\sim$25 MHz) suggest that each peak is actually a convolution of two peaks. Nevertheless, the ability to resolve four distinct resonances in the CW-ODMR spectrum structure confirms that the trapped particle does not noticeably revolve around its main axis during the course of the measurement (800 s). We emphasize that we were able to trap particles for up to 30 hours before purposely releasing them, which serves as another indication of the good stability of the system.

The stability demonstrated here is an important advancement towards using optically trapped diamond particles as magnetic field and temperature sensors. To estimate the accessible experimental DC magnetic field sensitivity we collect a series of CW-ODMR spectra in the presence of an external magnetic field. In these measurements the field is parallel to the trap axis and varies from 0 to 10 G in steps of 1 G (in Figure 4.13 we report a subset of the collected spectra). To con-

firm that the particle is being levitated at all time, after each measurement we move the position of the trapping laser and confirm the stability of the PL signal. Indicating the minimum detectable variation in the magnetic field with δB_{min}, we calculate the optimal experimental sensitivity using

$$\eta_B = \delta B_{min}\sqrt{t} = \frac{\sigma_{c,max_\omega}\sqrt{t}}{\max_\omega\left|\frac{\Delta C}{\Delta B}\right|} \tag{4.4}$$

where t is the measurement time for each frequency data point, $\max_\omega\left|\frac{\Delta C}{\Delta B}\right|$ is the variation of the CW-ODMR contrast for a change ΔB in magnetic field at the frequency that results in the optimal sensitivity, and σ_{c,max_ω} is the corresponding error on the contrast. This calculation gives us an optimal experimental sensitivity of $\sim$9 μT/Hz$^{1/2}$, comparable with the best values obtained in bulk diamond. We note that this sensitivity could be further enhanced by employing pulsed techniques to avoid power broadening in the CW-ODMR spectrum and by using isotopically pure material for the growth. Indeed in nanoparticles obtained from growth structure #1 we observe values of T_2^* of the order of few hundreds of nanoseconds, at least an order of magnitude lower than what was measured in the isotopically pure material. Additionally, the use of a pulsed optical trap would reduce the detrimental effect of the infrared laser on the NV centers' PL[81], increasing the signal-to-noise ratio of the measurements.

In conclusion, we developed a nanofabrication technique that is suitable for engineering single-crystal cylindrical diamond nanoparticles with reproducible shape, size, and crystal orientation. Crucially, the NDs can efficiently be released from the substrate and dispersed in solution. Using high quality, delta-doped diamond membranes, we are able to obtain NDs containing single NV centers with long coherence times ($T_{2,CPMG}$ up to 710 μs). These coherences are more than an order of magnitude longer than what is achievable with regularly available nanoparticles, and approach the bulk coherences, making these NDs ideal as high sensitivity, high spatial resolution probes. A possible approach to improve the potential of these NDs would be to combine our fabrication process with a technique to obtain lateral positioning of the NV centers relative to the sidewalls[115]. This would enable the creation of particles incorporating NV centers with long,

highly predictable spin coherence times and well-known distance from the diamond surface, which are critical parameters for the interpretation of the magnetic signature of external spins.

We also show that the precise control of the particles shape and geometry can strongly enhance the potential of NDs for sensing applications in fluids in combination with optical trapping techniques. In particular, when the solution of the engineered NDs is introduced within a microfluidic circuit we obtain stable trapping and can perform CW-ODMR measurements for more than 30 hours, demonstrating a magnetic field sensitivity comparable to the typical values for immobilized diamond structures[53]. Furthermore, these results suggest that our optically trapped NDs are sufficiently stable to be used in combination with dynamical decoupling techniques and could lead to the realization of low-thermal-mass, high sensitivity probes for fluctuating magnetic field and temperatures[102, 58] in fluid. For instance, these NDs could be used to determine important parameters in microfluidic environments such as the temperature of chemical reactions, or they could be manipulated inside a biological environment to explore the details of these systems at the nanoscale.

In addition to these applications in solution, NDs provide a platform to investigate the properties of magnetic materials with nanoscale spatial resolution[125] and to study the details of heat flow patterns in electronics and spintronics devices to advance the understanding of thermal phenomena like the Seebeck and spin Seebeck effects. A commonly used approach in these studies involves the integration of the NDs with an atomic force microscope probe to perform high resolution scanning measurements. While remarkable advancements have been obtained using these techniques[146], they have the disadvantage of being non-portable and hard to adapt to wide ranges of samples due to their complexity. Additionally, the commonly used silicon scanning cantilevers introduce a source of heat propagation that can strongly influence temperature measurements. In the next chapter we will introduce a technique to develop portable and flexible arrays of nanodiamonds that can easily be positioned on target samples of arbitrary shape. The nanoparticles are in this case embedded within a low-thermal conduction matrix, which strongly reduces the presence of spurious heat losses in the system.

CHAPTER 5

PORTABLE AND FLEXIBLE ARRAYS OF NANODIAMONDS

The goal of this work is to integrate arrays of NDs into a reusable platform that can be used to investigate the thermal and magnetic properties of a wide range of systems. To minimize the requirements on the sample to be measured the nanodiamonds need to be encased within a matrix that satisfies a set of requirements:

- Is transparent to visible light and gigahertz range radiation;
- Guarantees the presence of a good contact between the nanodiamonds and the sample;
- Has low thermal conductivity to avoid introducing spurious thermal dissipation channels;
- Is non-magnetic;
- Can be re-used multiple times and it is easy to manufacture to ensure the scalability of the fabrication process.

The technique that we develop combines the adaptability of a chemical pattern directed assembly technique, which allows to precisely locate the NDs, and a transfer printing technique to embed the nanoparticles into a layer of polydimethylsiloxane (PDMS), which is a transparent, portable, and flexible material that satisfies the aforementioned requirements. In the following, we present the details of the fabrication workflow (Figure 5.1) and characterize the properties of the resulting arrays of NDs. The use of commercially available nanoparticles makes this technique particularly scalable and useful for large areas applications but we will also briefly discuss how the process can be adapted to engineered nanodiamonds with better coherence and crystal properties.

5.1 Fabrication of ordered nanodiamond arrays on silicon

The nanodiamond arrays are first patterned on a silicon substrate (Si <100>, N/Phos, WRS Materials) using a chemical pattern directed assembly technique similar to that described previously

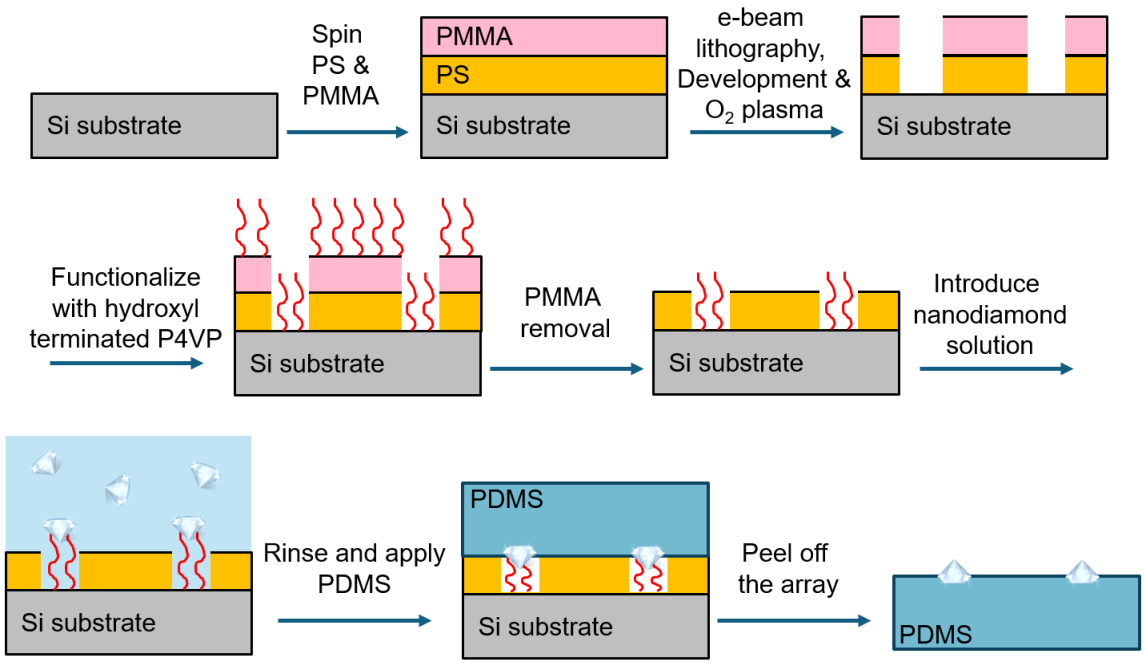

Figure 5.1: Fabrication process for the realization of arrays of nanodiamonds embedded within a transparent, flexible and portable matrix. First, crosslinked PS and PMMA resist are applied to a silicon substrate. Electron beam lithography, followed by resist development and a plasma ashing step are used to create the desired patterns within the PS layer. The sample is then functionalized with P4VP-OH, before removing the residual resist. Nanodiamonds from a drop casted solution bind preferentially at the remaining functionalized region and can finally be transfered into a PDMS layer.

in other works[88, 164]. To fabricate the ND arrays, the silicon substrate is first spin coated with 0.5 wt% cross-linkable polystyrene (PS) in toluene and annealed at 190 °C under vacuum for 24 hours to drive the crosslinking reaction. The PS is synthesized as described in [59] and contains 4 % glycidyl methacrylate as a crosslinking agent. Spin-coating and curing of poly(methyl methacrylate) (PMMA950, 4 wt% in chlorobenzene, MicroChem Inc.) resist above the PS, is followed by electron beam lithography to create the desired patterns. After the resist development with a mixture of 4-methyl-2-pentanone and 2-propanol (1:3 in volumetric ratio), we use an oxygen plasma ashing process (20 sccm O_2, 20 W, 30 s) to remove the residual resist and the crosslinked PS (XPS) in the unprotected regions. The exposed silicon patterns are functionalized with Hydroxyl-terminated poly(4-vinylpyridine) (P4VP-OH, Polymer Source, Inc.) by spin coating from a 4 wt% solution in N,N-dimethylformamide (DMF) and annealing at 210 °C for 5 min in

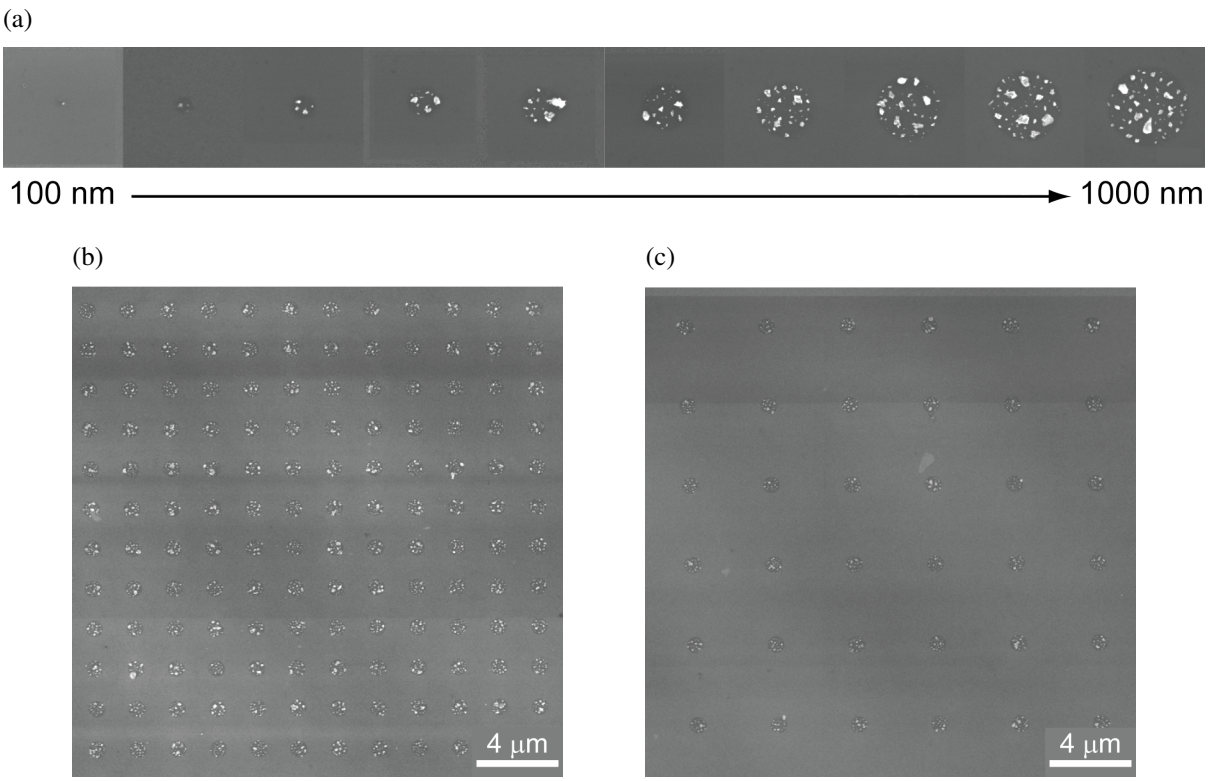

Figure 5.2: (a) SEM images of a series polymer functionalized areas on a silicon substrate, coated with diamond nanoparticles. The diameter of the patterned circles varies from 100 nm to 1000 nm in steps of 100 nm. (b,c) SEM images of two arrays of patterned circles with spacing between the circles of 2 and 4 μm respectively.

a nitrogen atmosphere. The remaining resist and excess P4VP-OH are then removed by sonication in 1-methyl-2-pyrrolidinone (NMP) (3 min, 2 cycles) and chlorobenzene (3 min, 1 cycle). A 100 μL drop of ND suspension (Adamas Technology, NV-ND-100nm) is deposited on the substrate, which is placed on an elevated post inside a sealed glass jar. The jar also contains 1 mL of water at the bottom to maintain the water vapor pressure constant and prevent the ND solution from evaporating. As the nanoparticles have a negative zeta potential ($\zeta = -35$ mV in deionized (DI) water), they are electrostatically attracted to the P4VP-OH polymers (weakly positively charged in water due to protonation) and they bind at their sites. After 40 min, the substrate is rinsed thoroughly with DI water and blow-dried with nitrogen. The PS provides minimal adhesion of the NDs to the substrate resulting in a good selectivity of the regions patterned with P4VP-OH, as it is clear from the following SEM characterization of the arrays.

5.2 Characterization of patterned arrays on silicon

In order to characterize our fabrication process, we pattern square arrays of circles with different diameters and spacing to investigate the effect of these parameters on the ND coverage yield and on the number of nanoparticles per area of patterned substrate. In Figure 5.2(a) we show a series of SEM images from patterned circles with diameters ranging from 100 nm to 1000 nm, which, as expected, reveal an increase in the number of nanoparticles per spot with the spot size. Analyzing tens of patterned spots, we obtain a more quantitative description (Figure 5.3, purple data points) and show that the number of bound nanoparticles increases linearly with the surface area of the patterned region (Figure 5.3(a)). No significant variation in the number of particles is observed when the pitch of the patterned arrays is changed from 2 µm to 10 µm (Figures 5.2(b) and 5.2(c)). Interestingly, we prove that by using 100 nm diameter spots we can obtain arrays with mostly one ND per spot (Figure 5.3(b)). This results is of great interest in applications where having multiple nanoparticles with different orientations affects the interpretation of the data or the contrast in the spin measurements. We note that this patterning technique could be used to create permanent arrays of nanosensors on any sample compatible with this fabrication process.

Figure 5.3(b) also highlights the presence of a greater variability in the number of nanoparticles per spot for larger spot sizes, which we associate to the wide distribution of the nanoparticle size ($\sim$50 nm to 300 nm). While a 100 nm patterned circle tends to be mostly covered by a single ND, independently of its size, the maximum coverage for larger circles can be reached with different numbers of nanoparticles. This variability stops to increase once the patterned circle size is substantially larger than the biggest particles ($\geq$ 700 nm) and could be reduced using solution of nanodiamonds with a narrower size distribution.

5.3 Transfer of the arrays in a silicone matrix

As we have discussed, for most applications we want to transfer the ND arrays patterned onto the silicon substrate in a PDMS matrix. We begin by mixing together PDMS base and curing agent

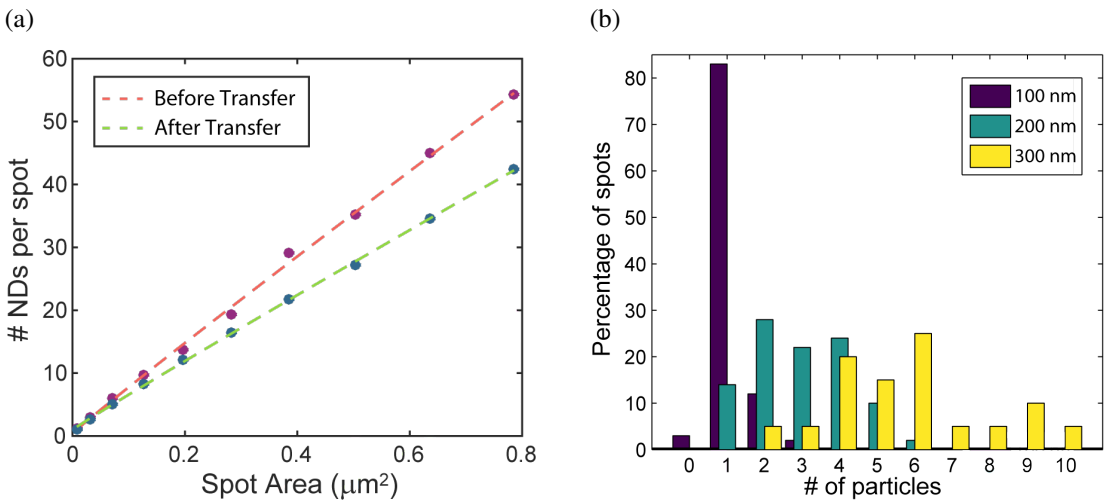

Figure 5.3: (a) Number of NDs per patterned spot as a function of the spot area A before and after the PDMS transfer procedure. We fit the data to $y = cA^{\alpha}$, where c is a free proportional factor and α assumes the value of 0.94 and 0.89 before and after the transfer respectively. (b) Histogram representation of the number of nanoparticle per spot for patterned circles with 100, 200, and 300 nm diameters before the transfer procedure. The vertical axis shows the percentage of analyzed spots showing a certain number of bound NDs (horizontal axis).

(Sylgard 184, Dow Corning Corp.) in a 10:1 mass ratio. The mixture is degassed in a vacuum chamber for one hour before being poured on the surface of the substrate with the ND arrays. The sample is then cured at 60 °C for 12 hours, during which the PDMS hardens and becomes an elastic solid material. The sample is allowed to cool to room temperature before the thin PDMS layer, and with it a portion of the NDs, is removed from the substrate and transferred on a clean silicon chip for characterization. We note that this transfer printing process could also be used to create portable arrays of the engineered diamond nanoparticles described in chapter 4, by taking advantage of the fact that the nanoparticles are loosely attached to the substrate.

5.4 Characterization of PDMS-nanodiamonds arrays

We now want to characterize the efficiency of the nanoparticles transfer into the PDMS layer and evaluate the PL properties of the resulting arrays.

We first conduct a SEM analysis of a series of patterned spots on the silicon substrate to estimate the number of nanoparticles that were removed in the transfer printing process. The result of

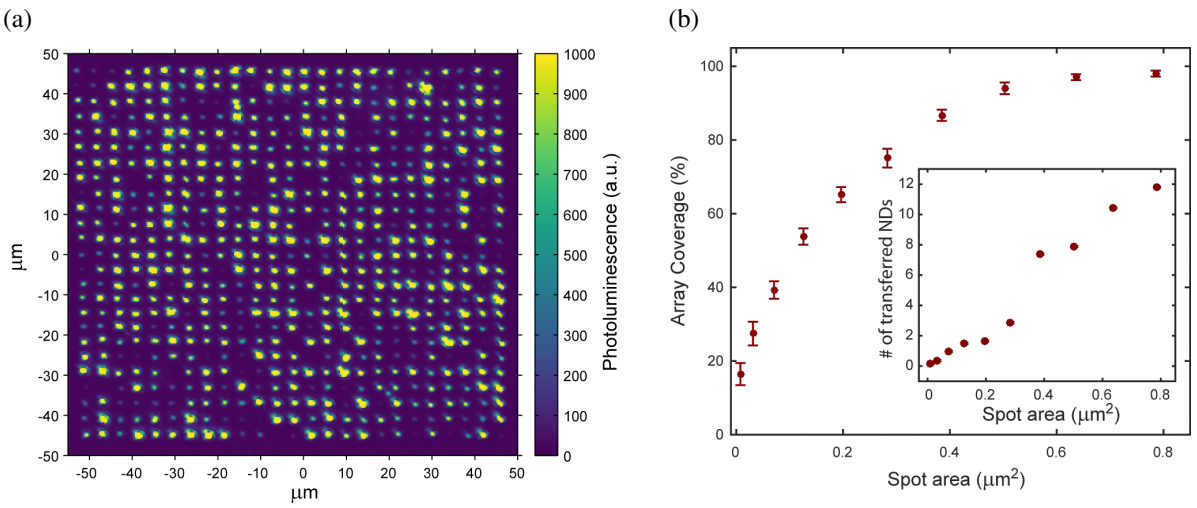

Figure 5.4: (a) Two-dimensional photoluminescence scan of an array of nanodiamonds embedded within a polydimethylsiloxane matrix obtained using a 25 by 25 array of 1000 nm diameter spots with 4 µm spacing. (b) Percentage of the array sites with at least one nanoparticle with detectable PL signal as a function of the patterned spot area. We measure between 9 and 11 arrays per spot size to build the statistics. In the inset we report the expected number of nanoparticle per site in the PDMS matrix as calculated from the data in Figure 5.3(a).

these measurements is shown in Figure 5.3(a) (green data points). From these measurements we conclude that the number of NDs that are removed from the substrate increases with the area A of the patterned circles. By fitting the data to $y = cA^{\alpha}$, where c is a free proportionality factor, we obtain for α the value of 0.89 ± 0.034, to be compared with 0.94 ± 0.052 for the data collected before the transfer process. This implies that the transfer efficiency moderately depends on the size of the patterned areas, with the larger ensembles of nanodiamonds being transferred more easily. We attribute this result to the aggregation of the NDs in small clusters in correspondence of the more populated spots, with the effect of allowing the removal of more than one particle at a time, and therefore increasing the effective transfer efficiency.

In the inset of Figure 5.4(b) we display the average number of nanoparticles that were removed from the substrate as a function of the patterned spot area as obtained from the data in Figure 5.3(a). This allows us to estimate the number of NDs per spot that we expect in the transferred arrays. Nevertheless, the uncertainty on these figures (not shown in the plot for clarity purposes) is comparable with their values, suggesting the presence of a wide spot-to-spot variability.

To gain further insight into the properties of the transferred ND arrays we characterize their PL collecting two dimensional scans of the signal using the custom-bulit confocal microscopy setup previously introduced. During these measurements the PDMS sample is placed on a bare silicon substrate with the nanodiamonds in contact with the silicon surface. In Figure 5.4(a) we present a typical PL map of a ND array obtained from a sample patterned with 1000 nm diameter spots and 4 µm spacing. As expected, the PL signal shows wide variations between different spots and we impose a limit to the the maximum plotted value of the PL to enable the visibility of most of the nanoparticles. For each patterned spot size we collect data on a series of ten arrays to investigate their quality in terms of the coverage percentage, defined as the percentage of array sites that result in at least one nanodiamond transferred to the PDMS layer. The result of these measurements is reported in Figure 5.4(b). The array coverage progressively increases with the area of the patterned spots and saturates close to the condition of full coverage ($98.0 \pm 0.8\,\%$) for the largest spots. Comparing these results with the number of expected transferred nanoparticles we see that using spots with $0.2\,\mu m^2$ area we can obtain arrays with $\sim 65 \pm 2\,\%$ coverage and $<$ 2 NDs per spots. This condition could be valuable for applications that require the use of single nanoparticles in order to simplify the interpretation of the data or optimize the PL contrast. On the other hand, temperature sensing application at zero field can take advantage of arrays with higher ND density and a larger PL signal.

5.5 Temperature sensing with PDMS-nanodiamonds arrays

We highlight the sensing capabilities of the PDMS-nanodiamond array system by demonstrating its potential as a thermal mapping device. In particular, as a proof of principle, we image the temperature profile generated by a coplanar waveguide (CPW) antenna that we concurrently employ to manipulate the NV centers' spin.

We position a ND array obtained with 1000 nm patterned spot diameter and 4 µm spacing in contact with a CPW patterned on a gadolinium gallium garnet (GGG) substrate and concentrate on a 9 by 9 particle subset that is located at a sharp bend in the antenna (see Figure 5.5), which

we expect to be particularly susceptible to temperature variations. To perform the sensing measurements we use the modified CW-ODMR scheme portrayed in Figure 5.5(a). The microwave input is alternated between a 100 µs, 0.4 W pulse off-resonant with respect to the NV centers' spin transitions, and a weaker 5 µs, 1 mW pulse of varying frequency. We use the former to simulate the presence of a heating source in the circuit, while the latter probes the NV centers' zero-field resonance as in a conventional ODMR experiment. Additionally, the PL signal is collected uniquely during the microwave probing pulse and a 500 ns time buffer separates the two microwave pulses to guarantee the absence of spurious frequency components from the strong heating pulse during the photon collection time bin. For each frequency of the probing microwave pulse we repeat the measuring sequence until we average the signal for $\sim$475 ms and the resulting ODMR traces are compared with calibration measurements collected with the heating pulse turned off. In particular, the shift in the zero-field splitting parameter D is calculated for each particle subtracting the values obtained from a Lorentzian fit of the ODMR spectra collected with and without the heating pulse. From the shifts in D we then estimate the values for the absolute temperature using $\frac{dD(T)}{dT}$ = 100 kHz/K[149], and the interpolated results are plotted in Figure 5.5(b), superimposed on a SEM image of the mapped CPW. As expected, we detect a higher temperature at the position of the signal line of the waveguide, and a shift towards lower temperatures with increasing distance from it. We also accurately image the presence of a hotter region in the inside corner where the signal line bends, which is associated to a higher current density at the inside edge of the metal.

In Figure 5.5(c) we report a simulated temperature map of the system obtained with Comsol Multiphysics®, which agrees qualitatively with the results in Figure 5.5(b). The model comprises both the sample (the GGG layer, the CPW, and the PDMS film) and a copper substrate on which the sample is mounted. Due to the complexity in modeling the heat transfer through wire connection to the CPW pads and to the rest of the setup, we treat the value of the heat transfer coefficient from the bottom of the copper substrate as a free parameter in the simulation to reach the same range of temperature that we experimentally measure. Nevertheless, we obtain a value for this parameter that is physically compatible with the heat sink on which the sample holder is mounted, and

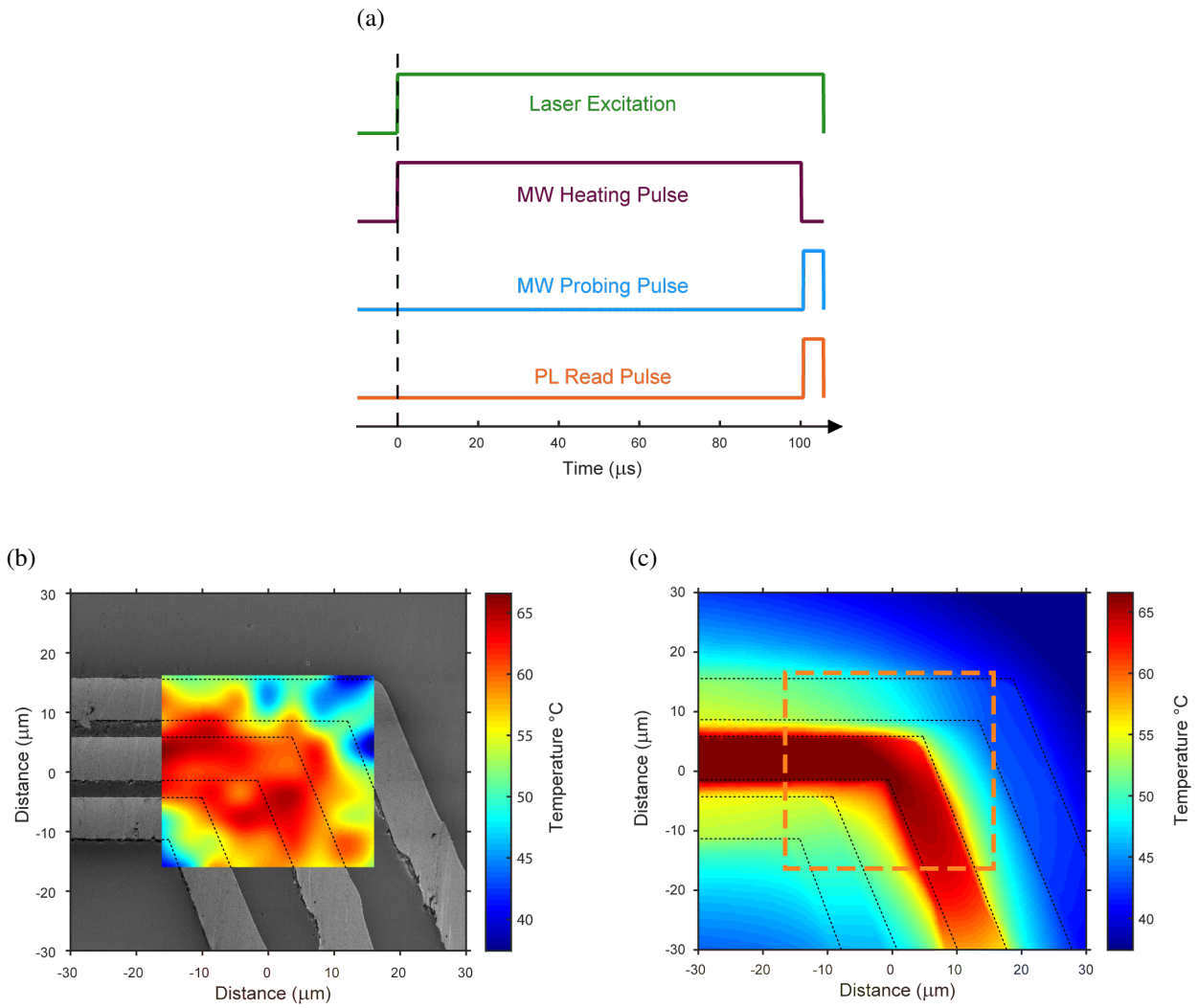

Figure 5.5: (a) Pulse sequence used to collect the ODMR spectra as the sample is being heated. The green excitation laser is always present while the microwave signal is switched between a 100 µs, 1.4 W of an off-resonant heating pulse and a 5 µs, 3.5 mW pulse of varying frequency used to probe the NV centers' resonance. At the same time the microwave probing pulse is applied a gating signal is sent to a data acquisition module to read the photoluminescence signal. A 500 ns delay separates the two microwave pulses to avoid spurious driving of the NV centers' spin during the acquisition time. (b) Temperature map of a CPW obtained from the interpolated data collected on a 9 by 9 array of nanodiamonds by detecting the shift in the zero-field splitting of ensembles of NV centers. The thermal image is superimposed on the SEM image of the CPW to identify the sample's features. (c) Simulation of the CPW's temperature map showing qualitative agreement with the data. The dashed box highlights the area that was investigated in the measurements shown in (b).

we therefore expect the results of the simulation to correctly represent the temperature variations across the sample. It is important to underline that no significant differences in the temperature

profile are present when the simulation is repeated without the PDMS layer, confirming that the low thermal conductivity of PDMS minimizes spurious effects on the thermal measurements. We note that the microwave signal used to probe the NV centers could also introduce a minor heating effect and modify the baseline temperature of the calibration measurements, nonetheless, as this signal is orders of magnitude smaller and has a smaller duty cycle than the heating pulse, we assume that we can neglect its effect.

In conclusion, we demonstrate that, using a combination of a directed assembly chemical pattern technique and a transfer printing process, we can fabricate arrays of nanodiamonds embedded in a transferable, transparent, and flexible matrix. Through the control of the chemical patterning parameters we showed the possibility of obtaining arrays with a wide range of nanoparticles per site. In particular, we can vary from 60 % coverage arrays with less than two NDs on average that are ideal for single ND or single NV center applications, to $\sim$100 % coverage samples with up to $\sim$10 NDs per spot that are optimal when high signals are advantageous. We also prove the temperature sensing potential of the ND arrays by imaging the thermal map of a CPW at the micrometer scale. This capability could have a great impact for the microelectronics community, where detailed knowledge of the temperature distribution and the mapping of hot spots is crucial for the devices' reliability and lifetime. We note that it is not necessary for the target sample to support the microwave signal used to probe the NV centers. This signal can indeed be applied using an antenna placed close to PDMS layer or patterned on its surface opposite to the NDs arrays.

The use of a widefield imaging setup and of ODMR measurements at a fixed probing frequency (see Section 2.3.1) would allow for fast and sensitive mapping of large arrays, paving the way to the scalability of the measurement with these systems. As we mentioned before, the transfer printing technique could also be used to create arrays with the engineered nanodiamonds described in the previous chapter, which would combine the portability of the PDMS system with optimal sensitivity properties.

In the next chapter we explore the possibility of combining transferable arrays of nanodiamonds with a ferromagnetic system in a hybrid architecture that could further enhance the capabilities of

the NV centers.

CHAPTER 6

LONG-RANGE SPIN WAVE MEDIATED CONTROL OF DEFECT QUBITS IN NANODIAMONDS

As discussed in Section 2.4, a major limitation to using NV centers to sense spins external to the diamond lattice is related to the trade-off between maximizing the sensor-target dipolar interaction and the decrease of the NV center's coherence in proximity of the diamond interface. Incidentally, the proximity requirements associated with magnetic dipole interactions also complicate the advancement of quantum information and computation applications that make use of NV centers or other analogous spin qubits in the solid state.

As we have seen, NV centers constitute remarkable single qubit systems, but in order to implement advanced quantum computing applications it is also necessary to couple multiple qubits and to control their coupling strength [33, 90]. While remarkable results have been obtained in recent years using optical coupling to entangle defects in diamond[7, 68, 120], these approaches require cryogenic temperatures and they are complex to scale to a large number of qubits on a single chip. Approaches based on direct dipolar interactions between multiple qubits[36], or mediated through the dipolar interactions with buffer spins[167] have the potential of working at room temperature, but face remarkable challenges regarding the placing and control of the single qubits. In Figure 6.1 we highlight the conditions in which two electronic spins can be strongly coupled to each other. From this it is clear that, even when taking advantage of the enhanced coupling of double quantum coherences[36], the NV centers need to be within few tens of nanometers to obtain collective coherent processes, particularly considering that spin coherences are usually $<200\,\mu$m for samples with high NV center density. This requirement translates into the necessity to deterministically position the NV centers with nanometer precision and to use super-resolution microscopy to separately address them with optical fields, which greatly complicates the fabrication and scaling of these systems.

Hybrid architectures that combine diamond with other materials and physical systems have

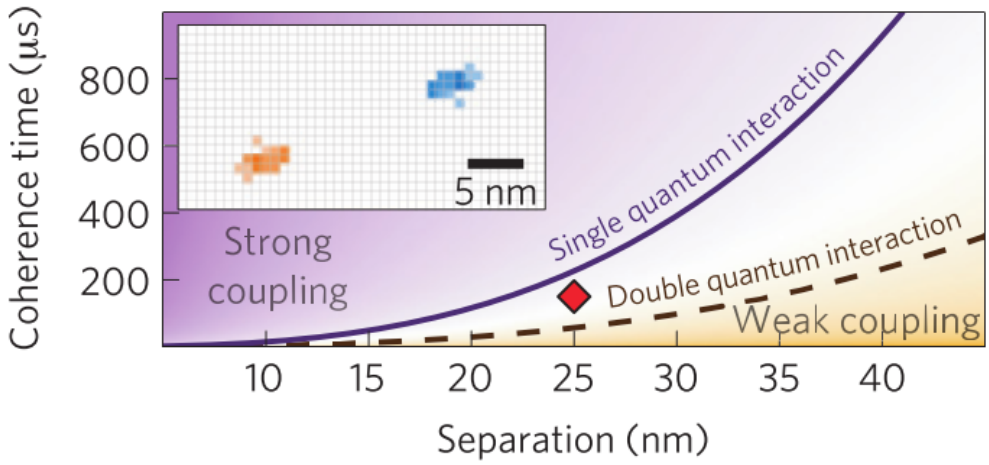

Figure 6.1: Coupling regimes for a pair of NV centers as a function of the shortest coherence time and their separation[36]. The solid line indicates the standard strong coupling limit, which can be increased using the enhanced couping of double quantum coherences (dashed line). The red diamond identifies the conditions used in [36]. The inset shows the optically resolved lateral distance between the two NV centers obtained by microwave-assisted super-resolution microscopy.

been recently proposed to overcome these limitations. Possible platforms that have been pursued (see Figure 6.2) involve the integration of diamond with nanoelectromechanical resonators[123] and with superconducting architectures[78, 89, 83]. A separate approach that has emerged as a promising candidate to enhance the NV center's capabilities in many quantum sensing and computing application relies instead on their interactions with spin-waves (SWs) in ferromagnetic materials. In this case the SWs' strong magnetic fields and long relaxation times could be used to efficiently interact with the NV centers and mediate their interactions. In particular, Trifunovic *et al.* [151] proposed to use virtual magnons in a ferromagnetic material as a bus to couple two distant NV centers dipolarly coupled with the ferromagnet (FM) (see Figure 6.3(a)), thereby easing the requirements on the defects' placing. Nonetheless, we note that this proposal requires the use of a FM with gapped excitations and that the thermal energy needs to to be smaller than the magnon gap, requiring the use of cryogenic temperatures.

Trifunovic *et al.* also introduced the possibility of amplifying the signature of a target spin by progressively converting the signal to be detected into variations of the magnetization of a nearby ferromagnetic particle, taking advantage of the slow decay of its magnetization[150]. Because

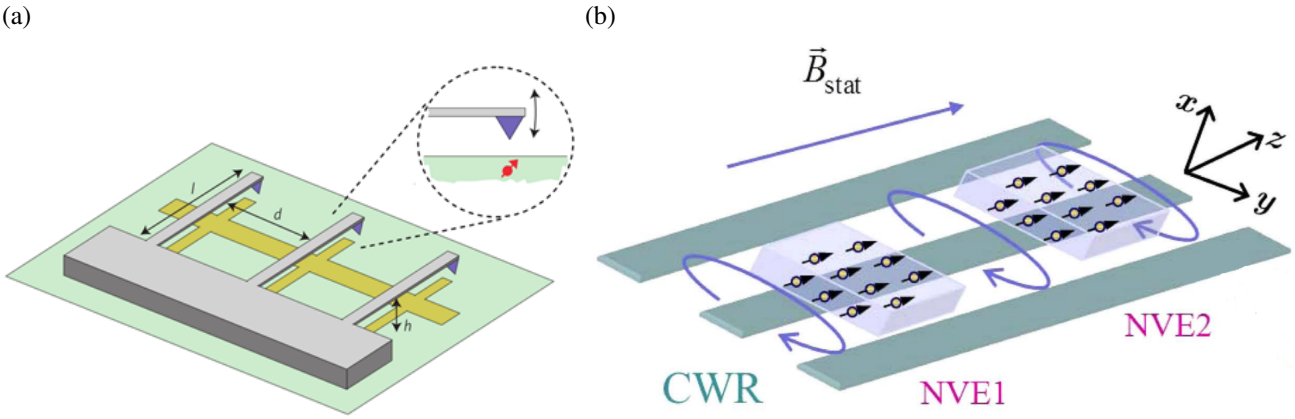

Figure 6.2: Hybrid quantum architectures proposed to implement strong coupling between NV centers. (a) Schematic of a system where the spin defects are coupled through an electromechanical quantum bus. The separate mechanical resonators are coupled indirectly through capacitive interactions with nearby metal wires[123]. (b) Proposed architecture for the coupling of two NV centers ensembles through their collective magnetic coupling to a superconducting coplanar waveguide resonator (adapted from [89]).

of this amplification, the NV centers can be located further away from the diamond surface (see Figure 6.3(b).

However, a number of recent works[162, 163, 118, 39, 154] revealed that the coherence of NV centers placed in proximity of a FM are strongly quenched by the presence of strong magnetic field noise generated by ferromagnetic excitation. While these results are of great interest for the implementation of broadband magnetic field sensing and for the study of the spin properties of ferromagnetic systems, they seem to suggest that incoherent mechanisms dominate the SW-NV center coupling. This would prevent the implementation of the proposals that we described, which crucially rely on the coherence nature of the interactions.

In this work, we develop a yttrium iron garnet ($Y_3Fe_5O_{12}$, YIG)-nanodiamond (ND) system integrating a thin YIG layer with an array of NDs embedded in a PDMS matrix (see Chapter 5) to further investigate these hybrid systems and evaluate their potential. We show that, under ambient conditions, surface confined Damon-Eshbach spin wave (DESW) modes excited in the YIG film using a microstrip line (MSL) antenna strongly interact with NV centers ensembles in NDs. Clear indications of the importance of the SWs surface nature for the strong enhancement

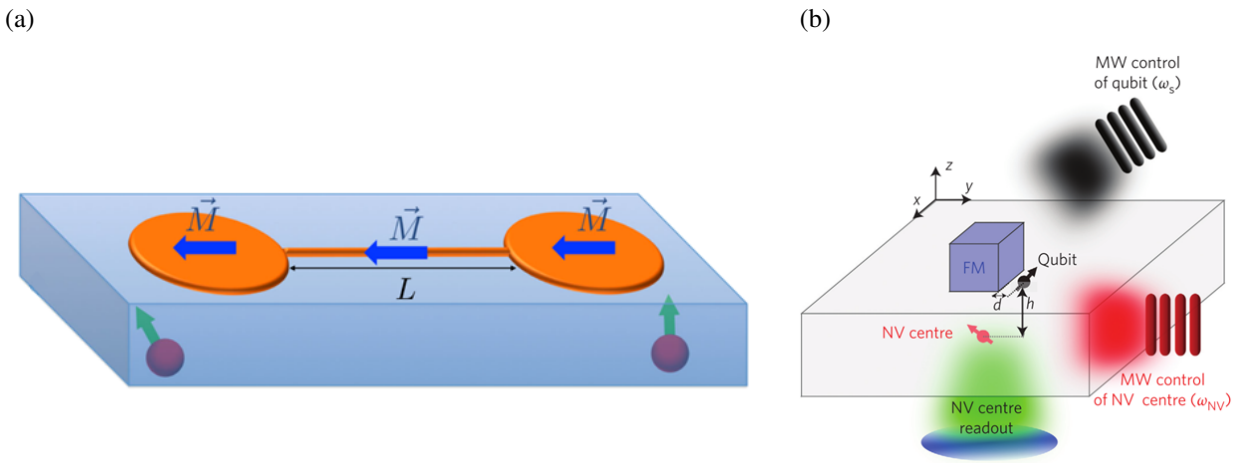

Figure 6.3: (a) Proposed ferromagnet/diamond platforms for long distance coupling of NV centers. The spin qubits (spheres with green arrows) are coupled to a monodomain ferromagnet (orange) via dipolar interactions. The blue arrows identify the ferromagnet magnetization[151]. The NV centers' coupling is obtained through the exchange of a virtual magnon across the ferromagnetic layer. (b) Proposed setup to implement enhanced hybrid sensing with spin qubits[150]. The ferromagnetic particle (FM) is positioned on top of a bulk diamond sample containing an NV center and in proximity of a target spin (called qubit here) to be measured. Separate microwave (MW) controls are used to manipulate the target spin and the NV center. The sensing scheme is based on inducing a precession of the macroscopic magnetization of FM through the resonant driving of the target spin. This in turns amplifies the AC magnetic signal detected by the NV center.

of the microwave-spin interactions is presented. Additionally, we demonstrate the existence of a microwave power regime where coherent coupling mechanisms between NV centers and SWs dominate over the effect of the FMs incoherent magnetic noise and we show that these coherent interactions are preserved over distances of up to 200 µm. Moreover, leveraging the strongly enhanced SW-NV interactions we show that the microwave magnetic field of the antenna can be amplified by several orders of magnitude and can uniformly deliver this enhanced driving field hundreds of micrometers away from the MSL.These results suggest the possibility of using SW mediated interactions to enhance the microwave signature of spin targets to be sensed by the NV centers. Additionally, our system could enable the implementation of high-sensitivity widefield thermometry applications, which would greatly benefit from a reduction in microwave power levels, as the microwaves measuring the NV centers can introduce heat in the system being probed.

In order to provide the background to explain our results, in the next section we are going to

briefly introduce the some basic concepts of spin wave theory and spin wave property characterization.

6.1 Spin waves: theory and measurements basics

Magnonics refers to the study of the transmission, storage and processing of information using SWs in magnetic films and nanostructures. SWs or magnons (the quanta of spin waves) are collective perturbations of a material's magnetization that arise from the precession of the individual magnetic moments in the system, which are commonly associated with the orbital and spin moments of electrons. In essence, they are the eigenexcitations of the electron spin subsystem in magnetically ordered materials[135]. Interestingly, the dispersion characteristics of these excitations can be widely varied by changing the material and the shape of the sample, or the orientation and amplitude of an externally applied magnetic field. Nevertheless, in general, spin waves frequencies fall in the gigahertz range and their wavelengths can reach the nanometer level, much shorter than the electromagnetic wavelength at the same frequency, making them particularly appealing for microwave information processing applications. However, until recently, most of the devices developed in the decades-long efforts in the field had been replaced by their semiconductor counterparts. In contrast, in recent years, a resurgence of interest in the field has emerged driven by one of the main limiting factors of semiconductor systems: the rapidly surging power consumption and dissipation with the increasing number of processing elements and their interconnections. SWs in spintronics devices can instead be manipulated without currents and can propagate without the displacement of charge carriers, offering a platform for low power information technologies[161].

Magnetic materials that are easily microfabricated as, for instance, permalloy, are very attractive for magnonics applications because they would allow for the development of complex magnonic circuits[77]. Unfortunately, SWs in these materials typically have very short lifetimes, of the order of nanoseconds[119]), and slow propagation speeds (roughly 4 orders of magnitude slower than the speed of light), which combine to give characteristic propagation lengths of the order of 10 μm[21]. On the other hand, monocrystalline YIG, while not as mature for nanofabrica-

tion applications, has very low damping parameters[50], resulting in SW lifetimes of the order of few hundreds of nanoseconds and propagation lengths up to centimeters. For this reason, and for its high Curie temperature T_c = 560 K, YIG provides a unique platform for the study of the SW dynamics and of their interactions with external systems at room temperature. Additionally, YIG, being an insulating ferromagnet, does not have free carrier which could introduce additional decoherence channels in a hybrid ferromagnet-diamond system. For these reasons YIG is still widely studied and we will focus on this material in this work.

6.1.1 Theoretical description of spin waves dispersion relations

Here we review a mathematical approach to derive the SW dispersion relation for a ferromagnetic system in the presence of an external magnetic field, which will be important to interpret the results that will follow. In particular, we focus on the case of magnetic field oriented in the plane in which the SW propagation occurs, as this is the condition in which all our measurements are collected. This treatment applies to any insulating ferromagnetic media but we will concentrate on discussing the results specifically for YIG.

At the microscopic level, the magnetic interaction between spins in a ferromagnet is dominated by the exchange interaction among neighboring spins and by dipole-dipole interactions at longer range. Obtaining an accurate description of the system using a microscopic model is nevertheless cumbersome and instead a macroscopic theory can be introduced, where the magnetization is considered as a continuously varying field obtained by coarse graining over the microscopic spin system. This can be done by replacing the individual magnetic moments with spacing a_i in the media with an average magnetization field $\mathbf{M}$. The procedure to define this field starts from the definition of discrete coordinates x_i spaced by dx_i, such that $a_i << dx_i << \lambda$, where lambda is the minimum SW wavelength of interest. The local magnetization field is then defined as

$$\mathbf{M}(\mathbf{r}) = \frac{\sum_{\mathbf{dr}} \boldsymbol{\mu}}{\mathbf{dr}} \tag{6.1}$$

where the sum is over all individual magnetic moments contained in the volume $\mathbf{dr} = \prod_i dx_i$, centered around the position $\mathbf{r}$. Due to the validity of the condition $dx_i << \lambda$, we can still consider $\mathbf{r}$ as a continuous variable.

In this macroscopic approach the magnetization dynamics is obtained combining Maxwell's equations in the ferromagnetic media and the equation of motion for the magnetization[26]. We note that, since at the relevant frequencies the SW wavenumber is much larger than that of the corresponding electromagnetic wave, the effect of displacement currents in the macroscopic Maxwell's equations can be ignored. Additionally, since we focus our attention on insulating ferromagnets, eddy currents are also negligible. At first we also neglect the effects of the exchange coupling, which is considered a valid approximation when the wavelength of the SW modes is large with respect to the characteristic exchange interaction coupling, while still small compared to the wavelength for electromagnetic propagation in the medium. Within this frame, the Maxwell's equations for the magnetic fields can be written as

$$\Delta \times \mathbf{H} = 0 \tag{6.2}$$

$$\Delta \times \mathbf{B} = 0, \tag{6.3}$$

with the usual boundary conditions that require the continuity of the normal component of $\mathbf{B}$ and of the tangential component of $\mathbf{H}$ at the sample surface. Additionally, all the fields must approach zero at large distances from the sample. We note that $\mathbf{H}$ is the effective internal magnetic field, which, in general, includes the contribution from the external magnetic field, shape anisotropy, magneto-crystalline anisotropy, and exchange interaction.

Assuming that the internal static field H_0 lies in the z direction, we can write the magnetic field and the magnetization in terms of their static and oscillating components as

$$\mathbf{H}(t) = H_0\hat{z} + \mathbf{h}e^{i\omega t} \tag{6.4}$$

$$\mathbf{M}(t) = M_s\hat{z} + \mathbf{m}e^{i\omega t} \tag{6.5}$$

where M_s is the saturation magnetization, $\hat{z}$ is a unit vector in the z direction and $\mathbf{h}$ and $\mathbf{m}$ are the amplitude vectors of the time-varying component of the field and magnetization respectively. The magnitudes $|\mathbf{h}|$ and $|\mathbf{m}|$ are assumed to be much smaller than H_0 and M_s, and therefore $|\mathbf{M}|$ is considered constant and $\mathbf{h}$ and $\mathbf{m}$ lie in the $\hat{x} - \hat{y}$ plane.

Introducing Equations 6.4 and 6.5 into Equations 6.2 and 6.3 we obtain Ampere's and Gauss' laws for the dynamic magnetic field and magnetization,

$$\Delta \times \boldsymbol{h} = 0 \tag{6.6}$$

$$\Delta \cdot (\boldsymbol{h} + 4\pi\boldsymbol{m}) = 0. \tag{6.7}$$

Equation 6.6 allows the definition of a magnetic potential ψ that satisfies $\boldsymbol{h} = \Delta\psi$ and we can rewrite Equation 6.7 as

$$\Delta^2\psi + 4\pi\Delta \cdot \boldsymbol{m} = 0. \tag{6.8}$$

The equation of motion for the magnetization, neglecting losses, is

$$\frac{\delta\mathbf{M}}{\delta t} = \gamma\mathbf{M} \times \mathbf{H} \tag{6.9}$$

where γ is the gyromagnetic ratio. Replacing $\mathbf{M}$ and $\mathbf{H}$ with Equation (6.4) and Equation (6.3), and considering only linear terms in $\mathbf{m}$ and $\mathbf{h}$, the equation of motion can be written as

$$
\begin{aligned}
4\pi m_x &= \chi \frac{\delta\psi}{\delta x} - i\kappa \frac{\delta\psi}{\delta y} \\
4\pi m_y &= i\kappa \frac{\delta\psi}{\delta x} + \chi \frac{\delta\psi}{\delta y}
\end{aligned}
\tag{6.10}
$$

where

$$
\begin{aligned}
\chi &= \frac{\omega_M \omega_H}{\omega_H^2 - \omega^2}, & \kappa &= \frac{\omega \omega_H}{\omega_H^2 - \omega^2}, \\
\omega_H &= \gamma H_0, & \omega_M &= 4\pi\gamma M_s.
\end{aligned}
\tag{6.11}
$$

Replacing Equation 6.10 into Equation 6.8 we obtain for the magnetic potential inside the sample ψ^i

$$
(1+\chi)\Big(\frac{\delta^2\psi^i}{\delta x^2} + \frac{\delta^2\psi^i}{\delta y^2}\Big) + \frac{\delta^2\psi^i}{\delta z^2} = 0 \tag{6.12}
$$

Outside the sample, where κ = 0 the potential ψ^e satisfies instead

$$
\Delta^2\psi^e = 0 \tag{6.13}
$$

We consider now the specific case of a ferromagnetic thin film of thickness L in the x direction, magnetized in the plane of the film (z direction), as in Figure 6.4. It's important to note that in this geometry the demagnetizing factor for the polarizing field vanishes and the internal effective field is equal to the external applied static field. By imposing the electromagnetic boundary conditions, we can obtain a relation between the SW wavevector components and its frequency[41]

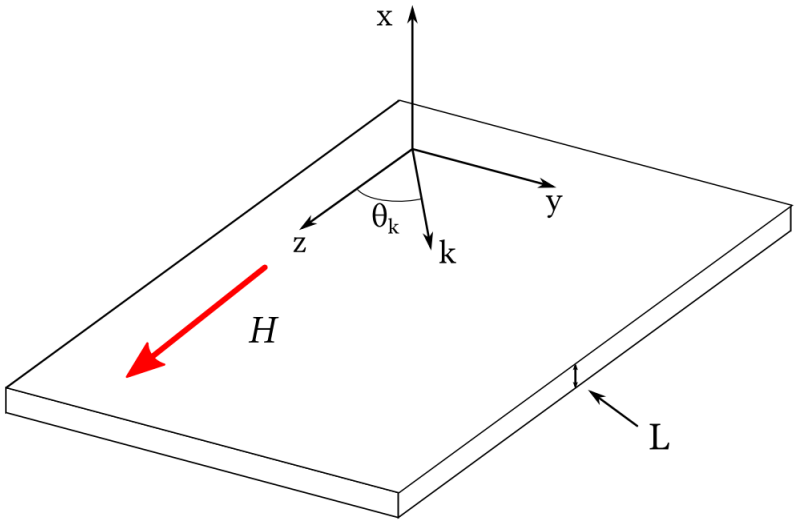

Figure 6.4: Schematic of the typical spin wave excitation geometry used in our measurements. A thin film of thickness L is magnetized in the plane of the film and SW with in-plane wavevector $k = \sqrt{k_y^2 + k_z^2}$ propagate at and angle θ_k with respect to the z axis. We assume that the film is infinite in the y - z plane.

$$k_{i,x} = \pm k\sqrt{-\frac{1+\chi \sin^2\theta_k}{1+\chi}} \tag{6.14}$$

$$k_{e,x} = k \tag{6.15}$$

$$k_{e,x}^2 + 2k_{e,x}k_{i,x}(1+\chi)\cot k_{i,x}L - {k_{i,x}}^2(1+\chi)^2 - \kappa^2 k^2 \sin^2\theta_k = 0 \tag{6.16}$$

where $k_{i,x}$ and $k_{e,x}$ are the x-components of the SW wavevector inside and outside the material respectively. Together these expressions provide a transcendental dispersion equation relating the mode frequency, the in-plane wavenumber k, and the in-plane propagation angle θ_k. This set of equations must be solved by numerical methods, but even in this form they provide some important insights on the properties of the propagating modes. For instance, the transverse wave vector inside the film can be real or imaginary depending on the sign of the quantity under the radical sign in Equation 6.14

$$-\frac{1+\chi \sin^2\theta_k}{1+\chi}. \tag{6.17}$$

which translates into a sinusoidal and a decaying exponential profile for the dynamic magnetization respectively.

To better analyze the conditions for these different regimes we can expand Equation 6.17 in terms of ω,ω_H, and ω_M

$$\frac{\omega^2 - (\omega_H^2 + \omega_H\omega_M \sin^2\theta_k)}{(\omega_H^2 + \omega_H\omega_M) - \omega^2}. \tag{6.18}$$

Here we can see that the frequency range where this expression is positive and therefore the magnetization oscillation inside the medium is sinusoidal, is

$$\omega_H^2 + \omega_H\omega_M \sin^2\theta_k < \omega^2 < \omega_H^2 + \omega_H\omega_M. \tag{6.19}$$

Modes that satisfy this requirements are called volume modes as their dynamic magnetization is distributed across the whole film thickness. From Equation 6.19 we see that for fixed values of H_0, M_s, and ω, the type of magnetization profile that we obtain depends on the in-plane propagation angle θ_k. For instance, for θ_k = 0, no volume mode can be excited in the system.

These results suggest that for values of ω that do not satisfy Equation 6.19, modes with imaginary wavevector, and therefore dynamic magnetization exponentially decaying away from the surface exist. A more detailed analysis [64], shows that these surface modes do not occur at frequency below the volume mode band, and instead appear only in the frequency range given by

$$\omega_H^2 + \omega_H\omega_M < \omega^2 < \omega_H^2 + \omega_H\omega_M + \frac{(\omega_M \sin^2\theta_k - \omega_H \cos^2\theta_k)^2}{4\omega_M^2 \sin^2\theta_k} \tag{6.20}$$

$$\text{for} \qquad \theta_k > \arctan\sqrt{\frac{\omega_H}{\omega_M}}. \tag{6.21}$$

To complete the analysis of SW modes in ferromagnetic thin films, we need now to add the

effect of the exchange interactions, which was so far neglected. It can be shown[74] that this effect can be represented as an additional effective magnetic field $\boldsymbol{H}_{exc} = q\nabla^2\boldsymbol{M}$, where q is called the exchange constant. The presence of this additional exchange field requires additional boundary conditions for the dynamic magnetization, which reflect the impact of surface anisotropy on the spin precession at the boundaries. Following this treatment it is possible to obtain a simple analytical description for the SW modes dispersion relation for an in-plane magnetized film[70]

$$\omega_n^2 = (\omega_H + q\omega_M k_n^2)(\omega_H + q\omega_M k_n^2 + \omega_M F_{nn}), \tag{6.22}$$

with,

$$F_{nn} = 1 - P_{nn}\cos^2\theta_k + \omega_M \frac{P_{nn}(1 - P_{nn})\sin^2\theta_k}{\omega_H + q\omega_M k_n^2}, \tag{6.23}$$

where $k_n^2 = k^2 + \kappa_n^2$, $\kappa_n = \frac{n\pi}{L}$, and n is an integer index that identifies the modes with different wave amplitude periodicity across the ferromagnetic film thickness. In the approximation of totally unpinned surface spins, which is common for high quality YIG films grown with liquid phase epitaxy techniques, we can express P_{nn} as

$$P_{nn} = \frac{k^2}{k_n^2} - \frac{k^4}{k_n^4} G_n \frac{1}{1 + \delta_{0n}} \tag{6.24}$$

where δ_{0n} is the Kroenecker's delta and

$$G_n = \frac{2}{kL}[1 - (-1)^n e^{-kL}]. \tag{6.25}$$

In summary, two distinct classes of SW with markedly different dispersion relations and magnetization profile can be excited in an in-plane magnetized thin ferromagnetic film. In particular, it will be important in what follows that, for a given geometry and magnetic field, the type of modes that are excited depends on the orientation of the applied bias magnetic field relative to the direction of the SW propagation.

In the case of propagation parallel to the external field (and therefore to the magnetization) we purely excite volume modes commonly called backward volume magnetostatic waves (BVMSW). Reverting to the approximation of negligible exchange interaction (q = 0), which is a good assumption for all the measurements that will follow (for YIG $q = 3 \times 10^{-12}$, which implies $qk^2 << 1$), the expression in 6.22 for $n = 0$ reduces to

$$\omega_{\text{BVMSW}} = \sqrt{\gamma H_0 \left(\gamma H_0 + 4\pi\gamma M_s \left[\frac{1 - e^{-kL}}{kL} \right] \right)} \tag{6.26}$$

One interesting property of these curves (see Figure 6.9) is their negative slope, and consequently the negative group velocity of the propagating modes. This implies that the phase and group velocities of BVMSW modes are counter-propagating (and hence the name "backward volume"), and that an increase in the wavevector is associated with a decrease in the mode frequency.

When the bias magnetic field is instead oriented perpendicularly with respect to the propagation direction of the SWs we instead excite magnetostatic surface spin waves, often referred to as Damon-Eshbach spin waves (DESWs). It is possible to show that in this configuration only one mode exist[139] and its dispersion curve in the approximation of negligible exchange interaction can be written as

$$\omega_{\text{DESW}} = \sqrt{\left(\omega_H + \frac{\omega_M}{2}\right)^2 - \left(\frac{\omega_M}{2}\right)^2 e^{-2kL}}, \tag{6.27}$$

Interestingly, these modes present the phenomenon of field displacement non-reciprocity. When the direction of the SW propagation is reversed, the dispersion relation is not affected but the localization of the dynamic magnetization shifts from one surface to the other.

6.1.2 Principles of spin wave measurements

In this section we introduce the principles of spin wave excitation and detection by means of microwave stripline (MSL) antennas, which is the technique that we will use in our measurements[135].

Figure 6.5 shows the typical configurations used to characterize the spin wave properties of

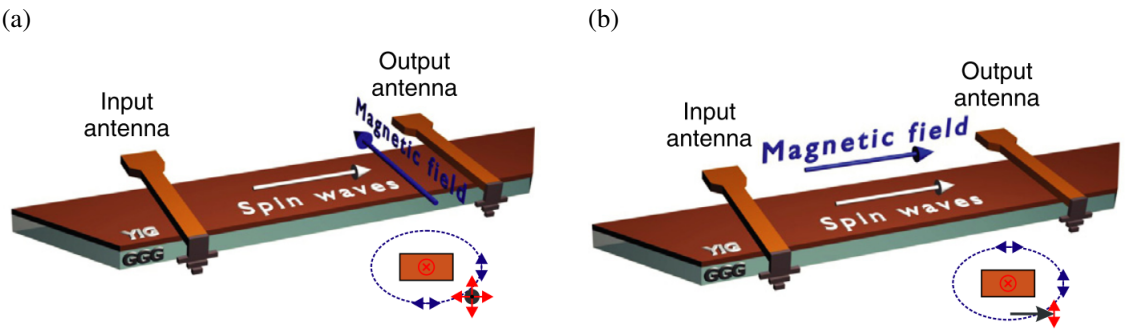

Figure 6.5: Schematic of the experimental setups for the study of BVMSW (a) and DESW (b) modes, and their respective excitation mechanism.

a ferromagnetic system (YIG here). Two microstrip antennas are patterned on a sample whose edges are commonly cut at a 45° angle to avoid SW reflection. In essence, the oscillating field of one of the antennas (input) is used to excite SWs propagating towards the second antenna, which inductively detects their electromagnetic signature.

To obtain a more detailed description of this process, we can consider again the ferromagnetic material as a collection of quasi-classical magnetic moments that, when the system is magnetically saturated, have their precessional axis parallel to the bias field. When a microwave signal is applied, the antenna generates alternating Oersted magnetic fields in the material. In the conditions for the excitation of DESW modes (Figure 6.5(b)) two components of the microwave magnetic field are orthogonal to the direction of the static magnetization and therefore can exert a torque on the magnetic moments and induce their precession. The spins driven by the antenna's field in turn interact with their nearest neighbors, exerting a torque that influence their precession. When the frequency of the oscillating field is resonant with one of the allowed SW modes, SW propagation is supported. The interplay between the two field component is what leads to the non-reciprocity of these modes[131]. Using time-reversal symmetry arguments we can also understand the mechanism for the detection process. When the SW arrives at the location of the second antenna, the oscillating electromagnetic field generated by the magnetic moments induces an oscillating current in the antenna. Therefore, connecting the input and output of a network analyzer to the two antennas we can obtain information on the SW spectrum in the system simply by collecting S-parameter data[168].

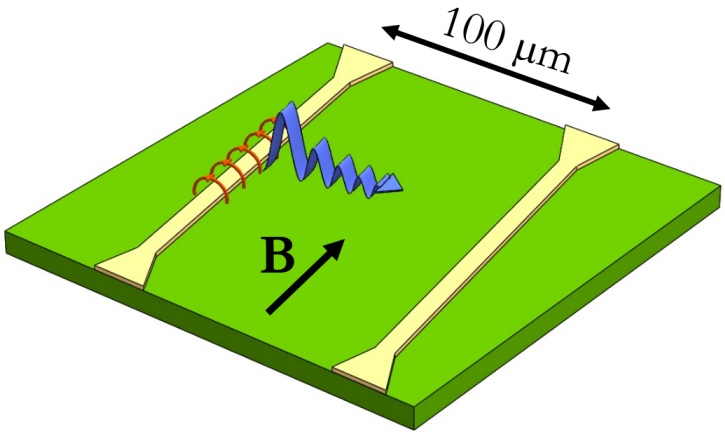

Figure 6.6: Geometry used in the SW spectra measurements. The ferromagnetic layer is a 3.08 μm thick single-crystal YIG film epitaxially grown on a 500 μm GGG substrate. To apply and detect microwave fields, pairs of 5 μm wide microstrip lines (MSL) are patterned with different separations on the YIG. For the measurements reported in this section we selected a 100 μm separation. The microwave magnetic fields (circles) and propagating spin waves (purple) are sketched.

Similar considerations apply in the conditions for BVMSW excitation(Figure 6.5(a)), but in this case the horizontal component of the oscillating field is parallel to the external bias field, and therefore cannot introduce a torque on the magnetic moments. For this reason, the excitation of SWs with a MSL is less efficient for BVMSWs than for DESWs.

Using the theoretical framework that we introduced and the microwave transmission measurements described in this section, we are now going to study the specific spin wave properties of the samples used in our work. As we will be interested in the effects of the resonant interactions between SWs and NV centers, calculating and experimentally measuring the SW spectra is important to ascertain where it overlaps with the NV center's spin resonances.

6.1.3 Damon-Eshbach spin wave spectra

The geometry of the setup used in our measurements is analogous to the ones we previously discussed (Figure 6.5), and it is schematically shown in Figure 6.6 for the case of DESW modes excitation. A pair of 5 μm wide striplines (Ti/Au, 10 nm/200 nm), separated by 100 μm is lithographically patterned on the surface of a L = 3.08 μm thick YIG layer epitaxially grown on a gadolinium gallium garnet (GGG) substrate (MTI Corp., YIG-GGG-100505). The MSLs are tilted

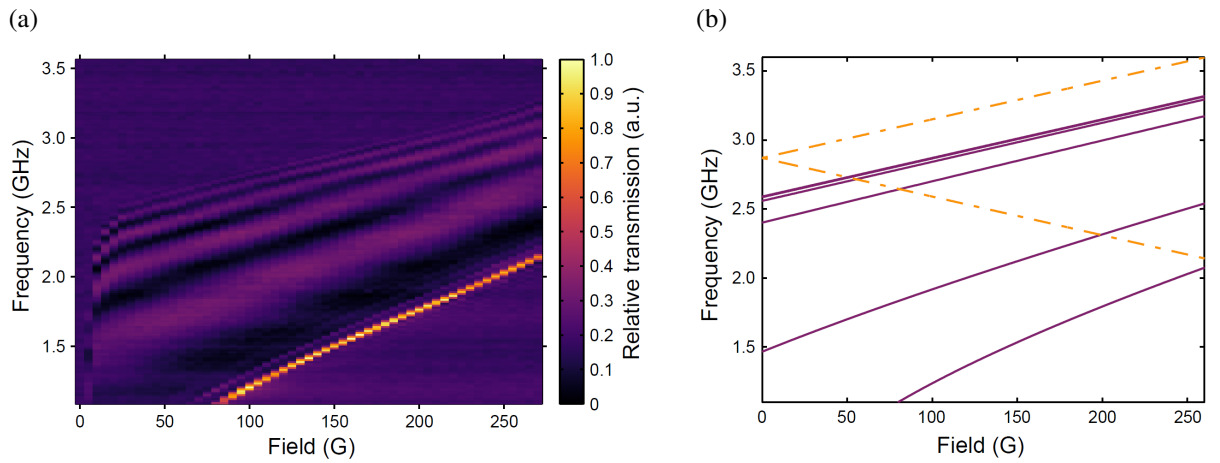

Figure 6.7: (a) Microwave transmission spectrum collected using two MSLs 100 µm apart as a function of the externally applied magnetic field for θ = 0. The data for 0 G were subtracted from the data at higher fields to eliminate features that are not field dependent. (b) Simulated DESW spectrum. The dashed lines enclose the range of frequencies where the NV centers ground state spin resonances are located.

with respect to the sample edges to avoid SW reflections. As mentioned above, YIG is chosen as a substrate because of its small damping parameter for spin wave propagation in the GHz frequency range, which makes it ideal for studying long-range interactions.

In Figure 6.7(a) we show the result of the microwave transmission measurements, showing the spectrum of the DESW modes as a function of the externally applied magnetic field. The zero-field measurement is used as a reference for the ones at higher fields to eliminate the features in the spectrum that are not magnetic field dependent. We also calculate the theoretical spectrum of the DESW modes following the principle of wave vector matching[56], and therefore assume that the efficiency of the excitation of a SW with wave vector k (in rad/cm) and frequency f (in Hz) depends on the amplitude of the Fourier Transform (FT) of the exciting microwave field at the same values of k and f. To obtain the FT of the Oersted fields $\boldsymbol{h}_{FT}$ that are generated in the experiments we perform a simulation of the microwave stripline (MSL) antennas using the CST Studio Suite toolkit. In Figure 6.8(a) we show the FT of the x ($|h_{kx,FT}|$) and z ($|h_{kz,FT}|$) component of the oscillating magnetic field. For $|h_{kx,FT}|$, we omit the points for small values of k, which contain spurious oscillations originating from the discretization of the FT calculation. The SWs that can be efficiently excited are the ones with k close to the maxima of $|h_{kx,FT}|$ and $|h_{kz,FT}|$. Next, we

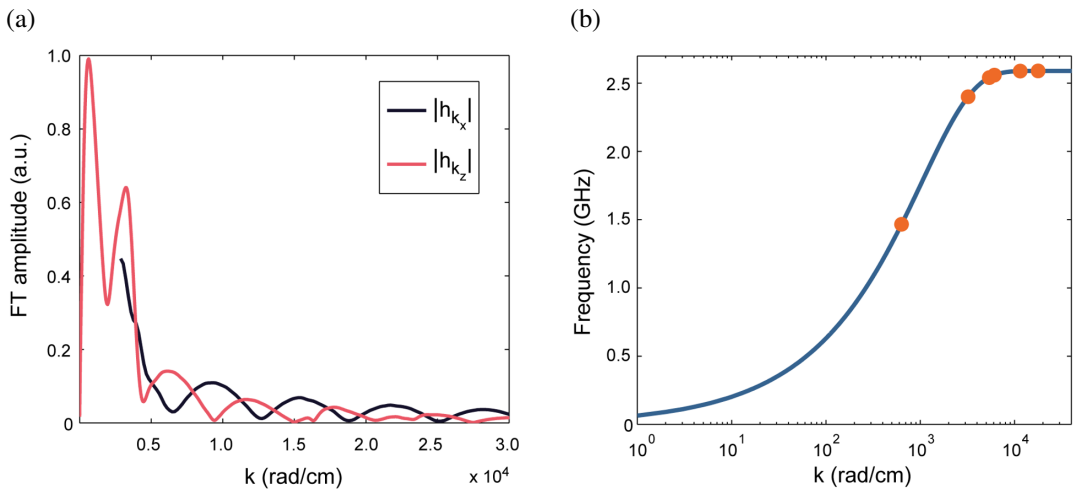

Figure 6.8: (a) Fourier transform of the x and z components of the Oersted magnetic field generated by a stripline antenna of width w = 5 µm. b, Dispersion relation of the DESW mode for H_0 = 0 G. The points corresponding to the first 6 combined maxima of $|h_{kx,FT}|$ and $|h_{kz,FT}|$ with $k > 0$ are highlighted on the curve.

need to consider the dispersion relation for the excited SW modes. As mentioned earlier and as it is clear from Figure 6.8(a), we can neglect the effect of the exchange interaction ($qk^2 << 1$) and use Equation 6.27, written here using the explicit dependence on H_0 and M_s

$$f_{\text{DESW}} = \gamma\sqrt{\left(H_0 + \frac{4\pi M_s}{2}\right)^2 - \left(\frac{4\pi M_s}{2}\right)^2 e^{-2kL}}, \tag{6.28}$$

where γ = 2.8 MHz/G is the electron gyromagnetic ratio, and from the fit of the Kittel mode (mode with k = 0) in the network analyzer data, we obtain $4\pi M_s$ = 1850 G. The DESW dispersion curve is shown in Figure 6.8(b) for the case H_0 = 0 in the range of wave vectors of interest and the points that correspond with the first few maxima of $|h_{kx,FT}|$ and $|h_{kz,FT}|$ (k = 0 is not shown) are highlighted. These identify the SWs that are efficiently excited by the MSL and when we plot the frequency of these SWs as a function of H_0 we obtain the spectra in Figure 6.7(b). In the same figure (dashed lines) we identify the frequency range for the NV center spin ground state resonances, which is enclosed by the resonance spectrum for a defect aligned with the external magnetic field. Even though the nanoparticles have random crystal orientations, their resonances inherently fall within this range.

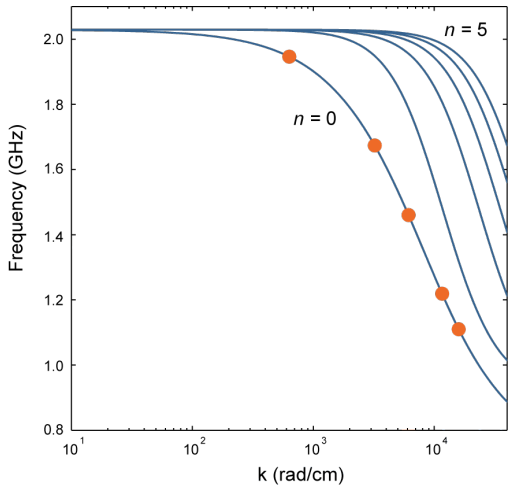

Figure 6.9: Dispersion relations of the BVMSW modes with n ranging from zero to five in the case of H_0 = 250 G. The points corresponding to the first four maxima of $|h_{k_x,FT}|$ with $k > 0$ are highlighted on the n = 0 curve.

The measured and calculated spectra that we obtained are in good agreement and although the calculation does not capture all of the features in the measured spectra, this is likely the result of the necessarily simplified model for the MSL used to simulate the driving oscillating field. Nevertheless, the simulated spectrum confirms that the DESW modes are expected to be resonant with the NV center transitions in the range of magnetic fields of interest.. It is important to note in what follows that DESW excitations with higher frequencies (at a fixed external field) are associated with larger wave vectors k, and display a more pronounced surface confinement. In particular, both the magnetization oscillations within the ferromagnetic layer and the field generated outside decay exponentially with characteristic length $1/k$ in the direction orthogonal to the YIG surface[139].

6.1.4 Backward volume spin wave spectra

Finally we analyze the spin wave properties in the case of an external magnetic field oriented in the plane of the YIG film and parallel to the SW direction of propagation, which results in the excitation of pure BVMSW modes. To theoretically estimate the spectrum of these modes we follow the same approach detailed for the calculation of the DESW spectrum. As we have mentioned earlier, in this configuration only the component of the antenna microwave field orthogonal to the YIG

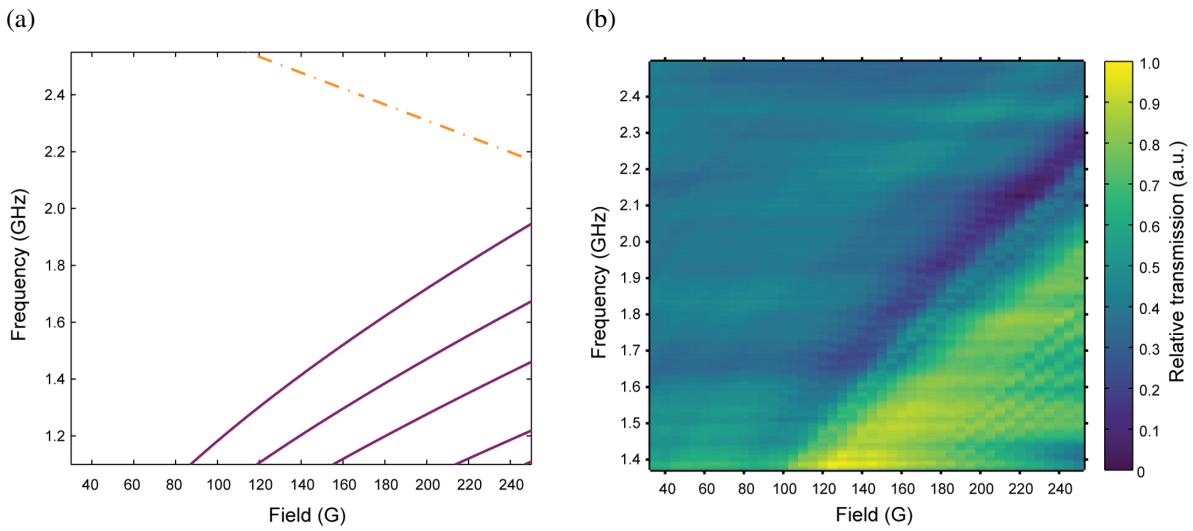

Figure 6.10: Spectrum of the BVMSW modes (a) as obtained from a microwave transmission measurement and (b) as calculated using the magnetic field dependence of the four excitations highlighted in Figure 6.9. The dashed line represents the lower branch of the ground state excitation of a NV center with axis aligned to the external magnetic field.

plane contributes to the SWs excitation, and the values of k of the SWs that are efficiently excited by the antenna can be obtained from the maxima of $|h_{kx,FT}|$, shown in Figure 6.8(a).

The dispersion relation for the BVSMW modes in the approximation of negligible exchange interaction can be written as[69],

$$f_{\text{BVMSW}} = \gamma\sqrt{H_0(H_0 + 4\pi M_s(1 - P_{nn}))}, \tag{6.29}$$

and, in the assumption of totally unpinned surface spins, P_{nn} has the form,

$$P_{nn} = \frac{k^2}{k^2 + (\frac{n\pi}{L})^2} - \frac{k^4}{(k^2 + (\frac{n\pi}{L})^2)^2} G_n \frac{1}{1 + \delta_{0n}} \tag{6.30}$$

and G_n is the same as in Equation 6.25.

In Figure 6.9 we plot f_{BVMSW} for the case H_0 = 250 G and for values of n ranging from zero to five. We also highlight the points on the n = 0 dispersion curve corresponding to the first few maxima of $|h_{kx,FT}|$. In Figure 6.10(b) and Figure 6.10(a) we report the calculated energy spectra for the n = 0 spin wave excitations as a function of the external magnetic field and the SW spectrum

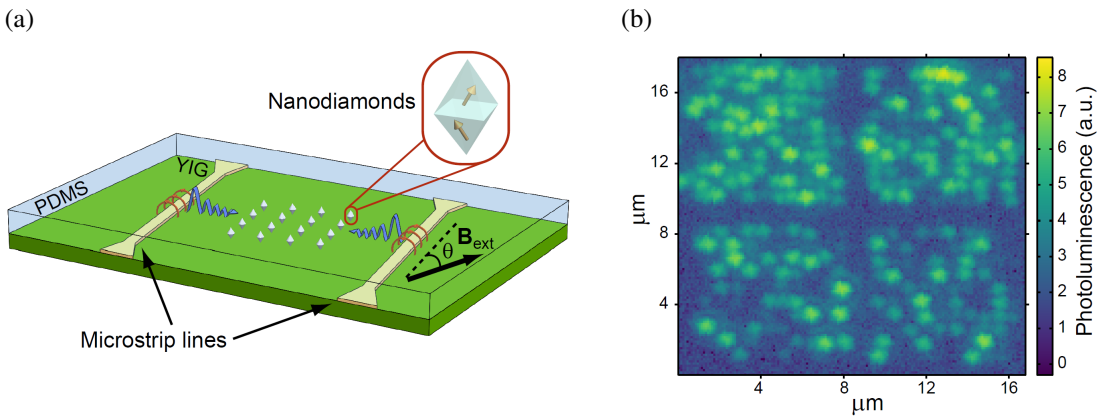

Figure 6.11: Complete hybrid ferromagnet-nanodiamond system. A ∼300 µm thick PDMS strip with an array of NDs embedded on its surface is placed in contact with the YIG substrate in proximity of the microstrip lines (MSLs). The external magnetic field can be applied at an angle θ with respect to the MSLs. The arrows in the ND represent the NV center spins, with each ND containing hundreds of NV centers. (b) Spatial photoluminescence scan of ND arrays collected using a confocal microscopy setup.

as obtained through a microwave transmission measurement respectively. We limit the magnetic field and frequency range of these data for the sake of clarity as it allows us to remove additional SW-independent features in the spectrum that appear particularly at low fields[163]. We again attribute the differences between the theoretical and experimental spectra mainly to imprecisions in the simulation of the oscillating magnetic field generated by the MSL.

6.2 Hybrid platform setup

We now proceed to integrate the ferromagnetic system in a hybrid architecture to study the interactions of SWs and NV centers. To do this we take advantage of the ordered nanodiamond platform described in Chapter 5. In particular, we use a ∼300 µm thick strip of PDMS with embedded an array of commercial NDs (Adamas Technology, ∼500 NV centers per particle) with a ∼1 µm pitch, which can be positioned in contact with the YIG substrate. Employing a portable and reusable system allows us to control the position of the NDs with respect to the MSLs and to easily locate and address single nanoparticles, which is critical for performing our measurements. For this reason, in all the measurements that follow we will concentrate on sites occupied by a single

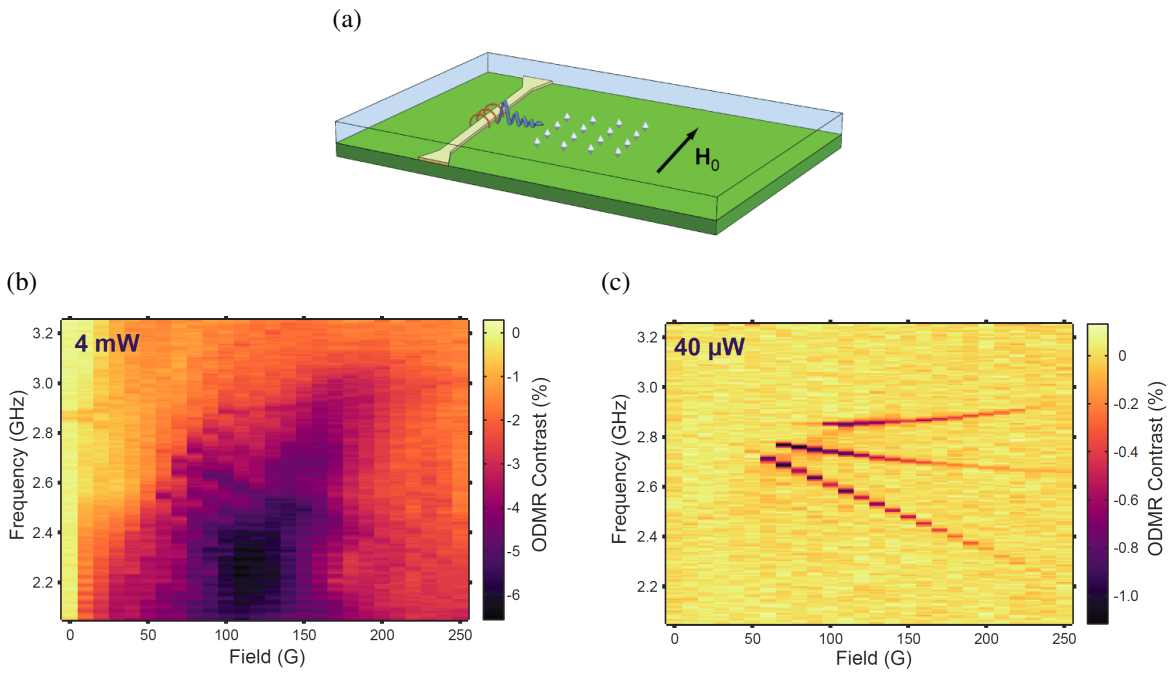

Figure 6.12: ODMR spectra collected in the case of θ = 0 (a). In this condition, we excite DESW modes confined at the surface closest to the NDs. For a microwave power that allows us to resolve the ODMR resonance at zero field (b) a strong, broadband PL quenching is visible when the magnetic field is increased. By decreasing the microwave power by two orders of magnitude (c) we enter a regime where the non-resonant PL quenching is suppressed and discrete NV center resonances are visible at fields above 60 G.

nanodiamond. Additionally, the flexibility of the PDMS guarantees the presence of close contact between the NDs and the YIG substrate.

The complete hybrid architecture is shown in Figure 6.11(a) and in Figure 6.11(b) we present a two-dimensional photoluminescence scan of some nanodiamonds arrays, collected using our custom-built confocal microscopy setup. All the measurements presented in the following are collected using this apparatus and are performed at ambient conditions.

6.3 Optically detected resonant interactions

To begin to investigate the extent of the DESW-NV centers interaction, we perform optically detected magnetic resonance (ODMR) measurements using one of the MSLs in our setup to drive microwave fields. Specifically, we detect changes in the NV centers' PL associated with the cou-

pling of their spins to the SWs oscillating magnetic field. Figure 6.12 shows the magnetic field configuration used for these measurements and the ODMR spectra obtained on a nanoparticle labeled NP-P, located $\sim$40 µm away from the MSL. In Figure 6.12(b), we report the results obtained using 4 mW of microwave power, which is the lowest power that still resolves the NV center's resonances at low fields. When we increase the external magnetic field, we observe a broad feature of increasing frequency that intersects the NV center resonances following the SW modes expected behavior (Figure 6.7). Recent studies have shown the presence of weaker off-resonant features in the NV centers ODMR spectrum[162, 118] ascribed to the shortening of the NV center longitudinal spin coherence time (T_1) caused by the broadband magnetic field noise introduced by the excited spin waves. Because of the extensive quenching effect on the spin coherence of the NV centers, it is not possible to isolate the effect of resonant interactions between the SWs and the spin qubits at this microwave power level.

When we instead decrease the input microwave power by two orders of magnitude (Figure 6.12(c)), the off-resonant quenching is suppressed and we observe some of the NV centers discrete resonances. We observe that these resonances are visible only for magnetic fields above 60 G, which corresponds to the field at which we expect the resonances to intersect the SW modes (see Figure 6.7(a)). The absence of optical contrast below this field, which corresponds to a lack of microwave driving of the NV centers, demonstrates that the effect of the antenna field is negligible at the ND location and that the NV center driving is purely SW mediated. We also note that only the lower branches of the NV centers ground state spin transitions are visible and attribute this to the fact that the upper branches do not intersect the SW resonances, as can be inferred from Figures 6.7(a) and 6.7(b). While the data in Figure 6.12(c) do not reflect the presence of the discrete series of SW excitations expected from the DESW spectrum, this result is the effect of the broadband nature of the SW-induced NV center photoluminescence quenching and of the coarse frequency and field resolution of these measurements. Indeed, when we collect measurements using a finer resolution we can resolve the effect of separate excitations, as it is visible in Figure 6.13(a), where we show a subset of the ODMR spectrum. Finally, we note in Figure 6.12(c)

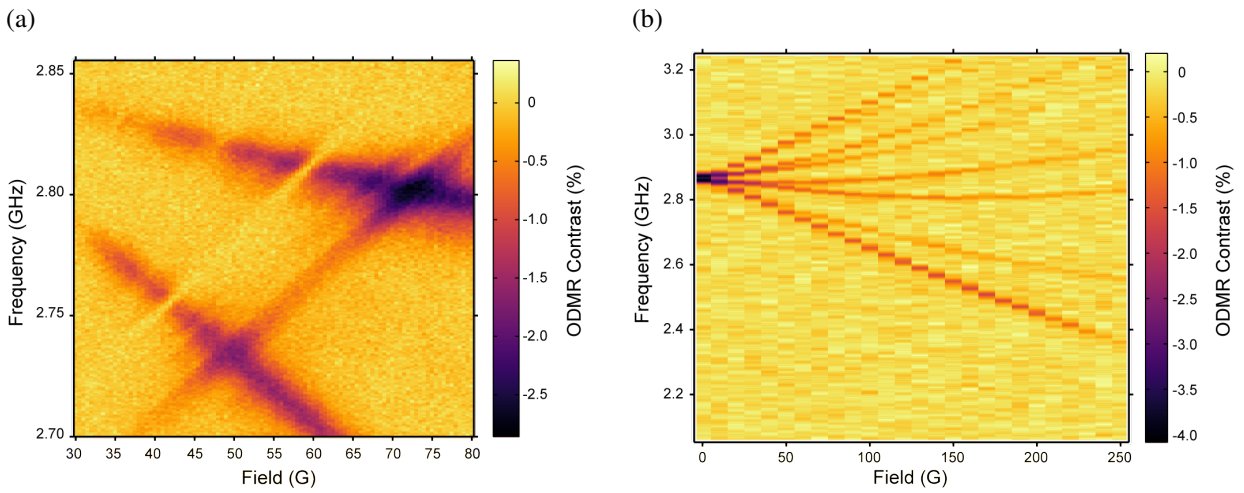

Figure 6.13: (a) ODMR spectrum collected with 0.5 MHz and 0.5 G resolution that shows the presence of features attributed to the discrete nature of the SW excitations. This measurement was collected on a particle ∼5 µm away from the antenna using 0.5 µW of microwave power. (b) ODRM spectrum of a nanodiamond on a GGG substrate. These data were collected from a diamond nanoparticle ∼5 µm away from the antenna using 16 mW of microwave power. A microstrip line with equivalent transmission characteristics as the ones patterned on the YIG substrates was used to deliver the microwave signal. Only discrete NV centers resonances are visible in the ODMR spectrum.

that the interaction appears to be stronger for the SWs associated with larger wave vectors, as can be deduced from the decrease in ODMR contrast at higher fields, where the NV centers resonances cross lower k modes. This is consistent with a stronger surface confinement of the magnetization oscillations for higher values of k.

We observe strong SW-NV centers interactions on numerous nanoparticles using multiple MSLs and YIG substrates. As a control, ODMR measurements are collected also for NDs positioned on a GGG non-magnetic substrate, where no off-resonant interactions nor enhanced resonant interactions are observed (see Figure 6.13(b)).

6.4 Dependence on the magnetic field orientation

In order to gain insight into the role the SW's surface confinement plays in the strong coupling enhancement, we investigate the effect of the magnetic field orientation on the PL contrast for the cases $\theta = \pi$ and $\theta = \pi/2$. In these conditions the excited spin waves have different dispersion

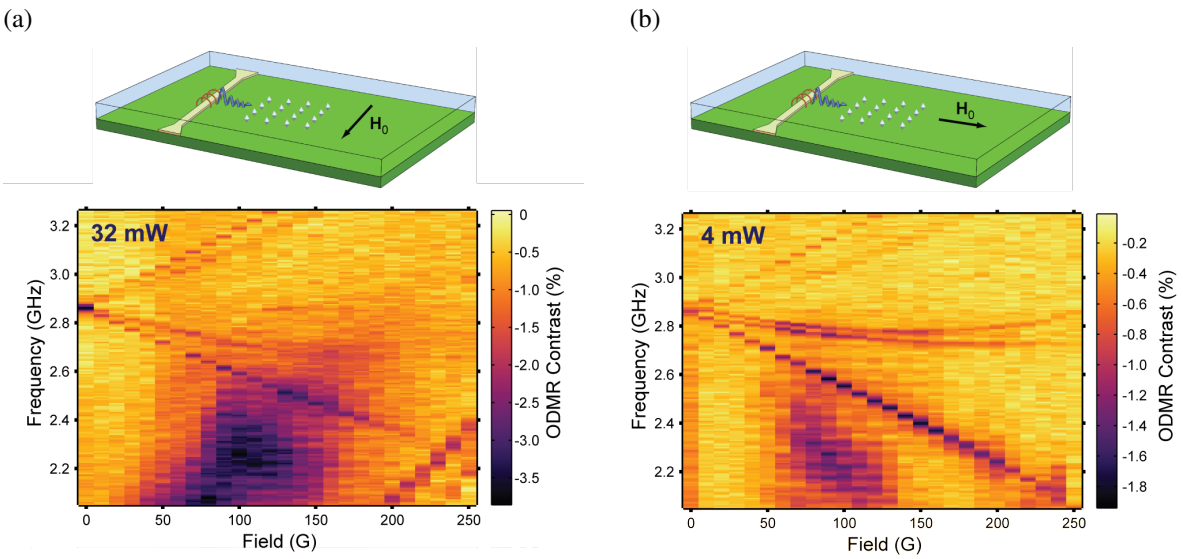

Figure 6.14: (a) ODMR spectra collected for $\theta = \pi$ using 32 mW of microwave power. In this condition, DESW are still excited, but the SW is now confined at the opposite surface of the YIG layer, resulting in the strong reduction in the PL quenching effect. (b) Data obtained for $\theta = \pi/2$ using 4 mW of microwave power. Here, we drive SW modes with sinusoidal profiles across the YIG layer. The absence of a strong surface confinement in the proximity of the NV centers results again in strongly diminished effects on the PL.

relations and magnetization profiles, which allows us to analyze the dependence of the SW-NV interactions on these properties. In Figure 6.14(a) we show the ODMR data collected for the $\theta = \pi$ case using 32 mW of microwave power, which is the minimum power needed to resolve the NV centers resonances at all fields. The strong reduction in the PL quenching with respect to the $\theta = 0$ case can be explained in light of the non-reciprocal nature of the DESW modes[131]. Indeed, as described earlier, a $\theta = \pi$ rotation of the magnetic field results in a decrease of the SWs excitation efficiency[134, 31] and in a drastic change in the SWs amplitude profile, which is confined to the opposite surface of the ferromagnetic layer. In Figure 6.14(b) we present the ODMR spectrum collected using 4 mW of microwave power in the case of $\theta = \pi/2$, when pure BVMSW are excited. The extent to which the PL is affected is again remarkably smaller than for the $\theta = 0$ case. While the excitation efficiency for DESW and BVMSW can be different, this alone cannot explain the two orders of magnitude increase in power required to observe ODMR contrast in the latter case. The difference in the frequencies of the two sets of modes also does not justify the absence of a region of strong PL quenching in the magnetic field range we studied, particularly considering the

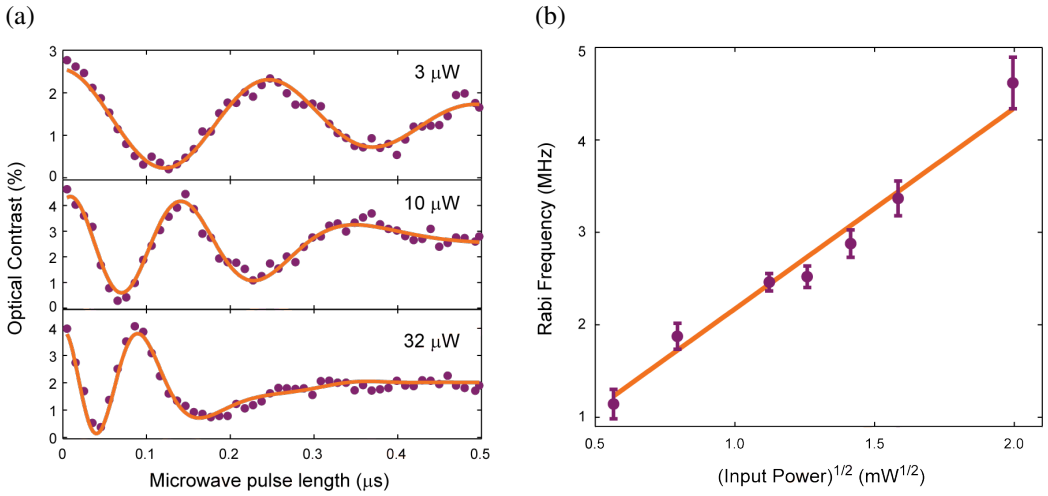

Figure 6.15: (a) Rabi oscillations measured on NP-Q at a fixed external magnetic field (120 G) and different microwave powers. The nanoparticle is located 20 μm away from the driving MSL. (b) Dependence of the Rabi oscillation frequency on the square root of the input microwave power in the spin wave driving regime. These data was collected on particle NP-R located ∼70 μm away from the MSL. The error bars are related to the imprecision in the determination of the Rabi periodicity.

broadband nature of the off-resonant effects. Together, the measurements presented in Figures 6.12 to 6.14 demonstrate the SW mediated nature of the enhanced microwave-NV center interactions and that the surface confinement of DESW is fundamental to this enhancement. We note that these results suggest that tightly confined surface SW modes could provide a promising tool for the study of the spin properties of many nanoscale systems, similar to the way surface plasmons are used to investigate light-matter interactions.

6.5 Spin wave mediated coherent driving of NV centers

We now want to show that the strong resonant quenching of the NV centers PL demonstrated above is the result of a coherent coupling mechanism between propagating SWs and NV centers. We demonstrate this through the observation of coherent Rabi oscillations of the NV centers driven by DESWs (Figure 6.15(a)). The data were collected on an additional nanoparticle (NP-Q) at 120 G and at microwave powers where the antenna microwave field is negligible at the NDs location (spin wave driving regime). The effect of the microwave power on the SW mediated coherent driving is

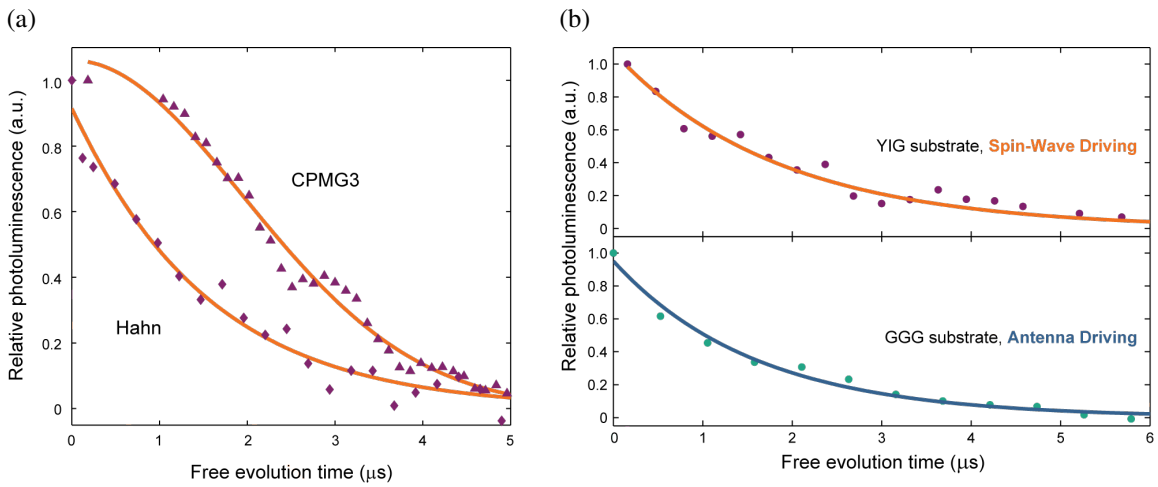

Figure 6.16: (a) Hahn-echo and Carr-Purcell-Meiboom-Gill 3π pulse (CPMG3) measurements that show robust multi-pulse control of the NV centers. Both sets of data are renormalized and fit to $\exp[-(t/T_2)^{\alpha}]$, where α = 1 and 2 for the Hahn and CPMG3 case respectively. From these fits we obtain $T_{2,Hahn}$ = 1.54 µs and $T_{2,CPMG3}$ = 2.78 µs. (b) Hahn-echo measurements on a ND in contact with a YIG substrate (top) and a GGG substrate (bottom). The measurement on YIG is collected using 2 µW of microwave power with the particle ∼30 µm away from the MSL. For the measurement on GGG we use 630 µW and the particle is ∼1 µm from the antenna. An external field of 90 G is applied in both cases.

also shown in Figure 6.15(a). By collecting a series of Rabi curves in the pure spin wave driving regime we can fully investigate the dependence of the NV centers' Rabi oscillation frequency on the input microwave power. The data is presented in Figure 6.15(b) and show a characteristic linear dependence of the Rabi frequency on the squared root of the input power, as expected in conditions where the impact of nonlinear ferromagnetic effects is limited and can therefore be neglected in the interpretation of our results.

We further demonstrate the robustness of the spin wave mediated coherent control using advanced multi-pulse dynamical decoupling protocols that are the basis for many high sensitivity metrology[148, 95, 128, 96] and quantum computing applications[36, 57]. In Figure 6.16 we show the result obtained in the pure SW driving regime for another nanoparticle (NP-R) ∼70 µm away from the MSL using ∼5 µW of microwave power. The ability to extend the coherence time using multi-pulse sequences demonstrates full control of the NV centers through pure SW driving.

We note that, at the microwave power levels required to perform these measurements, the spin

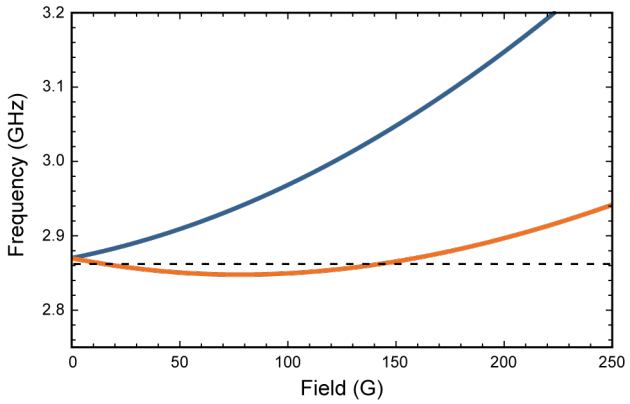

Figure 6.17: Calculated spectrum for the NV center ground state spin transitions for a defect at a 78 degree angle with respect to an external magnetic field. The transition at lower frequency crosses 2.862 GHz (dashed line) both at ∼15 G and ∼145 G.

coherence times are not significantly altered by the presence of the ferromagnet. To demonstrate this we collect Hahn-echo measurements from the same particle positioned first in contact with the YIG substrate and then with a non-magnetic gadolinium gallium garnet (GGG) substrate (Figure 6.16(b)). In both cases an external magnetic field of 90 G is applied. We collect the first measurement in the SW driving regime with the ND ∼30 µm away from the MSL and using 2 µW of microwave power. In the second measurement, the NV centers are manipulated directly by the antenna field, the ND is ∼1 µm from the MSL and we use 630 µW of microwave power. The values of T_2 estimated from fitting the data to exp[-(t/T_2)] are $T_{2,YIG}$ = 1.84 ± 0.36 µs and $T_{2,GGG}$ = 1.60 ± 0.16 µs at 95 % confidence level. These results suggest that the NV centers coherence properties are currently limited by the quality of the host material and not by the proximity to the FM, and can be extended using nanoparticles of higher qualities[2, 152].

6.6 Enhancement of coherent microwave fields

Finally, we estimate the SW induced enhancement of the coherent microwave magnetic field that couples with the NV centers. To do this we compare the Rabi frequencies we obtain at low fields, where the SWs do not appreciably interact with the NV centers (antenna driving regime), with the Rabi frequencies at high fields and low powers (SW driving regime). In order to correctly

estimate the effect of the SW mediated driving we need to factor out the impact of other parameters that influence the SW-NV interaction, such as the frequency dependence of microwave power transmission and the effect of the NV centers' orientation. To do this we take advantage of the dependence of the NV center's ground state spin resonances on the orientation of the external magnetic field with respect to the NV center's axis. Indeed, if we use Equation 2.1 to calculate the frequency of the m_S = 0 to m_S = $\pm$ 1 spin transition as a function of H_0 for the case of an external field oriented at a 78° angle with respect to the NV center axis, we obtain the spectrum in Figure 6.17. In this situation, we observe that the lower branch of the spin transitions crosses the same range of frequencies at fields in the pure antenna driving regime and in the pure SW driving regime.

We estimate that a subset of the NV centers in NP-Q is oriented at $\sim$78° with respect to the external field, therefore we collect the measurements on this ND using a microwave signal at 2.862 GHz (dashed line in Figure 6.17) in both driving regimes, thereby eliminating spurious effects on the calculation of the interaction enhancement. In Figure 6.18(a) we report the data collected at 15 and 145 G when NP-Q is 20 µm away from the MSL, which show that faster driving can be obtained in the SW driving regime using 1 µW of microwave power than in the antenna driving regime using 4 mW. From these measurements we can calculate the SW induced local enhancement of the driving microwave magnetic field Δ_{MW} from

$$\Delta_{MW} = \sqrt{\frac{P_{ant}}{P_{SW}}}\frac{\tau_{ant}}{\tau_{SW}} \tag{6.31}$$

where P_{ant} and P_{SW} are are the microwave powers used to collect the Rabi measurements in the two regimes, and τ_{ant} and τ_{SW} are the respective Rabi oscillation periods. For the data in Figure 6.18(a), this corresponds to a factor of $\sim$100 enhancement. This enhancement factor is a function of the nanoparticle's distance from the MSL as the antenna's field decays as the inverse of the distance while the magnetic field generated by the propagating spin waves is only limited by the YIG's large spin wave decay length[168]. This effect is illustrated in Figure 6.18(b), where we show the behavior of the microwave magnetic field enhancement for NP-Q when we translate the ND from

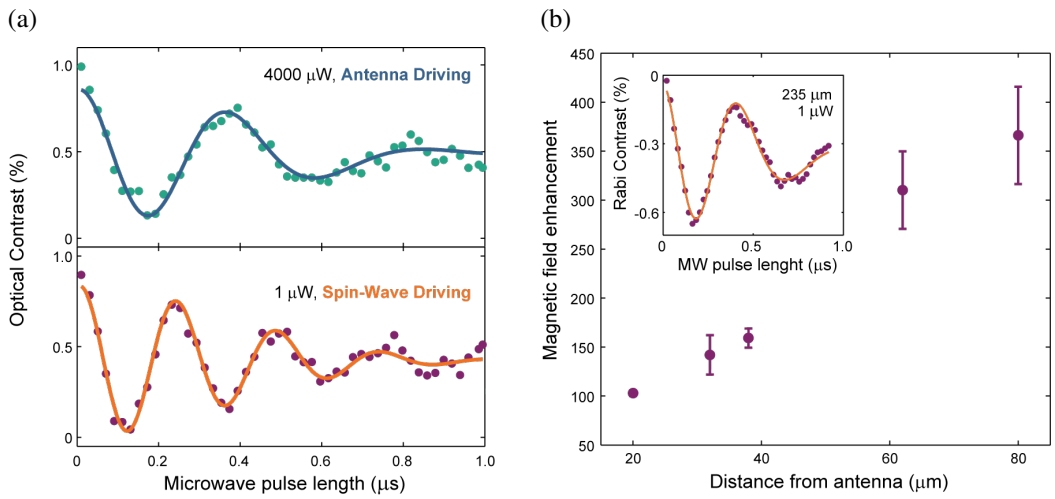

Figure 6.18: (a) Rabi oscillations measured on NP-Q (20 µm away from the MSL) at the same microwave driving frequency (2.862 GHz) but different external magnetic field and microwave power. The top curve is measured in the antenna driving regime at 15 G and using 4 mW of microwave power. The curve at the bottom is collected in the pure SW driving regime at 145 G and using 1 µm of microwave power. (b) Microwave magnetic field enhancement as a function of the NDs distance from the antenna showing the effect of the long SWs damping lengths. The error bars reflect imprecisions in the determination of the Rabi frequencies. In the inset we show the Rabi signal obtained at high fields when the particle is ∼235 µm away from the antenna using 1 µm of microwave (MW) power.

20 to 80 µm away from the MSL. The enhancement increases roughly linearly to >350, which corresponds to five orders of magnitude less power required for the qubit driving and suggests that the SW decay length in this YIG substrate is significantly larger than 80 µm. To illustrate this point and to showcase the long-range nature of the SW-NV centers interaction we demonstrate the possibility of performing Rabi oscillations on a ND ∼235 µm away from the antenna using 1 µW of microwave power (inset of Figure 6.18(b)). This measurement was collected using the pair of MSLs separated by 300 µm to avoid the presence of an antenna along the SW propagation path, which could introduce damping in the propagating SWs. We note that at distances > 80 µm, it becomes impossible to determine the field enhancement factor as we do not observe direct driving induced by the antenna's electromagnetic field due to the limited microwave power available in our experiment.

These results have great significance in the efforts towards achieving enhanced sensing of target spins as they suggest that surface confined SWs can very efficiently amplify the spins microwave

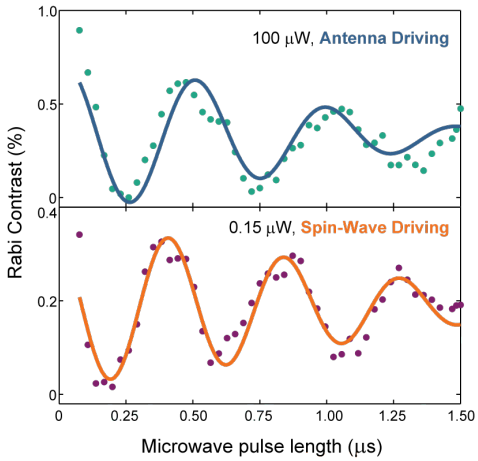

Figure 6.19: Rabi oscillations measured on a nanoparticle ∼100 nm away from the MSL (top) at 10 G and using 100 μW of microwave power at 2.845 GHz and (bottom) at 120 G and using 0.15 μW of microwave power at 2.865 GHz.

signature and transfer this amplified signal unchanged over large distances. Moreover, we note that the uniformity of the SW driving field has important implications for the development of widefield quantum sensing devices, where microwave signals need to be delivered homogeneously across a large array of sensors. In particular, the low power operation described here is suitable to perform sensitive temperature measurements, where microwave heating can interfere with naturally occurring thermal gradients.

6.7 Short distance enhancement

To obtain a better understanding of the potential of our results for applications concerning the detection of single spins, we measure the enhancement factor for a ND positioned in close proximity of a MSL, in particular at a distance where a NV center with long coherence times could be placed with respect to a spin target. This result could help estimate the SW mediated field enhancement for a source with a fast decaying field profile. Indeed, we note that the enhancement factor for a given separation depends on the magnetic field profile of the microwave source. For this reason, sources characterized by faster decaying fields, such as magnetic dipole moments, would benefit even more from the SW induced field amplification.

To select the ND for these measurements, we first position one line of a nanoparticle array close to the antenna and slightly tilted ($\sim$1.5°) with respect to the MSL signal line. The NDs in this line are therefore progressively closer to the antenna until they fully overlap with it. For this measurement, we used a ND array that was patterned using circles with diameters of 100 nm. We collect ODMR measurements on nanoparticles increasingly closer to the antenna until we notice a marked drop in the ODMR contrast for the first ND which resides on top of the metal (and therefore is less sensitive to the ferromagnetic excitations). From the spacing between the NDs and the orientation of the line of nanoparticles, we estimate that the separation between NDs in the direction orthogonal to the antenna is $\sim$100 nm. From this, and allowing for variations in the position of the nanoparticles within the lithographically patterned spot, we calculate that the particle closest to the MSL that shows strong SW-NV centers interactions is $\leq$100 nm from the antenna. Next, we collect Rabi curves on this particle in the antenna driving and SW driving regime. We note that, in this case, we cannot use the same exciting frequency in the low and high field range, nevertheless, these frequencies are within a range in which variations in the microwave transmission are negligible. In Figure 6.19 we show the data collected at 10 G and using 100 μW of power at 2.845 GHz (top) and at 120 G, using 0.15 μW of power at 2.865 GHz (bottom). From these results, we calculate a microwave field enhancement of $\sim 30 \pm 1.6$, which is compatible with the trend presented in Figure 6.18(b) and confirms that surface confined SWs are a promising platform to implement interaction buses to enhance the microwave signal of various spin species and allow their remote detection. To better illustrate this concept, we conclude this chapter by proposing a hybrid device that could be employed to perform these measurements.

6.8 Enhanced spin wave mediated electronic spin sensing

In the device schematically shown in Figure 6.20(a) target spins (e.g. free radicals in a biological molecule) are placed on top of a magnonic cavity that is connected by a SW waveguide to a distant ND. The external magnetic field is applied in the direction that results in strong DESW-NV center interactions and its amplitude is such that the SW cavity mode is resonant with one

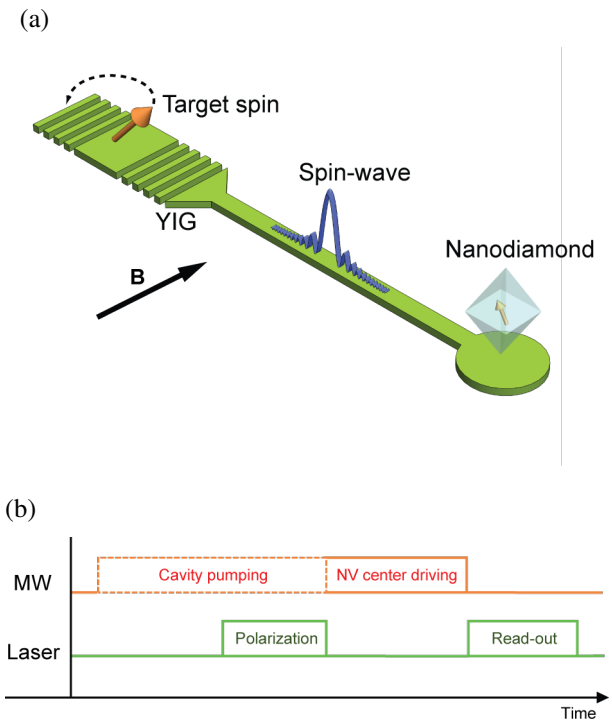

Figure 6.20: (a) Schematic of the proposed sensing device. Target spins are positioned in the proximity of a YIG magnonic nanocavity, which is connected to the location where the nanodiamond is through a SW waveguide. The external magnetic field in applied in the direction that guarantees the excitation of DESWs. (b) Pulse sequence for the detection of electronic spins through indirect coherent driving of a NV center. A microwave signal is used to induce the precession of the target spins at the frequency that matches the cavity mode resonance. The microwave field generated by the precessing spins excites the cavity mode and progressively pump energy in the cavity. A laser excitation pulse is used to initialize the NV center, which is then allowed to interact with spin waves emitted by the cavity. After a set interaction time, an additional laser pulse Is used to read-out the state of the NV center.

of the NV centers transitions, while the target spins Zeeman splitting is at a different frequency. Following the pulse sequence shown in Figure 6.20(b), Rabi oscillations of the target spins are induced using a microwave field resonant with their Zeeman splitting. When the periodicity of these oscillations matches the frequency of the cavity mode, the latter is progressively pumped by the microwave field generated by the precessing target spins, until the rate of SWs leaking from the cavity matches the rate of pumping. The NV centers are then initialized using a laser pulse, before interacting with the SWs leaking out of the cavity for a variable time τ. The state of the NV centers is read out optically with a second laser pulse. This measurement scheme is equivalent to performing SW mediated Rabi driving on the NV centers and contains information on the species

of the target spins through the resonant nature of their driving, and on their concentration through the Rabi oscillations frequency for a fixed pumping time.

To support the validity of this sensing scheme we want to draw a comparison between the experimental results and the case of a single electronic target spin. In particular, we will start by measuring the amount of power carried by the SWs that are involved in the NV centers driving. We will then assume to input this power into an ideal antenna and we will estimate the amplitude of the resulting oscillating magnetic field. Finally, we will compare this result with the oscillating magnetic field of a precessing electron spin. Due to the complexity of this system and the number of parameters that could be modified, we will necessarily need to introduce numerous assumptions as detailed in the following.

To calculate the effective microwave power that is converted into SW excitations, we first collect a microwave transmission measurement between two MSLs separated by 50 µm at zero field. This measurement provides the baseline power that is received by the detecting MSL, which is not related to SW excitations. Specifically, at the frequency of the SW mode used to collect the data in Figure 6.18 (2.862 GHz), the transmitted power is $\sim$10 nW for an input power delivered to the MSL of 0.5 µW. We select this power as it corresponds to a standard level at which we could observe SW mediated driving of the NV centers. We note that in various instances clear effects of SW-NV centers interactions are visible with up to 5 times less microwave power. These variations are attributable to variations in the ND size (which determines the average distance of the NV centers from the YIG surface) and in the exact distance of the nanoparticle from the FM.

When we increase the external field to 145 G (field is oriented in the DESW configuration), the signal related to the SW modes appears in the transmission spectrum. In particular, the transmitted microwave power at 2.862 GHz increases by 1dB in these conditions, which corresponds to an additional power of $\sim$3 nW introduced by the propagating SWs. Assuming a $\sim$5 % coupling efficiency of the SW microwave field with the antenna (projected from the results in Figure 6.8(a)), we can then estimate at $\sim$60 nW the power carried by the relevant SWs. Finally, assuming that the detected power is uniformly distributed along the entire length of the MSL (200 µm), the SW

power per unit length of the YIG is $\sim$300 pW/μm. In these calculations, we are assuming that, as it is well supported by the data in Figure 6.18(b), the SWs magnetization oscillation does not significantly decay over a distance of 50 μm.

We now turn to the case of a sensing device where the SW excitation source is an ideal antenna, which allows us to obtain an estimate of the oscillating magnetic field needed to excite the required SW power. We consider a dissipationless wire antenna with a 50 Ω impedance that runs orthogonally across a 200 nm wide YIG waveguide. The fabrication of such a nanostructure is achievable with current nanofabrication technology[113, 84, 8], but we note that in this discussion we are neglecting the effect of the wavelength of the excited SWs, which can differ depending on the magnetic field profile of the microwave source. We assume that the SW excitation efficiency for the field generated by the antenna is again $\sim$5 %. With these assumptions, an input microwave power of 1.2 nW would provide a total SW power of 300 pW/μm in the YIG waveguide.

We can now calculate the amplitude $\bar{I}$ of the oscillating current in the antenna from:

$$\bar{I} = \sqrt{2}\sqrt{\frac{P}{Z}} \sim 7pA \tag{6.32}$$

where P is the input power and Z is the antennas impedance. This oscillating current in turn produces an oscillating magnetic field of amplitude:

$$\bar{B} \sim \frac{\mu_0 \bar{I}}{2\pi r} \tag{6.33}$$

where μ_0 is the vacuum permeability and r is the distance from the center of the antenna. For the purpose of obtaining an estimate that can be compared with the case of a single electron positioned within few nanometers from the YIG surface, we now assume that the wire antenna has infinitesimal width. The magnetic field amplitude 5 nm away from the antenna is then $\sim 2.8 \times 10^4$ T.

We continue by estimating the amplitude of the oscillating magnetic field of a single electron spin precessing in a plane orthogonal to the ferromagnetic layer. The electron spin is initially oriented along the external magnetic field, which is applied in the DESW configuration, and a

microwave driving field is then used to induce precessions with a frequency that matches the SW resonance frequency. We calculate the static magnetic field of the electron spin using:

$$\boldsymbol{B} = \frac{\mu_0}{4\pi}\left(\frac{3\boldsymbol{r}(\boldsymbol{r}\cdot\boldsymbol{m})}{r^5} - \frac{\boldsymbol{m}}{r^3}\right) \tag{6.34}$$

where $\boldsymbol{r}$ is the displacement from the spin placed at the origin and $\boldsymbol{m}$ is the spin magnetic dipole moment. We then use the values of this field in the direction parallel and orthogonal to the dipole axis to estimate the oscillating magnetic field amplitude and obtain:

$$\bar{B} = \frac{\mu_0\mu_B}{8\pi r^3} \sim 3.7 \times 10^{-6}\,\mathrm{T}, \tag{6.35}$$

which is within 2 orders of magnitude of the field calculated above for the ideal antenna. We stress that, due to the complexity of the system that we are considering, a more detailed analysis and careful simulations of the device are required in order to obtain more quantitative results. Nevertheless, because we attempted to be conservative in the estimates introduced in the presented calculation, the results suggest that spin wave pumping using precessing target electronic spins for the purpose of obtaining enhanced, long-range sensing could be within the reach of the hybrid architecture that we developed. We note that, for these applications, the use of engineered NDs containing single NV centers at well defined distances from the nanoparticle interface, could play a large role in reducing the amount of SW power needed for the NV center manipulation. Additionally, in the calculation we have not considered the effect of the coupling of the precessing spin with a magnon cavity mode, which could introduce a further enhancement in the amplitude of the magnetic field in the YIG, to be balanced with the SW leakage from the cavity.

To conclude, in this work we used a hybrid YIG-ND quantum system to investigate the interactions between surface confined DESWs excited by a MSL and NV centers, and demonstrate the presence of a room temperature regime in which coherent coupling mechanisms can exceed the effects of incoherent interactions. This SW mediated coherent control persists at distances of more than 200 µm and is used to implement dynamical decoupling schemes on the NV centers

spins. Additionally, we show that DESWs can locally enhance the microwave magnetic field interacting with the NV centers by more than two orders of magnitude, which considerably lowers the amount of power needed for coherent control. These results suggest, for instance, that surface confined SWs offer a promising avenue to improve the NV centers sensitivity through the enhancement of the coherent coupling to distant spins. Additionally, the strong, local microwave magnetic field enhancement obtained with DESWs could be of great interest to study the properties of spin systems at the nanoscale. Finally, the observation of a uniform, efficiently driven SW microwave field over at least tens of micrometers is significant for the implementation of wide-field thermometry devices. We note that we achieve these results using inexpensive, commercially available nanoparticles, which makes our system highly scalable. Nonetheless, as mentioned in the previous chapter, combining the techniques described in Chapter 4 and Chapter 5 we can create array of engineered NDs with controllable NV center density, position, and orientation, as well as much improved coherence times[2], which could help furthering the understanding of the SW-NV centers interactions.

CONCLUSIONS

In this thesis we analyzed the ongoing challenges to using nanodiamonds (NDs) as nanoscale temperature and magnetic field sensors, and introduced various approaches aimed at tackling these limitations and extending their capabilities.

Firstly, we addressed the intrinsically poor coherence properties of NV centers in currently available diamond nanoparticles by developing a microfabrication technique for the creation of NDs with highly controlled geometry, crystal quality and NV centers' density and positioning. These properties are not only reflected into a higher achievable sensitivity, but also enable the stable, contactless control of the nanoparticles in solution by means of an optical trapping apparatus. This result paves the way to the implementation of advanced dynamical decoupling techniques on nanoparticles in fluidic environments, which could have a great impact, for instance, for the *in vivo* investigation of biological systems at a subcellular scale.

In order to scale up the use of diamond nanosensors, a platform that allows for their placement on a wide variety of systems and materials is also required. Here, we establish a process to fabricate millimeter sized arrays of NDs with variable pitches and particle density and that are embedded within a flexible and transparent silicone film. This structure can be easily placed on a substrate of interest and we demonstrate its capabilities for thermal mapping application by imaging the temperature distribution of a coplanar waveguide antenna. The results showcase the potential for these systems to become widely adopted, reusable sensors for the study of microelectronics and magnetic systems. In particular, they could have a great impact in the study of caloritronics and spin caloritronics devices, where the accurate knowledge of the temperature gradients in the system is crucial to understand its properties and optimize its efficiency.

While with the development of high quality engineered nanodiamonds we aimed at improving the intrinsic sensitivity of the NV centers, another approach towards pushing quantum sensing towards smaller and smaller numbers of detected spins, relies on amplifying the signal to be measured. This is the concept that we investigated in the last chapter, where we showed that spin waves in a ferromagnetic material can mediate coherent interactions between NV centers in nan-

odiamonds and a microwave source. Thanks to their low-damping properties, the spin waves can counteract the natural field decay of the microwave source, effectively amplifying its signature at the location of the NV centers. This achievement could also be exploited to relax the requirements on the positioning of the sensing qubits with respect to the diamond surface, thereby improving their coherence properties and their potential for the development of quantum computation schemes.

As we have previously mentioned, combining the techniques that we presented even further improvements could be achieved. For instance, embedding in a PDMS matrix engineered nanoparticles containing single NV centers would dramatically extend the capabilities of these flexible systems, both as two-dimensional sensing platforms and as building blocks for hybrid systems for quantum computing applications. Numerous advancements can also be introduced moving towards a second generation of hybrid devices. In particular, patterning magnonic waveguides and cavities in the ferromagnetic material will be critical to pushing the sensitivity of these architectures to few spins. Additionally, it will be of great interest to extend the measurements to cryogenic temperatures, where NV centers entanglement schemes based on the exchange of virtual magnons can be studied.

Our hope is that this thesis provides an important contribution in the development of the field of nanoscale sensing with nanodiamonds, establishing new techniques and concepts that could advance our ability to "manipulate and control things on a small scale", as it was to be in Feynman's vision.

Appendices

APPENDIX A

ENGINEERED NANODIAMONDS FABRICATION DETAILS

In this appendix we present the details of some of the fabrication steps used to obtain the engineered diamond nanoparticles that were omitted in the main text. These processes were developed at Nanotech, the nanofabrication facility at the University of California, Santa Barbara.

A.1 Recipe for diamond membrane bonding

In chapter 4 we described the process used to obtain engineered diamond nanoparticles by processing thin diamond membranes bonded onto a silicon carrier wafer. Here, we report the steps used to prepare a bonded membrane starting from the situation where it has been released from the bulk diamond substrate and transferred into a vial filled with deionized (DI) water (see section 4.1.2).

1. Using a micro-pipette transfer the membrane from the DI water solution into a vial containing isopropyl alcohol (IPA). To help with this process, we remove the top $\sim$2 mm of the pipette tip to obtain a larger opening that allows us to capture the membrane.

2. With a new pipette tip collect 2 µL of the new solution including the membrane and drop cast it on a polytetrafluoroethylene (PTFE) substrate. To do this, we first let the membrane float towards the bottom of the pipette tip to minimize the amount of deposited liquid. By virtue of its low surface tension, IPA quickly spreads across the substrate creating a thin solvent layer, which limits the tumbling dynamics of the membrane.

3. Ensure that the membrane is deposited in the correct orientation. The membrane will have to be bonded to the silicon substrate with the damaged layer facing up to allow for its removal. To identify the orientation, markers are created in the diamond during the etch step used to define the membrane mesas into the bulk material. In particular, we create triangular patterns with different orientations at three of the membrane corners (Figure A.1(a)). When the tips of the triangles point counter-clockwise the damaged layer is at the bottom surface of the

membrane, which is the necessary condition at this phase of the process. If the orientation of the membrane is not correct add a drop of IPA to float it again and promote moderate rotation. Another possible approach to follow in the case the membrane orientation is not correct is to flip the PTFE carrier onto another one to transfer the membrane upside-down. Nevertheless, this technique has proven difficult as the membrane is not consistently removed from the initial substrate.

4. Let the IPA slowly dry by placing the PTFE on a hot plate at 50 °C. If the evaporation of the IPA happens to rapidly it can dislodge the membrane from the substrate.

5. Cleave a silicon carrier substrate slightly larger than the PTFE carrier and clean it sequentially with acetone and IPA for 3 minutes each in an ultrasonic bath. Note that, if the membrane is to be used for the fabrication of diamond nanoparticles, the silicon carrier also needs to fit in the vial that will be used to obtain the ND solution.

6. Spin coat the silicon carrier with electron-beam resist 950 PMMA A4 (MicroChem Corp.) using the following recipe:

   - 5 s, 500 rpm, 500 rpm/s.
   - 10 s, 2500 rpm, 1000 rpm/s.

7. As soon as the spin coating recipe is completed rapidly position the silicon carrier on top of the PTFE substrate, with the photoresist layer in contact with the membrane. This step needs to happen quickly to minimize the evaporation of the resist solvent before it gets in contact with the membrane. Apply pressure on the silicon carrier using a cotton swab.

8. Position silicon,diamond membrane, and PTFE (with this latter layer on top) on a hot plate at 95 °C for three minutes. Place a magnet on top of the PTFE to apply a constant pressure during the solvent evaporation and consequent bonding. The magnet is attracted by the underlying metal hotplate. Particular attention needs to be used when first placing the magnet

(a) (b)

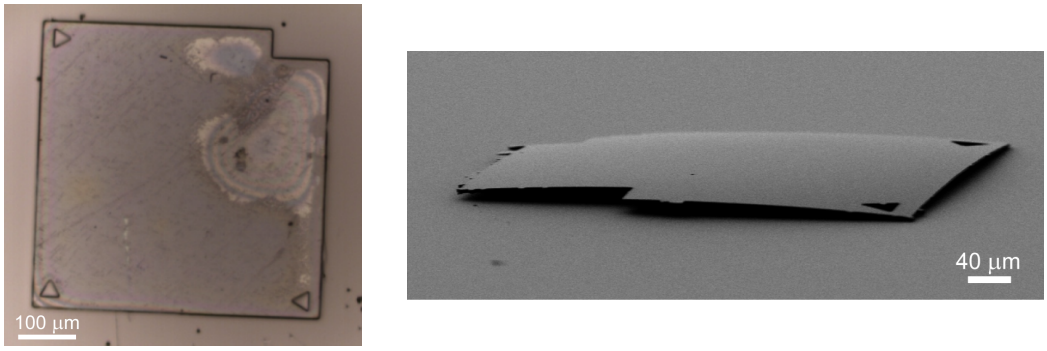

Figure A.1: (a) Optical image of a diamond membrane bonded on a silicon carrier wafer. Visible are the triangular regions etched to identify the orientation of the membrane. The ring-like patterns on the left side are due to thickness variations in the resist located underneath the membrane. (b) Scanning electron microscopy image of a bonded membrane showing the effect of strain, which tends to bend the material reducing its adhesion to the substrate.

to avoid moving the PTFE with respect to the underlying silicon carrier as this would result in a less efficient bond.

9. Increase the temperature of the hotplate to 185 °C to bring the resist above its glass transition to create a soft adhesive layer for the membrane. Bake at this temperature for 10 minutes.

10. Remove the magnet and the sample from the hotplate and let it cool down.

11. Remove the PTFE layer.

Note that the procedure reported here is partially different from the one used by the Hu's group at Harvard. In particular, we used PTFE for the transfer rather than a silicon carrier to minimize the adhesion of the membrane to this temporary substrate. We also immediately place the sample on the hot plate after silicon and PTFE are sandwiched together to promote the rapid evaporation of the photoresist solvant. Another possible approach is to first use a vice to strongly compress the two layers and favor the achievement of a uniform bond. This can be particularly important for membranes that show a high level of strain as they tend to curl during the bonding process resulting in poor adhesion to the substrate (Figure A.1(b)).

A.2 Recipe for hydrogen silsesquioxane spin coating

The following is the recipe used to spin coat the HSQ:MIBK 1:1 resist on the diamond membrane. As we mentioned in the main text, once exposed the resist becomes an amorphous silicon dioxide hard mask.

- Remove the bottle of HSQ:MIBK 1:1 resist from the fridge 5 minutes before spinning.
- Spin coat for 30 s at 4000 rpm, 800 rpm/s.
- Bake for 2 minutes at 95 °C.
- Slowly flow nitrogen into the resist bottle before storing it in the fridge to remove traces of water vapor, which would degrade the resist's quality.

This recipe results in a mask $\sim$ 200 nm thick.

A.3 Dry etch recipes

Here we list the details of the dry etch recipes used in the fabrication of the diamond nanopillars. All the etches are performed using a Panasonic E640 ICP-RIE tool.

A.3.1 Diamond thinning recipe

We use this etch recipe to remove the damaged layer from a membrane bonded on the silicon substrate, or to thin down the material to a required thickness. This etch guarantees the achievement of a smooth and uniform surface and provides an etch rate of 3 µm/h.

- Argon flow: 25 sccm.
- Chlorine flow: 50 sccm.
- Chamber pressure: 0.7 Pa.

- Radiofrequency source power: 500 W.

- Bias power: 200 W.

A.3.2 Chromium etch recipe

After developing the HSQ mask we remove the chromium adhesion layer from the regions where the diamond membrane is exposed using the following recipe:

- Oxygen flow: 40 sccm.

- Chlorine flow: 25 sccm.

- Chamber pressure: 0.7 Pa.

- Radiofrequency source power: 500 W.

- Bias power: 15 W.

which results in an etch rate of 3 Å/s. We note that this etch step is not strictly necessary as the diamond etch described below would also quickly remove the thin chromium layer.

A.3.3 Diamond etch recipe

This is the recipe that we use to transfer the hard silicon dioxide mask into the diamond membrane. The following parameters guarantee an etch rate of 150 nm/min:

- Oxygen flow: 30 sccm.

- Chamber pressure: 1.33 Pa.

- Radiofrequency source power: 700 W.

- Bias power: 200 W.

A.4 Preparation of the nanodiamond solution

For most of the measurements performed on the engineered diamond nanoparticles we create a ND solution by simply inserting the silicon substrate with the patterned membrane in a polypropylene (PP) vial containing acetone, and placing the vials in a ultrasonic bath for 10 min. We then remove the silicon substrate from the vial and use a centrifuge to precipitate the NDs at the bottom of the container. The acetone at the top of the vial is subsequently removed and replaced with DI water. We repeat the centrifugation process 3 to 5 times to remove as much acetone as possible and create a solution of NDs in water. Finally, we flow the solution through a filter with 2 µm pores to remove particulates and impurities originating from the silicon substrate.

We also developed a different process to obtain the ND solution for the situations where it is critical to remove all the impurities from the fluid.

1. **Oxide mask removal**

   When we complete the etch of the diamond membrane, the nanoparticles are still capped by part of the oxide layer used as a hard mask for the etch. To remove the HSQ in excess we place the silicon carrier into a PTFE container and deposit a $\sim$10 µL droplet of buffer oxide etch (BOE) on top of the region where the patterned membrane is. We cover the sample with a PTFE beaker and we let the BOE act for 10 min, during which it will also etch the PMMA resist. The etch rate for SiO_2 varies between 100 and 600 nm/min.

2. **Removal of silicon particulate**

   We transfer the silicon carrier, together with the HF drop into a PP vial containing 1.5 mL of Potassium Hydroxide (KOH) 45 % wt. in H_2O (we want to use an amount of KOH which allows for the neutralization of the BOE). The etch rate of silicon for this solution is $\sim$1.1 µm/min. We place the vial in an ultrasonic bath for 10 min. We then remove the silicon carrier from the vial and continue to sonicate for another 10 min.

3. **Nanoparticle filtering 1**

   We set up a vacuum filtration system (Fisher Scientific) to separate the nanoparticle from

the KOH. This system is composed of a 250 mL pyrex filtering flask connected to the house vacuum nozzle, a Whatman PTFE membrane filter with 0.2 µm pores placed on top of the flask, and a 15 mL open graduated cylinder clamped on top of the filter. We pour the nanodiamond solution in the graduate cylinder together with some DI water ($\sim$10 mL) and we let it percolate through the filter while the nanodiamonds get trapped in it. We note that the flow of the solution through the filtering system is strongly dependent on the degree to which the connections between the different piece of glassware are accurately sealed. To check for the presence of leaks spray some DI water at the locations of the connections between the various elements.

4. **Acid Cleaning**

   We proceed to use a standard acid cleaning treatment[91] to remove the amorphous carbon at the surface of the nanodiamonds and oxygen terminate the surface bonds. The PTFE filter is placed in a pyrex flask containing a magnetic stirrer in which we pour a mixture of nitric and sulfuric acid (H_2SO_4:H_2NO_3, 3:1). A Liebig condenser tube is clamped on top of the flask and water is flown through it to avoid the dispersion of acid fumes. The apparatus is held by a support stand inside an ultrasonic bath for 10 min to allow for the nanoparticles to be released from the filter. We note that a possible alternative to the PTFE filters would be to use polyethylene filters. These are not attacked by KOH but would be dissolved in the acid mixture releasing the particles. This approach could result in a better outcome as the filters we used are partially affected by the acid when left in it for a long time and might release fibers in the solution.

   We pour some mineral oil in a pyrex beaker that we place on a hot plate at 90 °C. We use this as a bath to heat the acids as the oil does not significantly evaporate at this temperature. With the help of the support stand we dip the acid cleaning apparatus inside the oil bath and activate the magnetic stirring at 200 rpm. We let this process continue for 16 hours.

5. **Nanoparticle filtering 2**

We allow the acid solution to cool down before detaching the condenser unit. We then pour the solution in the same filtration system used earlier with a new PTFE filter inserted between the flask and the graduated cylinder. At regular time we add DI water to improve the flow of the solution through the filter.

6. **Final water solution**

   Finally we cut out the part of the filter that was exposed to the acid flow and place it in a glass vial containing DI water. The amount of water that is used determines the density of the nanoparticles in solution. In particular we use 6 mL, which results in a low density solution. We place the glass vial in an ultrasonic bath for 10 min and then remove the filter.

We note that at each step of this process a certain amount of nanoparticles is invariably lost. As the efficiency with which the NDs are transferred through the various steps is not fully characterized we suggest using the simpler process described at the beginning of this section unless the purity of the solution is crucial.

APPENDIX B

FABRICATION OF THE MICROFLUIDIC CIRCUITS

The development of the microfliudic circuits follows these steps:

- Design of the circuits and creation of a photolithography mask.
- Fabrication of the circuit mold.
- Imprinting of the mold into a PDMS layer.
- PDMS circuit bonding on the desired substrate.

In the following we detail each of these steps.

B.1 Microfluidic circuit design and mask fabrication

To fabricate the microfluidic circuits we first use a lithographic process to create a mold that can be employed to serially produce the devices .

We start by creating a photolithography mask that corresponds to the positive image of the required circuits (exposed areas will correspond to the channels). As the minimum resolution needed in for our experiments is at most 10 µm, we elect to use photomasks printed on an optically transparent flexible substrate obtained from CAD/Art Services, Inc.. As the turnaround time to obtain these masks is much faster than for patterned metal masks, this also allows us to quickly experiment with multiple circuit designs. We first use a CAD software to prepare a dwg file with the circuit geometry following some basic design rules:

- The minimum feature size guaranteed by the photomask company is 10 µm.
- The microfluidic channels that we create have roughly a rectangular cross section. For this type of channel it is recommended not to exceed an aspect ratio (height of the channel:width of the channel) of 1:8 (for simple single layer devices). Beyond this limit the structures tend to collapse. If wider channels are required it is crucial to add support posts in the design.

- The hydrodynamic resistance of the microfluidic channels strongly depends on their features size. In particular, for a rectangular channel we have[14]:

$$R_{hyd} = \frac{12\eta L}{wh^3(1 - 0.63(h/w))} \tag{B.1}$$

where η is the viscosity of the fluid and L, h, and w are the length, height, and width of the channel respectively. In analogy with the current in an electric circuit, the flow rate Q in the channel is:

$$Q = \frac{\Delta p}{R_{hyd}} \tag{B.2}$$

where Δp is the pressure drop applied across the channel. It is therefore clear that the resistance of the microfludic channels needs to be carefully considered to assess the achievable flow rate given the available pressure gradient. It is also important to observe that the maximum value for Δp can be limited by the structural integrity of the microfluidic circuit. An excessive pressure across the channels can indeed affect the seals in the system.

- To ensure the presence of good adhesion between the PDMS and the substrate we usually do not place parallel channel closer to each other than $\sim$100 µm. This provides an efficient seal surface between the channels.

- The photomask company processes the CAD file by reversing the polarity (printed/non-printed areas) of the image at each closed boundary, starting with a non-printed area at the edges of the mask.

We usually replicate the circuit design enough time to cover a 5 by 7 inch area, which is the minimum mask size offered by the company. Once the mask design is ready we submit the dwg file, which is rendered into a pdf file with black and white features as they should appear on the mask. We commonly used the following printing options:

(a)

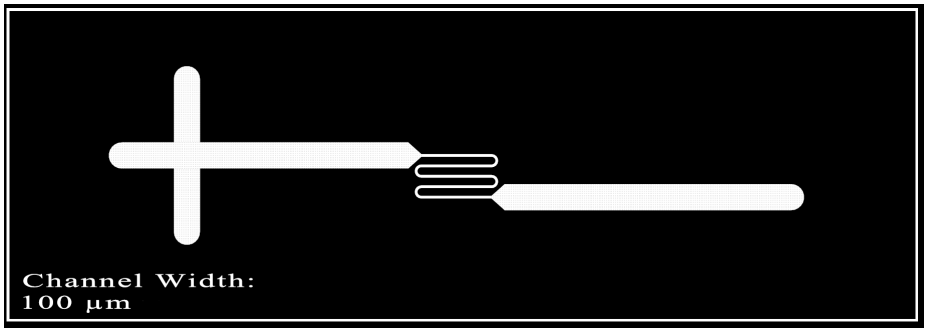

(b)

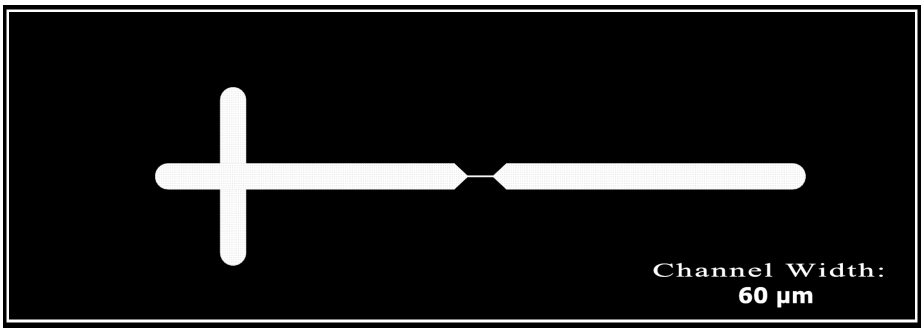

Figure B.1: Design of alternative microfluidic circuits. (a) Circuit with a winding narrow channel at the location where the circuit is in the proximity of the microwave antenna. The shape of the channel enables the presence of multiple regions where we can optically trap the NDs in the presence of a strong microwave signal. (b) Circuit with only a short narrow region to reduce the total impedance of the circuit. Both options are designed to have up to three inputs at the extremities of the cross-like region and one output at the opposite side of the circuit. The channels' width reported on the designs refers to the narrower region of the circuit. The wider channels contain circular structures (not visible at the magnification used here) that will result in the support pillars for the circuit.

- Spatial printing density of 25400 DPI, which is the highest density provided. This guarantees the best contrast and resolution in the resulting mask.

- Emulsion side down. This refers to the surface of the transparent printing substrate where the ink is deposited. More precisely, if when looking at the mask we see the features with the same orientation they have on the CAD design, the ink is on the bottom surface of the transparent layer. This information is crucial as the printed surface needs to be in contact with the substrate during the photolithography exposure step. This allows for the best feature resolution and prevent the base material (a porous gelatin) to be imaged onto the substrate.

In Figure B.1, we show designs (in addition to the one presented in the main text) that we considered and tested. The circuit in Figure B.1(a) has a longer winding narrow channel. This was designed to provide multiple areas where the NDs could be trapped in proximity of the microwave antenna, which is useful since often parts of the microfluidic circuit can become unusable as a result of the accumulation of nanoparticles or other impurities present in the solution. Additionally, the antenna itself could have damaged regions that do not guarantee an optimal microwave delivery.

In Figure B.1(b) we display a circuit that was designed to minimize its hydrodynamic resistance by making the narrow region of the circuit as short as possible, while still retaining the presence of regions with laminar flow. The small resistance allows for a quicker testing of the nanoparticle solution. We note that having a narrow region is critical as it forces the nanoparticles to flow close to the optical trapping region.

Ultimately, most of the measurements are performed using circuits obtained with the design in Figure 4.11(a) which guarantees a small impedance, while at the same time providing multiple devices on the same chip. This is important as occasionally some of the circuits can collapse during the fabrication process, or become clogged to the point of not being usable.

B.2 Preparation of the mold

The mold for the microfluidic circuits is fabricated by patterning a layer of photoresist on the surface of a silicon substrate, and its thickness is controlled by varying the lithography parameters. We also used two different photoresists to access two different ranges of thicknesses as detailed in the following recipe.

To start we need to prepare the substrate for the mold.

1. **Substrate cleaning**

   This is a very important step as it greatly affects the adhesion of the photoresist on the substrate.

   - Dip silicon wafer in a Nano-strip mixture for 10 min to remove all organic residues.

- Rinse in DI water.
- Dehydrate on a hot plate at 200 °C for 5 min.

2. **Spin coat SU-8 2000.5**

   We use this as a thin adhesion layer for the patterned mold. We spin the resist with:

   - 10 s, 500 rpm, 100 rpm/s.
   - 30 s, 3000 rpm, 300 rpm/s.

   This results in a photoresist thickness of $\sim$0.5 µm.

3. **Soft bake**

   On a hot plate:

   - 2 min at 65 °C. This step is very important as it allows the bubbles in the photoresist to escape.
   - Increase the temperature to 95 °C and bake for 5 min.
   - Decrease the temperature to 30 °C and let the sample cool down.

4. **Flood exposure**

   We flood expose the substrate using a mask aligner (SUSS MA-6) for 10 s. The lamp provides a 17.2 mW/m^2 light intensity.

5. **Post exposure bake**

   Bake on a hot plate at 95 °C for 3 min.

6. **Development**

   - Develop in SU-8 developer for 2 min.
   - Rinse in IPA for 20 s.
   - Dehydrate on a hot plate at 200 °C for 10 min.

The step that follows differ slightly depending on the photoresist that we use. We use SU-8 2015 and SU-8 2075 to create the mold for microfluidic channels with thickness between 15 and 35 µm, and 60 and 80 µm respectively. SU-8 2075 needs to be handled with particular care because it tends to trap air bubbles due to its viscosity. In the following we detail the recipe used to obtain 80 µm tall features. The parameters to be used for other thicknesses can be inferred starting from the one presented here and referring to the SU-8 data sheet (MicroChem Corp.).

1. **Photoresist spinning**

    a) Place the silicon substrate on a hot plate covered with aluminum foil at 35 °C.

    b) Pour the SU-8 onto the substrate directly from the bottle. The use of pipettes tend to introduce air bubbles in the photoresist. Keep the bottle as close as possible to the substrate while pouring to minimize the introduction of air bubbles.

    c) Let the air bubbles that are present escape from the photoresist. Remaining bubbles can be manually burst.

    d) Transfer the wafer to the spin coater. Use the spinning recipe:

        - 10 s, 700 rpm, 200 rpm/s.
        - 30 s, 3000 rpm, 300 rpm/s.

2. **Soft bake**

    On a hot plate:

    - 50 °C for 2 min.
    - Ramp the temperature up to 65 °C and bake for 3 min.
    - Ramp the temperature up to 95 °C and bake for 9 min.
    - Ramp temperature down to 30 °C and let the sample cool.

3. **Exposure**

    We attach the lithography mask to a blank quartz window using tape. It is important that the

tape resides outside the region where the mask comes in contact with the sample to ensure the minimum possible separation. Considering the intensity of the mask aligner lamp and the recipe suggested in the resist data sheet we would need to use a 12.5 s exposure time. This resulted in the underexposure of the photoresist likely due to the fact that we are combining the glass mask with the plastic film mask. We adjusted the exposure time to 15.5 s.

4. **Post exposure bake**

   This step is very important to allow the exposed region to harden.

   - 65 °C for 3 min.
   - 95 °C for 10 min.

   Note that after 1 min at 95 °C an image of the mask should be visible in the resist. The absence of this image is an indication of insufficient exposure, heating or both.

4. **Development**

   9 minutes in SU-8 developer. Transfer the sample in a second beaker halfway through the process to work with a fresh developer. The length of this step varies by few minutes depending on the exact exposure and baking conditions. It is required at times to inspect the sample and continue with further development until the SU-8 is fully removed from the unexposed areas. When development is complete thoroughly rinse the sample in IPA.

5. **Hard bake**

   A final hard bake helps guaranteeing the stability of the mold during thermal cycles. Indeed, because SU-8 2000 is a thermal resin, its characteristic can change when exposed to temperatures higher than the ones encountered during fabrication. For this reason we bake the mold for 10 min at 155 °C.

B.3 PDMS imprinting

Once the mold is ready we proceed with imprinting it within a PDMS matrix. The following recipe provides a 5 mm thick PDMS layer using a 4 inch diameter mold. We used a 3D printed wafer holder with a 4 inch diameter, 7 mm deep recessed area where we can place the mold during casting and hardening of the PDMS.

1. Mix 40 g of PDMS base (RTV615A 01G, Momentive Performance Materials) with 4 grams of cross linking agent (RTV615B 01G, Momentive Performance Materials) in a plastic cup.

2. Place the cup in a Nalgene vacuum dessicator. Rough pump for 30 min, then close the dessicator valve and turn off the pump. Leave the sample under vacuum for 1 h.

3. Cover a hot plate with a piece of aluminum foil and place the wafer holder with the mold in it on top. Pour the PDMS mixture on the mold and let it settle. If air bubbles are present in the PDMS allow them to raise to the surface or burst them.

4. Bake at 110 °C for 1 h.

5. Let the PDMS cool down for 30 min. Removing the PDMS from the mold when it is still hot can cause tearing in the PDMS especially when we use tall features.

6. Peal the PDMS out of the wafer holder, use a razor blade to cut out the microfluidic circuits, and a clean biopsy punch to make holes for the circuit's ports. The diameter of the holes needs to be $\sim$0.3 mm smaller than the outer diameter of the tubing used to deliver the solution to the circuit.

B.4 Bonding of the PDMS on a substrate

Finally, we bond the PDMS circuit to a substrate, which acts as the floor of the microfluidic channels.

1. Place the PDMS circuit in a beaker with DI water in an ultrasonic bath for 10 min to remove all the PDMS debris created while punching the holes. It is preferable not to use IPA for this cleaning step as the PDMS adsorbs the solvent and swells. Blow dry the PDMS when the cleaning terminates.

2. Clean the substrate with acetone and IPA. Dehydrate on a hot plate.

3. To prime the interfaces for the bonding we treat both the substrate and the PDMS sample in a ultra-violet ozone reactor (PR-100, UVP) for 900 s. This process fully oxidizes the interfaces, creating in particular siloxane groups at the PDMS surface, which are conducive of a strong bond.

4. Position the PDMS circuit on the substrate with the activated surface at the bottom and gently press to obtain a uniform contact.

5. Bake on a hot plate at 110 °C for 10 min.

6. Continue the baking in a convection oven at 140 °C for 1 h.

In the measurements that we presented in the main text (see Section 4.5), the substrate was a glass slide on top of which we patterned a coplanar waveguide antenna that we used to obtain the microwave control of the NV centers. We note that the finite thickness of the antenna introduces areas (at the edges of the metallic regions) where the PDMS is not in perfect contact with the substrate, which can introduce spurious flow paths in the system. It is therefore important that the thickness of the features patterned on the substrate only results in high impedance alternative paths for the fluid. Additionally, PDMS does not adhere well to gold because of the absence of an oxide layer. To improve the bonding of the circuits in the metal regions we use a three layer metal structure for the antennas, capping the usual Ti/Au layers with an additional 10 nm layer of titanium.

APPENDIX C

FABRICATION OF THE MICROWAVE ANTENNAS

Here we describe the process developed in the Searle cleanroom and nanofabrication facility at the University of Chicago, which was used to fabricate the microstrip line (MSL) and coplanar waveguide (CPW) antennas on YIG and GGG. We note that in the measurements presented in the main text the antennas are positioned underneath the PDMS layer but they still need to provide access to wire bonding pads outside the PDMS area. For this reason the electrical leads need to be $>$1 mm long. To avoid creating an excessive electrical impedance, even in the case ot the MSLs the leads are surrounded by two ground planes in a CPW configuration that guarantees a good impedance match condition (see Figure C.1). The smallest feature of these antennas are the signal and ground lines at the location where they are horizontally oriented. We patterned metal lines with widths ranging between 5 µm and 6.5 µm and separated by 3 µm to 5 µm. Nevertheless, we use electron beam lithography to pattern the antennas as it allows us to experiment with the design without needing different photolithography masks.

1. **Substrate cleaning**

   We use a standard solvent cleaning process in ultrasonic bath to prepare the substrate:

   - Toluene for 3 min.
   - Acetone for 3 min.
   - Methanol for 3 min.
   - IPA for 3 min.

   Finally we dehydrate the substrate on a hot plate for 5 min at 100 °C.

2. **Bilayer resist preparation**

   We use a bilayer resist process to allow for a thicker metal deposition.

   a) Spin coat PMMA copolymer resist EL11 (11% in ethyl lactate, MicroChem Corp.)

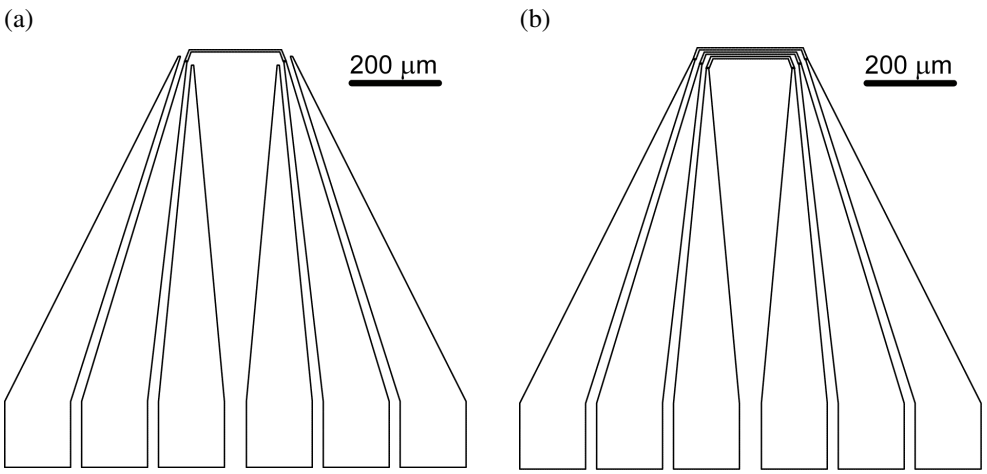

Figure C.1: Geometry of the microstrip line and coplanar waveguide antennas. The design was obtained using DesignCAD LT and fed to the Nanometer Pattern Generation System (NPGS) to control the electron beam of the SEM during exposure.

- 5 s, 500 rpm, 500 rpm/s.
- 45 s, 2750 rpm, 1000 rpm/s.
- Bake 90 s at 150 °C.

This recipe results in a resist thickness of ∼550 nm.

b) Spin coat 950PMMA A4, positive resist (4% in anisole, MicroChem Corp.)

- 5 s, 500 rpm, 500 rpm/s.
- 45 s, 3000 rpm, 1000 rpm/s.
- Bake 90 s at 180 °C.

This recipe results in a resist thickness of ∼250 nm.

3. **Chromium evaporation**

   On top of the resist we evaporate a thin layer of chromium that acts as a conductive layer to prevent charge accumulation during the electron beam exposure. We use a AJA ATC-Orion 8E e-beam evaporation system to deposit 8.5 nm of chromium at 0.5 Å/s.

4. **Electron-beam exposure**

   To expose the resist we use a field emission scanning electron microscope (FEI Sirion) con-

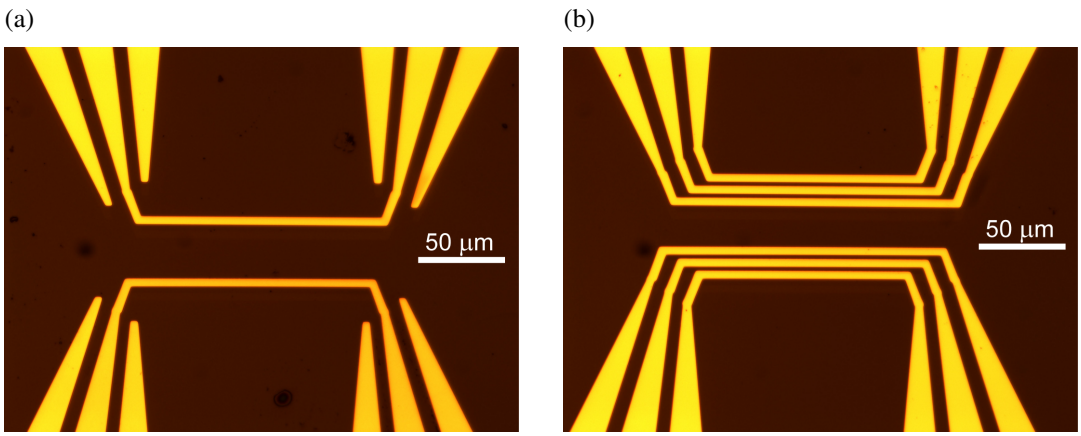

Figure C.2: Optical image of the measurement region of a pair of MSLs (a) and CPWs (b) antennas on a GGG substrate. The metal regions surrounding the signal line of the MSLs are the ground planes used to minimize the electrical losses in the system.

trolled with the Nanometer Pattern Generation System (NPGS, JC Nabity Lithography Systems). We use a 30 kV electron beam source with a current of 2350 pA (spot size 5) and a dose of 430 $\mu C/cm^2$.

5. **Chromium etch**

   We etch the chromium layer placing the sample in a ceric ammonium nitrate-based etchant (Sigma-Aldrich, 651826) for 10 s at room temperature.

6. **Development**

   70 s in Methyl isobutyl ketone (MIBK):IPA, 1:3.

7. **Oxygen plasma descum process**

   We use this step to ensure that the all the resist residues are removed from the exposed area promoting a good adhesion of the metal to the substrate. We use a Plasma Etch PE100 Oxygen Plasma Etcher with 100 W of bias power, 20 sccm.

8. **Metal Deposition**

   Using the AJA ATC-Orion 8E e-beam evaporation system we deposit 8.5 nm of titanium at 0.5 Å/s (the titanium acts as an adhesion layer for the following gold layer) and 200 nm of gold at 0.9 Å/s.

9. **Lift off**

   We place the sample in acetone and in an ultrasonic bath for 5 min to remove the remaining resist and the metal that was deposited on top of it.

In Figure C.2 we show the optical image of a pair of MSLs and of CPWs patterned on a GGG substrate. Only the region where the measurements are usually collected is shown.

APPENDIX D

FABRICATION OF NANOPILLARS IN SILICON CARBIDE

Here we describe a fabrication process for the fabrication nanopillar structures at the surface of a bulk silicon carbide (SiC) sample. The SiC crystal can contain paramagnetic point defects with properties similar to the NV center in diamond and with emission wavelength in the near infrared range[76, 19], which makes them particularly appealing for telecommunicaiton purposes. For this reason, we were interested in extending some of the fabrication techniques developed for diamond to obtain similar nanostructures in SiC. In particular, the creation of cylindrical pillars can strongly enhance the collection efficiency of the emitted photons[61], drastically improving the signal-to-noise ratio of the measurements. The following process was developed in the Searle cleanroom and nanofabrication facility at the University of Chicago using both 4H and 6H silicon carbide polymorphs.

1. **Substrate cleaning**

   We use a standard solvent cleaning process in an ultrasonic bath to prepare the substrate:

   - Toluene for 3 min.
   - Acetone for 3 min.
   - Methanol for 3 min.
   - IPA for 3 min.

   Finally we dehydrate the sample on a hot plate for 5 min at 100 °C.

2. **Bilayer resist preparation**

   We use a bilayer resist process to allow for a thicker metal mask.

   a) As the samples are usually small ($\sim$3 mm), we first bond them on a larger silicon carrier chip using a 950PMMA A4 bonding layer spinned using the recipe:

      - 5 s, 500 rpm, 300 rpm/s.

- 15 s, 1500 rpm, 500 rpm/s.
- Rapidly place the sample on top of the carrier and transfer to a hot plate at 95 °C for 2 min.
- Raise the temperature to 185 °C and hold for 5 min.

b) Spin coat PMMA copolymer resist EL11

- 5 s, 500 rpm, 500 rpm/s.
- 45 s, 4000 rpm, 1000 rpm/s.
- Bake 90 s at 150 °C.

This recipe results in a resist thickness of ∼500 nm.

c) Spin coat 950PMMA A4 (positive resist)

- 5 s, 500 rpm, 500 rpm/s.
- 45 s, 3000 rpm, 1000 rpm/s.
- Bake 90 s at 185 °C.

This recipe results in a resist thickness of ∼250 nm.

3. **Chromium evaporation**

On top of the resist we evaporate a thin layer of chromium that acts as a conductive layer to prevent charge accumulation during the electron beam exposure. We use a AJA ATC-Orion 8E e-beam evaporation system to deposit 6.5 nm of chromium at 0.5 Å/s.

4. **Electron-beam exposure**

To expose the resist we use a field emission SEM (FEI Sirion) controlled with the Nanometer Pattern Generation System (NPGS, JC Nabity Lithography Systems). In Figure D.1(a) we show a typical exposure pattern where the L-shaped areas are control markers, while the circles correspond to the regions where the mask for the pillars will be deposited. To expose these smaller circular regions we use a 30 kV electron beam with a current of 200 pA (spot

size 3) and a dose of 430 μC/cm^2. The markers were exposed using the same dose but larger spot size (5) and current (3000 pA) to reduce the processing time.

5. **Chromium etch**

   We etch the chromium layer placing the sample in a ceric ammonium nitrate-based etchant (Sigma-Aldrich, 651826) for 10 s at room temperature.

6. **Development**

   70 s in Methyl isobutyl ketone (MIBK):IPA, 1:3.

7. **Oxygen plasma descum process**

   We use this step to make sure that the all the resist residues are removed from the exposed area and promote a good adhesion of the metal to the substrate. We use a Plasma Etch PE100 Oxygen Plasma Etcher with 100 W of bias power, 20 sccm.

8. **Metal Deposition**

   Using again the AJA ATC-Orion 8E e-beam evaporation system we deposit 15 nm of titanium at 0.5 Å/s and 290 nm of gold at 0.9 Å/s.

9. **Lift off**

   We place the sample in a beaker with acetone that we position in an ultrasonic bath for 5 min to remove the excess resist and metal.

10. **SiC etch**

    We use a dry etch process in a ICP-RIE system (Oxford Instruments Plasma-Pro NGP80) to transfer the metal mask into the SiC substrate. The recipe we used is as follow:

    - Sulfur hexafluoride (SF_6) flow: 18 sccm.
    - Oxygen: 9 sccm.
    - Plasma strike pressure: 1.33 Pa.
    - Chamber pressure: 0.27 Pa.

- Radiofrequency source power: 1000 W.
- Bias power: 400 W.

These parameters result in an etch rate of 375 nm/min and we perform etches with depths ranging from 700 nm to 3 µm. In Figures D.1(b) and D.1(c) we present scanning electron microscopy images of one of the fabricated arrays of SiC pillars with the residual metal mask retained.

11. **Metal mask removal**

Finally we remove the remaining metal mask using a two step wet etch. We use a standard gold etchant (Sigma-Aldrich, 651818), which provides an etch rate of 28 Å/s at room temperature, and TFTN titanium etchant (Transene Company, Inc.) with a etch rate of $\sim$ 30 Å/s at 80 °C.

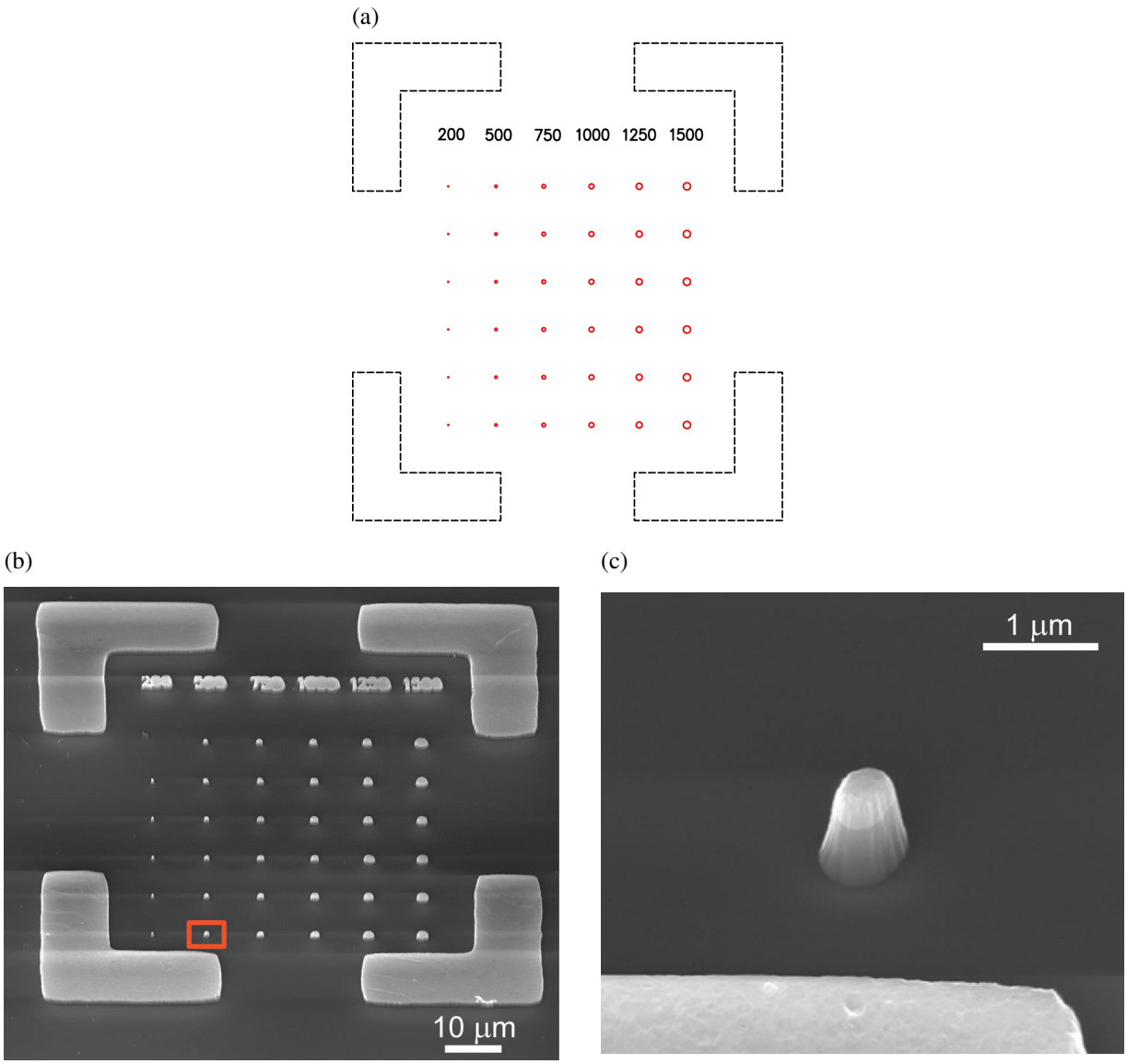

Figure D.1: (a) Design of the exposure pattern used to create the etch mask for an array of silicon carbide pillars with diameters ranging from 200 nm to 1500 nm. The L-shaped regions are markers that allows us to easily identify the arrays. (b) Scanning electron microscopy (SEM) image of an array of nano- and micropillars fabricated in a 4H silicon carbide substrate. (c) Magnified (SEM) image of the pillar highlighted in (b) showing the presence of the residual metal mask. Note that the SEM images were collected at a $\sim 30^{\circ}$ angle from the direction perpendicular to the SiC interface to allow for a clearer imaging of the pillars.

REFERENCES

[1] V. M. Acosta et al. Diamonds with a high density of nitrogen-vacancy centers for magnetometry applications. *Phys. Rev. B*, 80:115202, 2009.

[2] P. Andrich et al. Engineered micro- and nanoscale diamonds as mobile probes for high-resolution sensing in fluid. *Nano Lett.*, 14:4959, 2014.

[3] T. A. Baginski. An introduction to gold gettering in silicon. *Gold Bullet.*, 20:47, 1987.

[4] G. Balasubramanian et al. Ultralong spin coherence time in isotopically engineered diamond. *Nat. Mater.*, 8:383, 2009.

[5] P. B. Bareil and Y. Sheng. Angular and position stability of a nanorod trapped in an optical tweezers. *Opt. Express*, 18:26388, 2010.

[6] J. C. Bergquist, R. G. Hulet, W. M. Itano, and D. J. Wineland. Observation of quantum jumps in a single atom. *Phys. Rev. Lett.*, 57:1699, 1986.

[7] H. Bernien et al. Heralded entanglement between solid-state qubits separated by three metres. *Nature*, 497:86, 2013.

[8] A. V. Bespalov, O. L. Golikova, S. S. Savin, A. I. Stognij, and N. N. Novitskii. Preparation of magnonic crystals with nanoislands by focused ion beam etching. *Inorg. Mater.*, 48:1190, 2012.

[9] A. Beveratos, R. Brouri, T. Gacoin, J.-P. Poizat, and P. Grangier. Nonclassical radiation from diamond nanocrystals. *Phys. Rev. A*, 64:061802, 2001.

[10] R. Blatt and D. Wineland. Entangled states of trapped atomic ions. *Nature*, 453:1008, 2008.

[11] G. Boero, M. Demierre, P.-.A. Besse, and R.S. Popovic. Micro-hall devices: performance, technologies and applications. *Sens. and Act. A: Physical*, 106:314, 2003.

[12] J.-P. Boudou et al. High yield fabrication of fluorescent nanodiamonds. *Nanotech.*, 20:235602, 2009.

[13] C. Bradac et al. Observation and control of blinking nitrogen-vacancy centres in discrete nanodiamonds. *Nat. Nano.*, 5:345, 2010.

[14] Henrik Bruus. Chapter 1 governing equations in microfluidics. In *Microscale Acoustofluidics*, page 1. The Royal Society of Chemistry, 2015.

[15] D. G. Cahill et al. Nanoscale thermal transport. *Jour. of Appl. Phys.*, 93:793, 2003.

[16] Y. Cao, A. B. Stilgoe, L. Chen, T. A. Nieminen, and H. Rubinsztein-Dunlop. Equilibrium orientations and positions of non-spherical particles in optical traps. *Opt. Express*, 20:12987, 2012.

[17] L. Childress et al. Coherent dynamics of coupled electron and nuclear spin qubits in diamond. *Science*, 314:5797, 2006.

[18] Y. Cho, S. Gorina, P.D. Jeffrey, and N.P. Pavletich. Crystal structure of a p53 tumor suppressor-dna complex: understanding tumorigenic mutations. *Science*, 265:346, 1994.

[19] D. J. Christle et al. Isolated electron spins in silicon carbide with millisecond coherence times. *Nat. Mater.*, 14:160, 2015.

[20] I. Chuang and M. Nielsen. *Quantum Computation and Quantum Information*. Cambridge University Press, 2000. Cambridge.

[21] A. V. Chumak et al. Spin-wave propagation in a microstructured magnonic crystal. *Appl. Phys. Lett.*, 95:262508, 2009.

[22] J. I. Cirac and P. Zoller. Quantum computations with cold trapped ions. *Phys. Rev. Lett.*, 74:4091, May 1995.

[23] J. Clark. Squids. *Sci. Amer.*, 271:46, 1994.

[24] G. M. Clore et al. High-resolution structure of the oligomerization domain of p53 by multi-dimensional nmr. *Science*, 265:386, 1994.

[25] P. J. Cranfill et al. Quantitative assessment of fluorescent proteins. *Nat. Met.*, 13:557, 2016.

[26] R.W. Damon and J.R. Eshbach. Magnetostatic modes of a ferromagnet slab. *Jour. of Phys. and Chem. of Solids*, 19:308, 1961.

[27] V. V. Danilenko. On the history of the discovery of nanodiamond synthesis. *Physics of the Solid State*, 46:595, 2004.

[28] C. L. Degen. Nanoscale magnetometry: Microscopy with single spins. *Nat. Nanotech.*, 3:643, 2008.

[29] C. L. Degen. Scanning magnetic field microscope with a diamond single-spin sensor. *Appl. Phys. Lett.*, 92:243111, 2008.

[30] C. L. Degen, M. Poggio, H. J. Mamin, C. T. Rettner, and D. Rugar. Nanoscale magnetic resonance imaging. *Proc. Nat. Acad. Sci.*, 106:1313, 2009.

[31] V. E. Demidov et al. Excitation of microwaveguide modes by a stripe antenna. *Appl. Phys. Lett.*, 95:112509, 2009.

[32] R. M. Dickson, A. B. Cubitt, R. Y. Tsien, and W. E. Moerner. On/off blinking and switching behaviour of single molecules of green fluorescent protein. *Nature*, 388:355, 1997.

[33] D. P. DiVincenzo. The physical implementation of quantum computation. *Fortsch. der Phys.*, 48:771, 2000.

[34] V.V. Dobrovitski, G.D. Fuchs, A.L. Falk, C. Santori, and D.D. Awschalom. Quantum control over single spins in diamond. *Annu. Rev. Condens. Matter Phys.*, 4:1, 2013.

[35] M. W. Doherty et al. Theory of the ground-state spin of the nv^- center in diamond. *Phys. Rev. B*, 85:205203, 2012.

[36] F. Dolde et al. Room-temperature entanglement between single defect spins in diamond. *Nat. Phys.*, 9:139, 2013.

[37] J. S. Donner, S. A. Thompson, M. P. Kreuzer, G. Baffou, and R. Quidant. Mapping intracellular temperature using green fluorescent protein. *Nano Lett.*, 12:2107, 2012.

[38] A. Dréau et al. Avoiding power broadening in optically detected magnetic resonance of single nv defects for enhanced dc magnetic field sensitivity. *Phys. Rev. B*, 84:195204, 2011.

[39] C. Du et al. Control and local measurement of the spin chemical potential in a magnetic insulator. *arXiv*, 1611.07408, 2016.

[40] A. M. Edmonds et al. Production of oriented nitrogen-vacancy color centers in synthetic diamond. *Phys. Rev. B*, 86:035201, 2012.

[41] E. R. J. Edwards. Study of spin waves in in-plane magnetized thin films by means of brillouin light scattering and magneto-optical kerr effect, 2012.

[42] R. L. Fagaly. Superconducting quantum interference device instruments and applications. *Rev. of Sci. Instr.*, 77:101101, 2006.

[43] R. P. Feynman. There's plenty of room at the bottom. *Engineer. and Sci.*, 23:22, 1960.

[44] Center for Sustainable Nanotechnology. sustainable nano.com. `http://sustainable-nano.com/2014/01/23/nuclear-proliferation-sustainability-the-history-of-nanodiamonds`, Accessed: May 2017.

[45] M. R. Freeman and B. C. Choi. Advances in magnetic microscopy. *Science*, 294:1484, 2001.

[46] K.-M. C. Fu, C. Santori, P. E. Barclay, and R. G. Beausoleil. Conversion of neutral nitrogen-vacancy centers to negatively charged nitrogen-vacancy centers through selective oxidation. *Appl. Phys. Lett.*, 96:121907, 2010.

[47] T. Fukui et al. Perfect selective alignment of nitrogen-vacancy centers in diamond. *Appl. Phys. Expr.*, 7:055201, 2014.

[48] B. W. Gardner et al. Scanning superconducting quantum interference device susceptometry. *Rev. of Sci. Instr.*, 72:2361, 2001.

[49] M. Geiselmann et al. Three-dimensional optical manipulation of a single electron spin. *Nat. Nano.*, 8:175, 2013.

[50] S. Geller and M. A. Gilleo. Structure and ferrimagnetism of yttrium and rare-earth-iron garnets. *Acta Crystallogr.*, 10:239, 1957.

[51] C. Granata and A. Vettoliere. Nano superconducting quantum interference device: A powerful tool for nanoscale investigations. *Phys. Rep.*, 614:1, 2016.

[52] N. R. Greiner, D. S. Phillips, J. D. Johnson, and F. Volk. Diamonds in detonation soot. *Nature*, 333:440, 1988.

[53] M. S. Grinolds et al. Nanoscale magnetic imaging of a single electron spin under ambient conditions. *Nat. Phys.*, 9:215–219, 2013.

[54] G. Grosso and G. Pastori Parravicini. *Solid State Physics*. Elsevier Ltd., 2000. Oxford.

[55] A. Gruber et al. Scanning confocal optical microscopy and magnetic resonance on single defect centers. *Science*, 276(5321):2012, 1997.

[56] P. Gruszecki, M. Kasprzak, A. E. Serebryannikov, M. Krawczyk, and Śmigaj. Microwave excitation of spin wave beams in thin ferromagnetic films. *Sci. Rep.*, 6:22367, 2015.

[57] M. V. Gurudev Dutt et al. Quantum register based on individual electronic and nuclear spin qubits in diamond. *Science*, 316:1312, 2007.

[58] L. T. Hall, J. H. Cole, C. D. Hill, and L. C. L. Hollenberg. Sensing of fluctuating nanoscale magnetic fields using nitrogen-vacancy centers in diamond. *Phys. Rev. Lett.*, 103:220802, 2009.

[59] E. Han, K. O. Stuen, Y.-H. La, P. F. Nealey, and P. Gopalan. Effect of composition of substrate-modifying random copolymers on the orientation of symmetric and asymmetric diblock copolymer domains. *Macromolecules*, 41:9090, 2008.

[60] M. V. Hauf et al. Chemical control of the charge state of nitrogen-vacancy centers in diamond. *Phys. Rev. B*, 83:081304, 2011.

[61] B. J. M. Hausmann et al. Fabrication of diamond nanowires for quantum information processing applications. *Diam. and Rel. Mater.*, 19:621, 2010.

[62] V. R. Horowitz, B. J. Alemán, D. J. Christle, A. N. Cleland, and D. D. Awschalom. Electron spin resonance of nitrogen-vacancy centers in optically trapped nanodiamonds. *Proc. Nat. Acad. Sci.*, 109:13493, 2012.

[63] M. E. Huber et al. Gradiometric micro-squid susceptometer for scanning measurements of mesoscopic samples. *Rev. of Sci. Instr.*, 79:053704, 2008.

[64] M. J. Hurben and C. E. Patton. Theory of magnetostatic waves for in-plane magnetized isotropic films. *Journ. of Magn. and Magn. Mater.*, 139:263, 1995.

[65] K. Iakoubovskii, K. Mitsuishi, and K. Furuya. High-resolution electron microscopy of detonation nanodiamond. *Nanotech.*, 19:155705, 2008.

[66] B. Jang et al. Undulatory locomotion of magnetic multilink nanoswimmers. *Nano Lett.*, 15:4829, 2015.

[67] A. Jarmola, V. M. Acosta, K. Jensen, S. Chemerisov, and D. Budker. Temperature- and magnetic-field-dependent longitudinal spin relaxation in nitrogen-vacancy ensembles in diamond. *Phys. Rev. Lett.*, 108:197601, 2012.

[68] N. Kalb et al. Entanglement distillation between solid-state quantum network nodes. *Science*, 356:928, 2017.

[69] B. A. Kalinikos. Excitation of propagating spin waves in ferromagnetic films. *Micro., Opt. and Ant., IEEE Proc. H*, 127:4, 1980.

[70] B. A. Kalinikos and A. N. Slavin. Theory of dipole-exchange spin wave spectrum for ferromagnetic films with mixed exchange boundary conditions. *Journ. of Phys. C: Sol. St. Phys.*, 19:7013, 1986.

[71] Y. Kamei et al. Infrared lasermediated gene induction in targeted single cells in vivo. *Nat. Met.*, 6:79, 2009.

[72] M. Kim et al. Decoherence of near-surface nitrogen-vacancy centers due to electric field noise. *Phys. Rev. Lett.*, 115:087602, 2015.

[73] J. R. Kirtley et al. Highresolution scanning squid microscope. *Appl. Phys. Lett.*, 66:1138, 1995.

[74] C. Kittel. *Quantum theory of solids*. Wiley, 1963. New York.

[75] H. Knowles, D. Kara, and M. Atat´ure. Observing bulk diamond spin coherence in high-purity nanodiamonds. *Nat. Mater.*, 13:21, 2014.

[76] W. F. Koehl, B. B. Buckley, F. J. Heremans, G. Calusine, and D. D. Awschalom. Room temperature coherent control of defect spin qubits in silicon carbide. *Nature*, 479:84, 2011.

[77] M. Krawczyk and D. Grundler. Review and prospects of magnonic crystals and devices with reprogrammable band structure. *Journ. of Phys.: Cond. Matt.*, 26:123202, 2014.

[78] Y. Kubo et al. Hybrid quantum circuit with a superconducting qubit coupled to a spin ensemble. *Phys. Rev. Lett.*, 107:220501, 2011.

[79] G. Kucsko et al. Nanometre-scale thermometry in a living cell. *Nature*, 500:54, 2013.

[80] S. V. Kumar and P. A. Wigge. H2a.z-containing nucleosomes mediate the thermosensory response in arabidopsis. *Cell*, 140:136, 2010.

[81] N. D. Lai et al. Quenching nitrogenvacancy center photoluminescence with an infrared pulsed laser. *New Jour. of Phys.*, 15:033030, 2013.

[82] A. Laraoui, J. S. Hodges, and C. A. Meriles. Nitrogen-vacancy-assisted magnetometry of paramagnetic centers in an individual diamond nanocrystal. *Nano Lett.*, 12:3477, 2012.

[83] M. Leijnse and K. Flensberg. Coupling spin qubits via superconductors. *Phys. Rev. Lett.*, 111:060501, 2013.

[84] B. Lenk, H. Ulrichs, F. Garbs, and M. M´unzenberg. The building blocks of magnonics. *Phys. Rep.*, 507:107, 2011.

[85] M. Lesik et al. Perfect preferential orientation of nitrogen-vacancy defects in a synthetic diamond sample. *Appl. Phys. Lett.*, 104:113107, 2014.

[86] E. M. Levenson-Falk, R. Vijay, N. Antler, and I. Siddiqi. A dispersive nanosquid magnetometer for ultra-low noise, high bandwidth flux detection. *Supercond. Sci. and Tech.*, 26:055015, 2013.

[87] K. A. Lidke, B. Rieger, T. M. Jovin, and R. Heintzmann. Superresolution by localization of quantum dots using blinking statistics. *Opt. Expr.*, 13:7052, 2005.

[88] L. Liu, Xiaoying et al. Deterministic construction of plasmonic heterostructures in well-organized arrays for nanophotonic materials. *Adv. Mater.*, 27:7314, 2015.

[89] Y. Liu, J. You, and Q. Hou. Entanglement dynamics of nitrogen-vacancy centers spin ensembles coupled to a superconducting resonator. *Nat. Comm.*, 6:21775, 2016.

[90] D. Loss and D. P. DiVincenzo. Quantum computation with quantum dots. *Phys. Rev. A*, 57:120, 1998.

[91] E. R. MacQuarrie, M. Otten, S. K. Gray, and G. D. Fuchs. Cooling a mechanical resonator with nitrogen-vacancy centres using a room temperature excited state spinstrain interaction. *Nat. Comm.*, 8:14358, 2017.

[92] B. J. Maertz, A. P. Wijnheijmer, G. D. Fuchs, M. E. Nowakowski, and D. D. Awschalom. Vector magnetic field microscopy using nitrogen vacancy centers in diamond. *Appl. Phys. Lett.*, 96:092504, 2010.

[93] A. P. Magyar et al. Fabrication of thin, luminescent, single-crystal diamond membranes. *Appl.Phys. Lett.*, 99:081913, 2011.

[94] A. Majumdar. Scanning thermal microscopy. *Ann. Rev. Mat. Sci.*, 29:505, 1999.

[95] H. J. Mamin et al. Nanoscale nuclear magnetic resonance with a nitrogen-vacancy spin sensor. *Science*, 339:557, 2013.

[96] H. J. Mamin et al. Multipulse double-quantum magnetometry with near-surface nitrogen-vacancy centers. *Phys. Rev. Lett.*, 113:030803, 2014.

[97] N. B. Manson, J. P. Harrison, and M. J. Sellars. Nitrogen-vacancy center in diamond: Model of the electronic structure and associated dynamics. *Phys. Rev. B*, 74:104303, 2006.

[98] Materialscientist. Nitrogen-vacancy center: Nvple.jpg. `https://commons.wikimedia.org/wiki/File:NVple.JPG`, Accessed: May 2017.

[99] P. C. Maurer et al. Far-field optical imaging and manipulation of individual spins with nanoscale resolution. *Nat. Phys.*, 6:912, 2010.

[100] J. R. Maze et al. Nanoscale magnetic sensing with an individual electronic spin in diamond. *Nature*, 455:7213, 2008.

[101] J. C. McDonald et al. Fabrication of microfluidic systems in poly(dimethylsiloxane). *Electrophoresis*, 21:27, 2000.

[102] L. P. McGuinness et al. Ambient nanoscale sensing with single spins using quantum decoherence. *New Jour. of Phys.*, 15:073042, 2013.

[103] D. M. Meekhof, C. Monroe, B. E. King, W. M. Itano, and D. J. Wineland. Generation of nonclassical motional states of a trapped atom. *Phys. Rev. Lett.*, 76:1796, 1996.

[104] V. N. Mochalin, O. Shenderova, D. Ho, and Y. Gogotsi. The properties and applications of nanodiamonds. *Nat. Nano.*, 7:11, 2012.

[105] C. Monroe, D. M. Meekhof, B. E. King, W. M. Itano, and D. J. Wineland. Demonstration of a fundamental quantum logic gate. *Phys. Rev. Lett.*, 75:4714, 1995.

[106] T. Monz et al. 14-qubit entanglement: Creation and coherence. *Phys. Rev. Lett.*, 106:130506, 2011.

[107] D. Mounce. Magnetic resonance force microscopy. *IEEE Instr. Meas. Mag.*, 8:20, 2005.

[108] B. A. Myers et al. Probing surface noise with depth-calibrated spins in diamond. *Phys. Rev. Lett.*, 113:027602, 2014.

[109] A. H. Myerson et al. High-fidelity readout of trapped-ion qubits. *Phys. Rev. Lett.*, 100:200502, 2008.

[110] W. Nagourney, J. Sandberg, and H. Dehmelt. Shelved optical electron amplifier: Observation of quantum jumps. *Phys. Rev. Lett.*, 56:2797, 1986.

[111] B. Naydenov et al. Dynamical decoupling of a single-electron spin at room temperature. *Phys. Rev. B*, 83:081201, 2011.

[112] P. Neumann et al. High-precision nanoscale temperature sensing using single defects in diamond. *Nano Lett.*, 13:2738, 2013.

[113] S. Neusser and D. Grundler. Magnonics: Spin waves on the nanoscale. *Adv. Mater.*, 21:2927, 2009.

[114] K. Ohno et al. Engineering shallow spins in diamond with nitrogen delta-doping. *Appl. Phys. Lett.*, 101:082413, 2012.

[115] K. Ohno et al. Three-dimensional localization of spins in diamond using 12c implantation. *Appl. Phys. Lett.*, 105:052406, 2014.

[116] K. Okabe et al. Intracellular temperature mapping with a fluorescent polymeric thermometer and fluorescence lifetime imaging microscopy. *Nat. Comm.*, 3:705, 2012.

[117] H. Ozawa, K. Tahara, H. Ishiwata, M. Hatano, and T. Iwasaki. Formation of perfectly aligned nitrogen-vacancy-center ensembles in chemical-vapor-deposition-grown diamond (111). *Appl. Phys. Expr.*, 10:045501, 2017.

[118] M. P. Page et al. Optically detected ferromagnetic resonance in metallic ferromagnets via nitrogen vacancy centers in diamond. *arXiv*, 1607.07485, 2016.

[119] C. E. Patton. Linewidth and relaxation processes for the main resonance in the spinwave spectra of nife alloy films. *Journ. of Appl. Phys.*, 39:3060, 1968.

[120] W. Pfaff et al. Unconditional quantum teleportation between distant solid-state quantum bits. *Science*, 345:532, 2014.

[121] R. J. Pylkki, P. J. Moyer, and P. E. West. Scanning near-field optical microscopy and scanning thermal microscopy. *Jap. Jour. Appl. Phys.*, 33:3785, 1994.

[122] J. R. Rabeau et al. Implantation of labelled single nitrogen vacancy centers in diamond using n15. *Appl. Phys. Lett.*, 88:023113, 2006.

[123] P. Rabl et al. A quantum spin transducer based on nanoelectromechanical resonator arrays. *Nat. Phys.*, 6:602, 2010.

[124] RCSB. Protein data bank: Content growth report. `http://www.rcsb.org/pdb/statistics/contentGrowthChart.do?content=total&seqid=100\`, Accessed: February 2017.

[125] L. Rondin et al. Nanoscale magnetic field mapping with a single spin scanning probe magnetometer. *Appl. Phys. Lett.*, 100:153118, 2012.

[126] L. Rondin et al. Magnetometry with nitrogen-vacancy defects in diamond. *Rep. on Progr. in Phys.*, 77:056503, 2014.

[127] D. Rugar, R. Budakian, H. J. Mamin, and B. W. Chui. Single spin detection by magnetic resonance force microscopy. *Nature*, 430:329, 2004.

[128] D. Rugar et al. Proton magnetic resonance imaging using a nitrogen-vacancy spin sensor. *Nat. Nanotech.*, 10:120, 2015.

[129] M. J. Rust, M. Bates, and X. Zhuang. Sub-diffraction-limit imaging by stochastic optical reconstruction microscopy (storm). *Nat. Met.*, 3:793, 2006.

[130] R. Schirhagl, K. Chang, M. Loretz, and C. L. Degen. Nitrogen-vacancy centers in diamond: Nanoscale sensors for physics and biology. *Annu. Rev. Phys. Chem.*, 65:83, 2014.

[131] T. Schneider, A. A. Serga, T. Neumann, B. Hillebrands, and M. P. Kostylev. Phase reciprocity of spin-wave excitation by a microstrip antenna. *Phys. Rev. B*, 77:214411, 2008.

[132] A.M. Schrand, S. A. Ciftan Hens, and O. A. Shenderova. Nanodiamond particles: Properties and perspectives for bioapplications. *Critic. Rev. in Sol. St. and Mat. Sci.*, 34:18, 2009.

[133] A. Schroeder et al. Treating metastatic cancer with nanotechnology. *Nat. Rev. Canc.*, 12:39, 2012.

[134] K. Sekiguchi et al. Nonreciprocal emission of spin-wave packet in feni film. *Appl. Phys. Lett.*, 97:022508, 2010.

[135] A. A. Serga, A. V. Chumak, and B. Hillebrands. Yig magnonics. *Journ. of Phys. D: Appl. Phys.*, 43:264002, 2010.

[136] A. Shalek et al. Vertical silicon nanowires as a universal platform for delivering biomolecules into living cells. *Proc. Nat. Acad. Sci.*, 107:1870, 2010.

[137] J. A. Sidles. Noninductive detection of singleproton magnetic resonance. *Applied Physics Letters*, 58:2854–2856, 1991.

[138] J. A. Sidles et al. Magnetic resonance force microscopy. *Rev. Mod. Phys.*, 67:249, 1995.

[139] D. Stancil and A. Prabhakar. *Spin Waves*. Springer US, 2009. New York.

[140] T. Staudacher et al. Nuclear magnetic resonance spectroscopy on a (5-nanometer)^3 sample volume. *Science*, 339:561, 2013.

[141] M. Steiner, P. Neumann, J. Beck, F. Jelezko, and J. Wrachtrup. Universal enhancement of the optical readout fidelity of single electron spins at nitrogen-vacancy centers in diamond. *Phys. Rev. B*, 81:035205, 2010.

[142] S. Steinert et al. Magnetic spin imaging under ambient conditions with sub-cellular resolution. *Nat. Comm.*, 4:1607, 2013.

[143] P. H. Tamarat et al. Spin-flip and spin-conserving optical transitions of the nitrogen-vacancy centre in diamond. *New Jour. of Phys.*, 10:045004, 2008.

[144] J. Taylor et al. High-sensitivity diamond magnetometer with nanoscale resolution. *Nat. Phys.*, 4:810–816, 2008.

[145] J.-P. Tetienne et al. Nanoscale imaging and control of domain-wall hopping with a nitrogen-vacancy center microscope. *Science*, 344:1366, 2014.

[146] J.-P. Tetienne et al. Scanning nanospin ensemble microscope for nanoscale magnetic and thermal imaging. *Nano Lett.*, 16:326, 2016.

[147] J. Tisler et al. Fluorescence and spin properties of defects in single digit nanodiamonds. *ACS Nano*, 3:1959, 2009.

[148] D. M. Toyli, C. F. de las Casas, D. J. Christle, V. V. Dobrovitski, and D. D. Awschalom. Fluorescence thermometry enhanced by the quantum coherence of single spins in diamond. *Proc. Nat. Acad. Sci.*, 110:8417, 2013.

[149] D. M. Toyli et al. Measurement and control of single nitrogen-vacancy center spins above 600 k. *Phys. Rev. X*, 2:031001, 2012.

[150] L. Trifunovic et al. High-efficiency resonant amplification of weak magnetic fields for single spin magnetometry at room temperature. *Nat. Nanotech.*, 10:541, 2015.

[151] L. Trifunovic, F. L. Pedrocchi, and D. Loss. Long-distance entanglement of spin qubits via ferromagnet. *Phys. Rev. X*, 3:041023, 2013.

[152] M. Trusheim. Scalable fabrication of high purity diamond nanocrystals with long-spin-coherence nitrogen vacancy centers. *Nano Lett.*, 14:32, 2014.

[153] T. Ungár, A. Borbély, G. R. Goren-Muginstein, S. Berger, and A. R. Rosen. Particle-size, size distribution and dislocations in nanocrystalline tungsten-carbide. *Nanostr. Mater.*, 11:103, 1999.

[154] T. van der Sar, F. Casola, R. Walsworth, and A. Yacoby. Nanometre-scale probing of spin waves using single-electron spins. *Nat. Comm.*, 6:7886, 2015.

[155] F. Vetrone et al. Temperature sensing using fluorescent nanothermometers. *ACS Nano*, 4:3254, 2010.

[156] S. Viaene, V. Ginis, J. Danckaert, and P. Tassin. Transforming two-dimensional guided light using nonmagnetic metamaterial waveguides. *Phys. Rev. B*, 93:085429, 2016.

[157] I. I. Vlasov et al. Nitrogen and luminescent nitrogen-vacancy defects in detonation nanodiamond. *Small*, 6:687, 2010.

[158] T. D. Vreugdenburg, C. D. Willis, L. Mundy, and J. E. Hiller. A systematic review of elastography, electrical impedance scanning, and digital infrared thermography for breast cancer screening and diagnosis. *Breast Canc. Res. and Treat.*, 137:665, 2013.

[159] Z.-H. Wang, G. de Lange, D. Ristè, R. Hanson, and V. V. Dobrovitski. Comparison of dynamical decoupling protocols for a nitrogen-vacancy center in diamond. *Phys. Rev. B*, 85, 2012.

[160] G. D. Watkins. *Electron Paramagnetic Resonance of Point Defects in Solids, with Emphasis on Semiconductors*, page 333. Springer US, Boston, MA, 1975.

[161] S. A. Wolf et al. Spintronics: A spin-based electronics vision for the future. *Science*, 294:1488, 2001.

[162] C. S. Wolfe et al. Off-resonant manipulation of spins in diamond via precessing magnetization of a proximal ferromagnet. *Phys. Rev. B*, 89:180406, 2014.

[163] C. S. Wolfe et al. Spatially resolved detection of complex ferromagnetic dynamics using optically detected nitrogen-vacancy spins. *Appl. Phys. Lett.*, 108:232409, 2016.

[164] L. Xiaoying, S. P. McBride, H. M. Jaeger, and P. F. Nealey. Hybrid nanostructures of well-organized arrays of colloidal quantum dots and a self-assembled monolayer of gold nanoparticles for enhanced fluorescence. *Nanotechn.*, 27:285301, 2016.

[165] C.G. Yale et al. Optical manipulation of the berry phase in a solid-state spin qubit. *Nat. Phot.*, 10:184, 2016.

[166] J.-M. Yang, H. Yang, and L. Lin. Quantum dot nano thermometers reveal heterogeneous local thermogenesis in living cells. *ACS Nano*, 5:5067, 2011.

[167] N Y. Yao et al. Scalable architecture for a room temperature solid-state quantum information processor. *Nat. Comm.*, 3:800, 2012.

[168] H. Yu et al. Magnetic thin-film insulator with ultra-low spin wave damping for coherent nanomagnonics. *Sci. Rep.*, 4:6848, 2014.

[169] S.-J. Yu, M.-W. Kang, H.-C. Chang, K.-M. Chen, and Y.-C. Yu. Bright fluorescent nanodiamonds: no photobleaching and low cytotoxicity. *Jour. Amer. Chem. Soc.*, 127:17604, 2005.

[170] Y. Yue and X. Wang. Nanoscale thermal probing. *Nano Rev.*, 3:11586, 2012.